NANOSCALE BIOFETS FOR ULTRASENSITIVE PH AND BIOMOLECULAR DETECTION

BY

BOBBY REDDY, JR.

DISSERTATION

Submitted in partial fulfillment of the requirements
for the degree of Doctor of Philosophy in Electrical and Computer Engineering
in the Graduate College of the
University of Illinois at Urbana-Champaign, 2012

Urbana, Illinois

Doctoral Committee:

Professor Rashid Bashir, Chair
Professor Brian T. Cunningham
Professor Kanti Jain
Professor Muhammad Ashraful Alam, Purdue University

ABSTRACT

In the last decade, nanoscale field-effect transistor biosensors have proven to be powerful, ultra-sensitive, label-free electrical detectors of relevant molecules ranging from solution pH to proteins to nucleic acids. Such sensors are highly amenable to scale-up and mass production and are easily integrated with necessary external electronics for point-of-care diagnostic devices, or lab-on-a-chip systems. In particular, nanowire FET sensors have been demonstrated to be much more sensitive to analytes, extending sensing capabilities to as low as attomolar concentrations without the need for labels. These devices have the potential to far surpass many current clinical alternatives in many important criteria, such as sensitivity, detection time, sample volumes, need for a label, and selectivity. However, in recent years it has become apparent that the technology has been suffering from lack of reliability, robustness, and repeatability of the devices in fluidic environments. These issues are the primary barriers preventing the maturation of the technology.

Towards resolving some of these issues, this dissertation presents an iterative process of increasing the performance characteristics of nanoscale field-effect transistor biosensors. A top-down baseline silicon dioxide process with silicon-on-insulator wafers is presented, including methods for defining the biosensors at the nanoscale. This baseline process is then demonstrated for the detection of changes in pH and for detection of pyrophosphate (work in collaboration with Grace Credo, Oguz Elibol, and Madoo Varma at Intel Corporation). The CMOS compatible process presented allows for mass scale-up and for seamless integration with existing platforms.

The next iteration of devices utilizes an atomic layer deposited high-k gate dielectric, aluminum oxide (Al_2O_3), for increased gate oxide capacitance. A high-k gate dielectric allows for similar electrical gate oxide thicknesses with higher physical oxide thicknesses, which results in lower leakages in fluid. This process is compared to the baseline SiO_2 process. These process

improvements result in increased sensitivity to pH, increased robustness in fluid, and reduced noise.

The last device iteration replaces the Al_2O_3 gate dielectric with hafnium oxide (HfO_2). HfO_2 has a higher dielectric constant than Al_2O_3, is less susceptible to ion incorporation in fluid, has higher pH sensitivity, and is highly resistant to all forms of etching after annealed. This allows for the use of a wet etch of the fluid passivation layer, removing the possibility of damaging the fragile gate dielectric layer by dry etches such as reactive ion etching. Several critical steps were added for better characterization of gate dielectric layer, with special attention to the insulator-silicon interface. The HfO_2 devices exhibited near Nernstian pH response with very low noise and good repeatability. Two of these stable devices were then employed simultaneously in a novel scheme that greatly amplifies pH response (work in collaboration with Professor Ashraf Alam at Purdue University). Using the drastic differences in source-drain current for a 2 μm wide nanoplate device compared to a 100 nm wide nanowire device, the pH amplification scheme was shown to theoretically enable the detection of extremely low pH changes, down to 0.002 pH units. The devices were then used for the detection of microRNA analogues, short 20-25 base pair nucleotide molecules that have found use in the last decade as cancer biomarkers, down to 100 fM concentration levels. The process improvements in this work demonstrate significant progress towards catalyzing the transformation of such nanoscale bioFETs from mere proofs of concept into powerful, robust, and reliable tools for point-of-care diagnostics.

To my parents and to my little sister for their everlasting love and support.

ACKNOWLEDGMENTS

Several key people contributed to the work in this disseration, including mentors, family, co-workers, collaborators, and friends. My quest for the holy grail (the PhD) has been hands-down the most challenging endeavor of my life, and would have faltered years ago if not for the invaluable support of people around me. Professor Rashid Bashir has been one of the best mentors someone could ask for over the course of this process, in good times and, more importantly, through the inevitable tough times. His unwavering support and guidance have been the foundation upon which any of this work is built. He has also given me the opportunity to work with an astoundingly interdisciplinary group of collaborators, including experts in the theoretical aspects of the work (Professor Ashraf Alam at Purdue), cancer physician experts (Dr. Sue Clare at IUPUI), industry experts (Integrated Biosystems Lab at Intel Corporation), surface functionalization experts (Professor Don Bergstrom at Purdue), and so many more. I am forever indebted to all of these groups and people for so much technical advice and discussions over the (many) years.

I must sincerely thank Dr. Oguz Hasan Elibol, who is a mentor and dear friend whose efforts gave rise to this work so many years ago. Without his countless hours of research, discussions, and advice, none of this would have been possible or worth doing. I would also like to thank Brian Ross Dorvel, who has been there in the trenches with me for the past few years. Brian is an amazingly intelligent individual with genuine passion and interest in the research, and I feel extremely fortunate that I had the opportunity to work so closely with him over the years. I would also like to thank other members of our team, including Eric Salm, Carlos Duarte, Nima Jokilaakso, and David Korenchan for so many useful discussions, hard work, enthusiasm, and support. Pradeep Nair from Purdue offered so much insight over the course of the project and is a truly brilliant researcher. In addition, the staff

at MNTL have always been helpful and knowledgeable about pretty much everything, especially John Hughes, Edmond Chow, and Yaguang Lian.

Several friends, mostly also from the Bashir group, have been there with me through thick and thin, and I would be remiss not to mention them here. I count myself lucky to have the privilege of calling Piyush Bajaj and Matz Kasten my friends. They are truly amazing individuals without whom the PhD experience would have been not only impossible, but significantly less worthwhile and fulfilling. I would also like to thank Murali Venkatesan for so many years of good times and for valuable guidance and advice over the course of living together. Sukru Yeminicioglu, we had so many great times and I look forward to more in the future! Yi-Shao Liu and Kidong Park are extremely intelligent friends that I enjoyed hanging out with while we were trying not to avoid talk about work, even when we were unsuccessful. Enrique Carrion helped distract from work for (probably too many) hours, and indeed in the last year 406 E. Park has been almost like a second home on the weekends (thanks Joe, Steve, Sabrina, Sandy, Mimos, Taissa)!

Last but certainly not least, my family. To my parents, no words can describe what you have done for me, so I will not try. I will always love and cherish you. It is times like this that you are reminded not to take those closest to you for granted. To mei mei (Jessica Reddy), I love you and always will no matter what. Thanks for being you.

I would also like to thank the sponsors that supplied the funding for the work - DARPA, NIH, NSF, Intel Corporation, and TSMC Corporation.

"No dream comes true until you wake up and go to work."

– Anonymous

TABLE OF CONTENTS

CHAPTER 1

INTRODUCTION

Cancer is one of the greatest challenges that our generation will face. Approximately 1.6 million new cases of cancer were diagnosed in 2011, with over 600,000 deaths [1]. Past the age of 73, chances of cancer diagnosis skyrocket, an unforunate fact compounded by the realization that our baby boomer population is passing that very age presently. And yet, we remain woefully unprepared for what is to come. Current cancer diagnostic techniques are quite simply too slow and not sensitive enough, a broad-reaching statement which applies to nearly all types of cancer. Shocklingly, the most common ways to diagnose cancer are either by x-ray or via self-exam, when tumors are already on the order of 100 million to 1 billion cells [2]! Cheap, accurate, sensitive, and rapid diagnostic schemes will be an absolute necessity moving forward, for three critical reasons:

- Enabling of much earlier detection of cancer, which directly translates into increased survival rates
- Increased feedback about the efficacy of cancer treatment strategies for development of better treatments
- Mapping and de-convolution of the complex pathways that lead to cancer, which is essential for an eventual "cure to cancer"

Point-of-care devices, also known as lab-on-a-chip devices, may satisfy these requirements by enabling the same functions of bulky, costly lab equipment with cheap, portable devices. Intrinsic to the reduzed size of these devices are often enhanced sensitivity, reduced cost, reduced diagnosis times, and reduced sample volumes [3]. Field-effect transistor biosensors (bioFETs) are one possible technology for the sensing component of such point-of-care devices. BioFETs combine ubiquitous transistor technology with a biosensitive membrane, resulting in sensors that are much cheaper than alternatives,

much more sensitive, and much more easily integrated with necessary external electronics.

This work focuses on the development of nanoscale bioFETs for detection of various processes indicative of cancer. Though the technology was initially demonstrated over a decade ago, several device related issues have prevented the technology from reaching full maturation. This disseration is aimed at addressing these issues — including reliability, robustness, stability, sensitivity, selectivity, and repeatability of bioFET devices. Multiple iterations of device fabrication are shown, each with improvements targetted at increasing device performance, demonstrated with sensing of various important cancer related properties, including pH, proteins, DNA, and microRNA. Chapter 2 will focus on the relevant background for bioFETs, with focus on the individual components for the sensor — biological, chemical, electrochemical, and electrical. Chapter 2 will also address the relevant work to date on similar sensors for the detection of pH, nucleic acids, and protein. Next, the first baseline process for the bioFETs will be established in Chapter 3. Briefly, the method for creating the nanoscale devices will be discussed, critical process steps will be addressed, and measurement schemes will be illustrated. In Chapter 4, the resulting devices will be shown to be capable of small non-specific molecules (pyrophosphates) showing polymerase activity, short nucleic acid oligomers, and immunoglobulin proteins. Next, Chapter 5 will illustrate how device performance can be dramatically improved by the use of a high-k dielectric, $Al_2O_3(\epsilon_r=9)$, which decreases the effective electrical thickness of the gate dielectric with higher physical thicknesses. We will discuss how process steps need to be enhanced to incorporate the high-k dielectric and how this inclusion results in devices that are more stable, more robust in fluid, and more sensitive to changes in pH. Chapter 6 will demonstrate the further enhancement of these parameters, with the use of a hafnium oxide (HfO_2) gate dielectric, which has a ϵ_r value of 20-25. The hafnium oxide devices are extremely stable in fluid for long periods of time, exhibit very low noise, and have very high sensitivity to charge. The devices are used to demonstrate the sensitive detection of microRNA sequences which are well known to be cancer biomarkers. These devices are also used to demonstrate ultrasensitive pH detection, down to 0.002 pH units, using a novel pH amplification scheme that utilizes two devices with large width discrepancies simultaneously in Chapter 7. Such high pH sensitivity could

be used to monitor small changes in intracellular and extracellular pH, which gradually changes depending on the progression of various cancers. The devices described in this work exhibit superior base characteristics to devices reported in most of the work in the literature, and with further optimization could usher in a new era of point-of-care bioFET devices.

CHAPTER 2

BACKGROUND AND LITERATURE REVIEW

In this chapter, relevant background information will be presented about biosensors, including the motivation for creating such devices, the basic elements of any biosensor, relevant literature in the field, and the characteristics of an ideal biosensor.

2.1 Basics of Biosensors

Biosensors are a large classification of devices which refer to anything that can be used to detect the presence of biological entities. A wide variety of sensor read-out schemes, configurations, relevant target molecules, and operational principles have been discussed and investigated. However, for a general biosensor, two basic components usually exist, as is illustrated in Figure 2.1. These include a bio-functional membrane, which interfaces directly with the biological entities of interest, and a transducer element, which translates the phenomena observed at the bio-functional membrane into an electrical output.

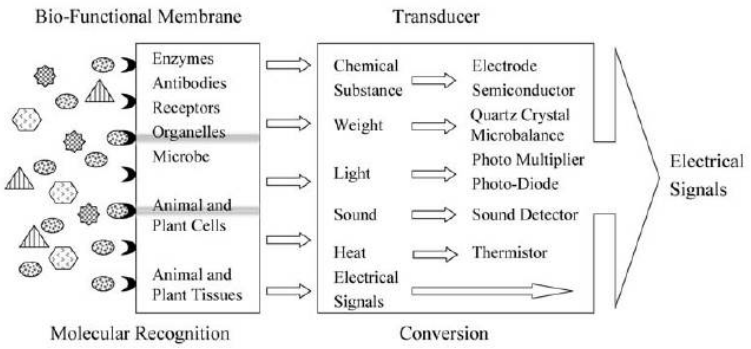

Figure 2.1: General components of a biosensor, from [4].

2.1.1 Motivation

The human body can be compared quite aptly to human societies, where the members of the society are analogous to the cells of the body. However, the body is a very unique society where rules of self-sacrifice (called apoptosis for cells) take precedence over rules of survival of the fittest [2]. Proper cell collaboration eventually leads to the proper functioning of the whole enterprise, the human body. Cancer can be thought of as a striking divergence from this rule; it is defined as the uncontrolled growth of abnormal or atypical cells, called mutated cells [2]. An adult human body is roughly composed of 100 trillion cells, with billions of cells undergoing mutation daily. Regulatory mechanisms (the law enforcement force of the body) prevent these mutations from wreaking havoc on the body. However, in certain cases, repeated selfish behavior by these mutated cells escapes rectification and jeopardizes the entire society, giving birth to cancer. Cancer is a collection of these mutated cells which replicate out of control.

Cells live, grow, divide and die following a strict set of rules defined by the genome, which is a set of instructions in a person's deoxyribonucleic acid (DNA). DNA is composed of four different bases adenine (A), thymine (T), guanine (G) and cytosine (C). Human DNA consists of 3 billion bases which give rise to roughly about 30,000 genes. Genes are portions of DNA which are translated into vital body proteins. There are three different processes happening in every cell of the body: DNA replication, transcription, and translation. During DNA replication, the DNA of a cell is copied, resulting in two copies of the parent DNA in the daughter cells. Transcription is the process of converting the DNA to ribonucleic acids (RNAs). RNA is another nucleic acid similar to DNA with the exception of having uridine (U) as a possible base instead of T. During transcription, a complementary strand of RNA is formed. Translation is the process where the RNA produced during transcription is decoded to synthesize a protein using amino acids as building blocks. Figure 2.2 demonstrates this central dogma of biology. Proteins are the key regulators of all the processes in cells. During cancer, a compounding of several abnormal protein levels in the cell eventually leads to uncontrolled cell growth through a complex network of pathways, resulting in tumors. One such example of a few pathways involved in breast cancer is shown in Figure 2.3. The entire process, originating from the DNA, transcription into RNA,

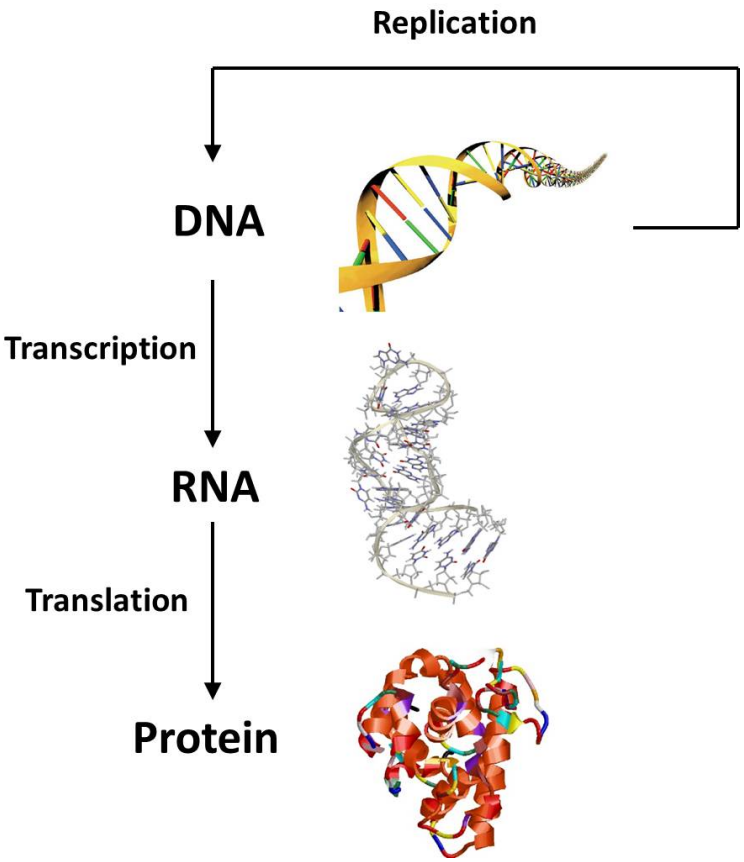

Figure 2.2: The central dogma of biology.

and translation into proteins, is affected by cancer progression. Sensitive and robust detection of any of these molecules (loosely termed biomarkers) in either human blood or in cancer tumors, offers valuable information which can be used both for early detection of disease and for evaluation of the efficacy of cancer treatment strategies. Various sequences of microRNA, short (21-23 base pair) nucleic acid molecules, have also been shown in the last decade to be important cancer biomarkers [5–8]. MicroRNA are important in cells because they can downregulate gene expression by affecting the translation process via inhibiting or degradation of messenger RNA molecules originally slated for production of various proteins.

Biosensors are important for cancer and other various diseases for many reasons:

- They can offer important patient information to physicians to assist in making critical decisions

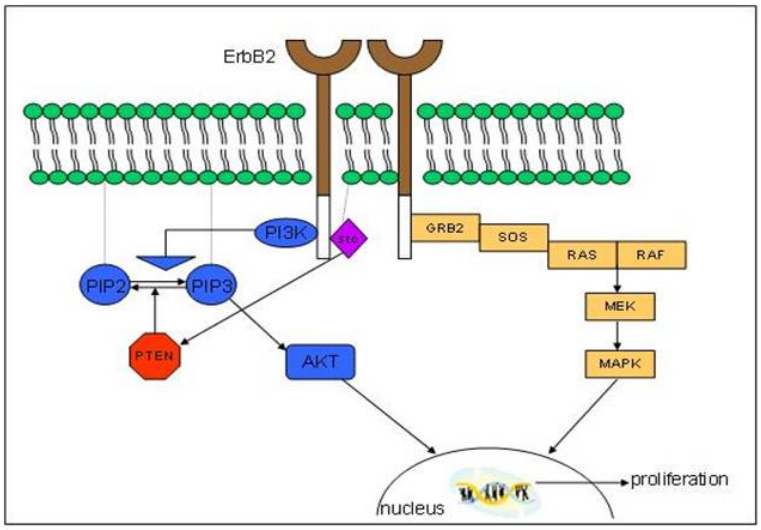

Figure 2.3: Pathways involving the HER2 protein in the progression of breast cancer. From Sue Clare's group at IUSOM.

- They can assist in reverse engineering the body: the mapping and deconvolution of the complex pathways that cause disease
- They can contribute to understanding of cells and living organisms at a molecular level
- They can assist in drug screening by evaluating the efficacy of treatments

The ultimate vision for biosensors would be the capability to have a biosensor at every decision point in the entire body constantly monitoring the expression level and conformation of all the relevant DNA, RNA, and proteins in the processes and pathways. If such information were possible to acquire, the grand mystery of molecular interactions of the human body would be understood almost completely, which would inevitably translate into treatments with maximized efficacies.

2.1.2 Criteria for Evaluating Biosensors

Several important criteria are important for evaluating a biosensor device:

- Cost: As is the case with any technology, cost is a huge concern and should be kept as low as possible. If the per unit cost can be brought

down far enough, then disposable one-time use devices can be made possible, which have inherent advantages particularly in the medical field where concerns of contamination are paramount.

- Accuracy: Accuracy refers to the metric of how closely the device results correlate to the current accepted gold standard. For truly groundbreaking technologies which break the limits of gold standards, accuracy can often be very difficult to evaluate.

- Robustness: Robustness is a very important criterion that can often be overlooked. Since these devices inherently must interact with fluidic biological environments, device lifetime and performance degradation are serious concerns that must be considered. Devices must maintain adequate performance characteristics for the life of each experiment.

- Reliability: Reliability refers to device repeatability and device to device variation. For a technology to be scalable, the same experiment on the same device or a similar device should yield comparable results. Any variation from device to device or experiment to experiment increases the noise of the overall system.

- Use of a label: Many biosensors use techniques which require a modification of the target analyte with some sort of label. The most common examples of this are fluorescence based techniques. Ideally, label free techniques are preferred. Labeling can be very heterogeneous as well as detrimental to target-analyte interactions, reducing the sensitivity and accuracy of the measurement [9, 10].

- Sensitivity: Sensitivity is defined as the lowest concentration of the target analyte that can be detected with confidence. Typically, with a rule of thumb of greater than 3 times noise acceptance, sensitivity can be defined by:

$$Sensitivity = \frac{3 * Noise}{Signal} \tag{2.1}$$

where the Signal is the transduced response monitored at the output for a positive event and the Noise is the average transduced response

monitored at the output for all negative events. Sensitivity to lowest concentrations possible is always desirable for any biosensor.

- Selectivity: For any sensor, false positives and false negatives are serious considerations. Selectivity can be defined as:

$$\frac{\textit{Signal induced by a positive event}}{\textit{Signal induced by the most prominent negative event}} \tag{2.2}$$

  Selectivity should be as high as possible to ensure that the entity being detected from the transducer has indeed triggered the response, and not a mismatch molecule.

- Dynamic Range: Dynamic range refers to the concentration range of the target analyte that is detectable by the sensor. Often high dynamic range and high sensitivity levels are difficult to achieve simultaneously. A high sensitivity layer implicitly implies a large signal change for a relatively small concentration of analyte, but a high dynamic range requires that the device respond to not only small concentrations but much large concentrations. Ideally, a sensor should have as large a dynamic range as possible.

- Interrogation Volume: This refers to the minimum volume that must be placed on the sensor to achieve a result. Minimal volumes are always desired to minimize invasiveness to the patient and costs.

- Time to Result: This is one of the most critical parameters, which describes the time from when the sample is placed on the sensor to when meaningful results are available to the user. This includes both the time for the machine to output raw data and the time to analyze this data so that useful information can be extracted. This time is often the critical chokepoint for the feedback cycle for patient treatment, and if too high it can limit the number of treatments a physcian can employ with a patient.

An ideal biosensor will have the best case scenario for all of these characteristics. They will be referenced repeatedly throughout this dissertation as they quite neatly sum up the overall goals for any biosensor device.

2.2 Next Generation Sequencing

Since the first full sequencing of the human genome in 2001, there has been a race to decrease the cost of human sequencing. Costs have been so dramatically reduced that as of late 2011, it is possible to fully sequence the human genome, transcriptome, and exome for as low as $3600 [11]. A pilot study 2011 demonstrated that the entire process of sequencing, data processing, and treatment planning can be accomplished in 24-30 days [12]. With such an ease of sequencing, the possibility of truly personalized diagnostics for disease treatment has become quite feasible. Figure 2.4 shows a flow for the treatment of patients. When a patient comes in for treatment, the entire genome, exome, and transcriptome can be sequenced. Doctors can look for mutations in certain known specific genes, hundreds of which are known to be correlated to various cancers. These genes are continuously being investigated and documented in many databases, the most prominent of which is the Catalog of Somatic Mutations in Cancer (COSMIC) from the Sanger Institute for Cancer Research. At this point, a board of doctors can meet to decide on a personalized cancer treatment program for the patient, targetted specifically at the mutations that were found in the sequencing results. Such a "sequence everything" approach of tailoring treatment to each individual will truly revolutionize medicine, beginning with cancer but extending to many types of disease.

Two main companies have been competing for the sequencing market, Illumina and Ion Torrent (which is a subsidiary of Life Sciences). Illumina employs fluorescence based techniques for sequencing, using methods very similar to the original Sanger sequencing demonstrated in 2001. Ion Torrent uses novel FET technology very similar to that described in Section 2.4.5 to accomplish sequencing by synthesis [13].

The two obvious information holes in the sequence everything approach are lack of protein and microRNA information. Sequencing obviously refers only to nucleic acids, but so much useful information can be obtained by monitoring protein levels, which ultimately are what regulate cell activity and result in the repression or stimulation of cancer related pathways. Sequencing is just one part of the puzzle — a quite important part, but not the entire story. Methods that would enable the full profiling of not only the relevant DNA and RNA, but also important cell communication proteins,

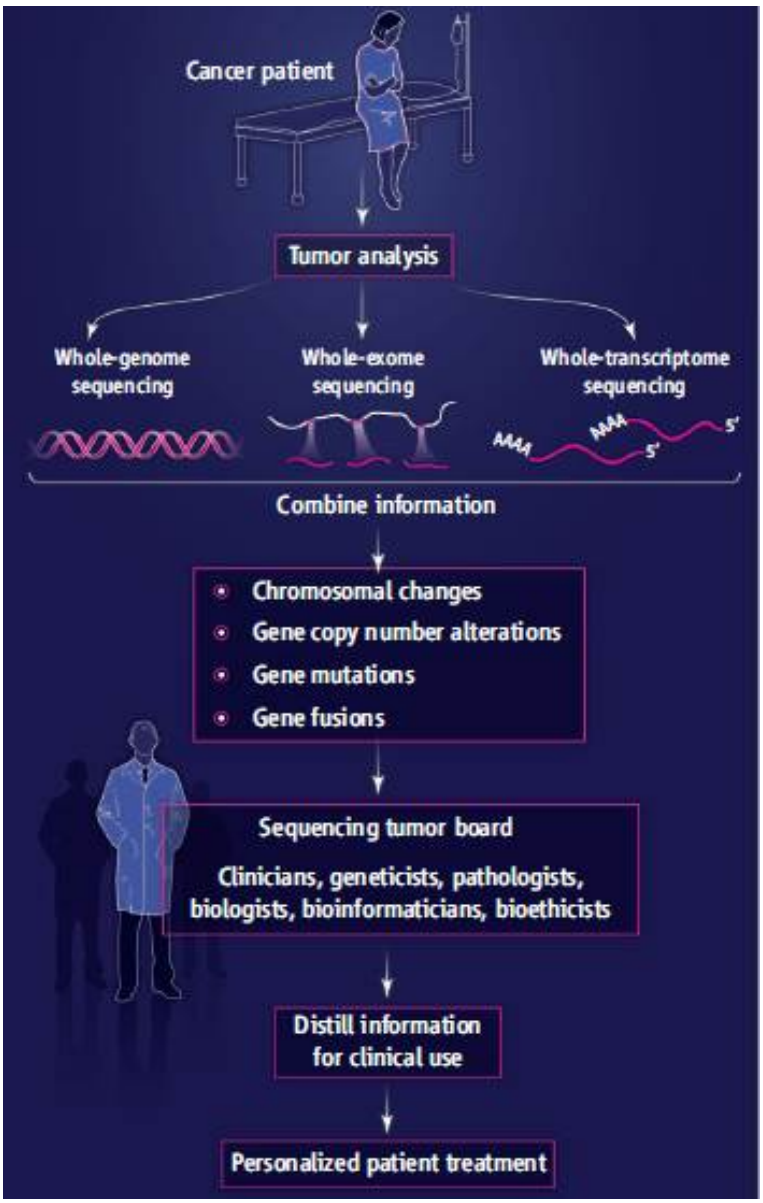

Figure 2.4: Schematic demonstrating the"sequence everything" approach, from [11].

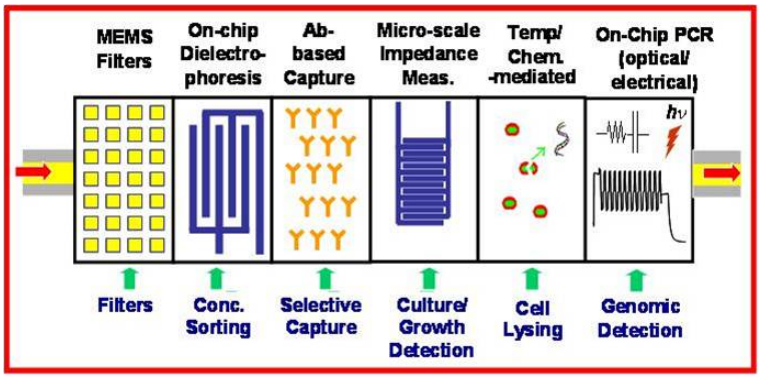

Figure 2.5: Schematic illustrating the components of a typical lab-on-a-chip device. From [20].

cancer biomarkers, microRNA, and other various important molecules, could allow us to fully de-convolute processes in the human body, both cancerous and non-cancerous.

2.2.1 Point-of-Care Biosensors

Point-of-care biosensors, with miniaturization of almost all biosensor components, have the potential to optimize most, if not all, of these critieria [3, 14]. Point-of-care (POC) devices may be defined as testing at or near the site of patient care whenever it is required [15, 16]. Typically, functions normally performed with bulky laboratory equipment are ported onto miniaturized ''lab-on-a-chip" systems with much smaller components and sample volumes. POC diagnostics can provide results rapidly, reducing the turnaround time for results in critical care situations [17]. Moreover, POC diagnostics enable the patient to be more in control of monitoring their own therapy and complying with their care regimen [18], leading to greater patient satisfaction and improved clinical outcome [19].

A schematic for a point-of-care, or lab-on-a-chip system is shown in Figure 2.5. Lab-on-a-chip devices are much smaller than their counterparts, which typically increases sensitivity, decreases costs, decreases sample volumes, and shortens diagnosis times.

POC devices have had a few major success stories, including the widespread home pregnancy test, the portable glucose monitors available from Abbot, and their similar gas and ions monitoring systems for detection from blood

Figure 2.6: Examples of current commercial point-of-care devices.

(Figure 2.6). Lab on a chip or POC devices have the potential to revolutionize treatment in hospitals, third world countries, and ultimately in the homes of patients across the United States and Europe.

2.3 Sensors with Labels

Though labeling the target analytes is intrinsically undesirable for the reasons mentioned in Section 2.1.2, labeling often leads to increased sensitivity or ease of detection, especially in highly noisy environments. This section will describe various technologies that employ a label for the detection of biomolecules.

2.3.1 DNA Microarrays

DNA microarrays offer an attractive fluorescence based method for determining the presence of certain DNA strands in a fluidic environment. Quite simply, a surface (usually silicon dioxide) is functionalized with an attachment chemistry (typically poly-l-lysine or aminosilanes) to immobilize a large collection of varying known DNA probe sequences in known positions via automated microspotting [21]. After the probes have been dried on the surface,

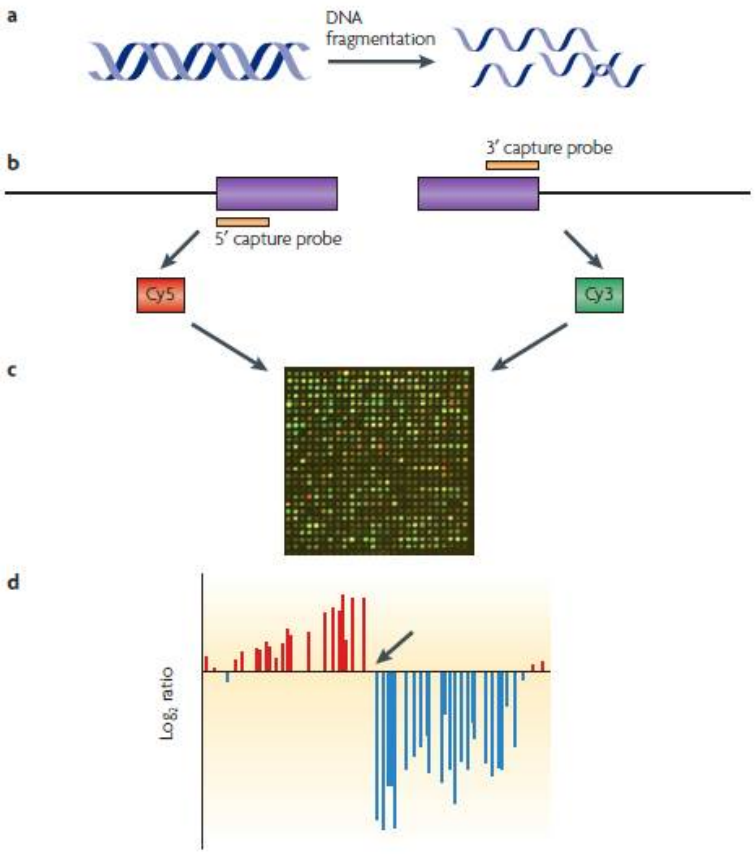

Figure 2.7: Schematic illustrating the use of DNA microarrays, from [22].

fluorescently modified target DNA strands with unknown sequences are introduced to the surface and allowed to hybridize with probes on the surface. If the sequences match with a probe on the surface, the target DNA will be immobilized to the surface and will be seen via a fluorescence microscope or a DNA microarray scanner. This fluorescence then indicates the presence of a specific DNA sequence in the solution. A schematic illustrating this technique is shown in Figure 2.7. Entire genomes can be sequenced using this technique by splitting consecutive pieces of the genome, labeling, and placement on the DNA microarray chips [22–25]. A wide variety of techniques exist for immobilizing the probes on the surface, which can themselves range from cDNA clones [26] to PCR products [27] to very short oligonucleotide strands [28]. The microarrays can be used for detection of single base mutations, specific genome differences in individuals [22], and single nucleotide polymorphisms (SNPs) [29, 30].

The advantages to DNA microarrays include very widespread use, high degree of parallel simultaneous detection, and high sensitivity to even single base mismatches. The main drawbacks to DNA microarray technology are fairly low sensitivity levels (on the order of 100 pM-the nM range) and the requirement for expensive labeling reagents and imaging equipment [22]. However, principles of DNA microarrays, particularly the attachment chemistry, are easily adapted to miniaturized sensors and can be integral in the development of more sensitive DNA biosensors.

2.3.2 Enzyme-Linked Immunosorbent Assays

Enzyme-linked immunosorbent assays (ELISAs) are a widespread and popular method for determining the presence of specific proteins in a solution. ELISAs are widely considered the gold standard for protein detection, and can be loosely thought of as the protein analog to DNA microarrays [31]. ELISAs typically involve at least one antibody with high specificity for a particular antigen of interest. In sandwich ELISA, which is most relevant for protein detection, several steps are performed to determine the presence of the target antigen in the unknown solution:

- A surface is prepared with a known quantity of capture antibody, the probe protein.
- The surface is then blocked with a non-specific blocking agent to passivate any unreacted groups.
- The solution with the target analyte is then placed over the surface, allowing the antigen to bind to the probe molecule.
- The surface is thoroughly washed to remove any unbound antigen or non-specific molecules.
- An antibody specific to the antigen is added to the surface and binds to unreacted sites on the antigen.
- Enzyme linked secondary antibodies are applied as detection antibodies that bind specifically to the antibody's Fc region.
- The surface is once again to remove non-specific enzymes.

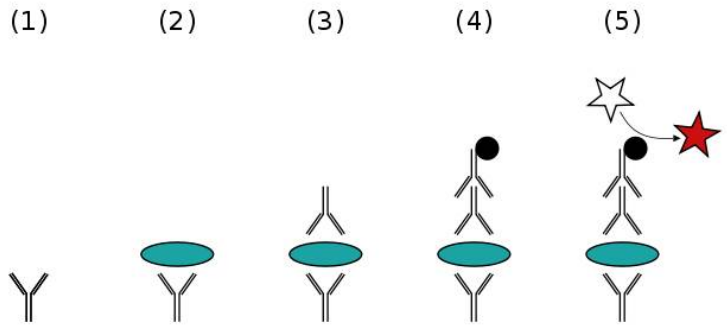

Figure 2.8: Basic schematic illustrating the operation of a sandwich ELISA.

- A chemical is applied that is converted by the enzyme into a color or fluorescent signal.
- The fluorescence or change in color is measured by an external instrument to determine the presence of the target analyte.

This process is illustrated in the schematic shown in Figure 2.8. ELISAs are extremely commonplace in today's research and clinical labs, and have been employed to interrogate for a huge variety of proteins for many applications, including home pregnancy tests. For cancer biomarkers, ELISAs are typically used to validate new technologies as a gold standard. Commonly quoted sensitivity limits for ELISAs range in the 0.5-1 pM range for cancer biomarkers [32, 33]. Disadvantages of ELISA include low sensitivity, difficult preparation, complex steps for analysis, and the need for external lab equipment for detection.

2.3.3 Miscellaneous Label Technologies

Many technologies claim to have high sensitivity to biomolecules with high selectivity to the analyte of interest. However, in the past few years two technologies have demonstrated real detection of target analytes from actual bodily fluids: the integrated blood barcode chip (IBBC) sensor from Caltech University [33], and the Giant magneoresistance (GMR) sensor from Stanford University [32].

The IIBC sensor from Caltech employs a scheme very similar to ELISA and DNA microarrays, discussed in Sections 2.3.1 and 2.3.2, except on a mass

scale and from whole blood. Using the Zweifach-Fung effect, which describes polarized blood cell flow at branch points of small blood vessels [34], whole blood is flown through a low flow resistance primary channel with high resistance channels that branch off at right angles. A critical streamline is created closer to the primary channel wall that connects the branch channels. Large blood cells with radii larger than the distance between this streamline and the channel wall are forced down the primary low resistance channel, filtering them out of the blood. A certain percentage (approximately 15%) of the remaining plasma is passed through the high resistance branch channels. These branch channels contain DNA-encoded antibody libraries (DEAL), which involves using the DNA-directed immobilization of antibodies for conversion of a pre-patterned single stranded DNA microarray into a protein microarray. The specificity of the immobilized probe antibodies to the DNA hooking molecules on the surface was checked with a full orthogonality test. These "probe" antibodies are then used for specific capture of the protein of interest, followed by a biotin labelled detection antibody and a streptavidin-Cy5 fluorescence label for fluorescence detection.

Using this technology, the work was able to demonstrate detection of interleukin-1β (IL-1β) down to less than 1 pM and transforming growth factor (TGF)-β1 down to 30 pM. This was compared to an in house ELISA gold standard, which showed similar sensitivities (0.5 pM for IL-1β). Next, they demonstrated the multiplexed detection of eight plasma proteins from whole blood from clinical patients, shown in Figure 2.9. Using spiked known concentrations of the eight different proteins as a calibration, they were able to back out the concentration of PSA , plasminogen, IL-10, IL-6, IL-1β, and others, simultaneously.

This technology has demonstrated a truly impressive application of protein detection from whole blood. The only main drawbacks of this technology are relatively low sensitivity (only approximately 1 pM or so), the need for a label, and the need for fluorescence detection equipment.

Giant Magneoresistance (GMR) sensors use a very old magnetic technology that was developed for use with read heads in hard-disk drives. The sensors themselves are very simple: they are multilayer thin-film structures that operate based on a quantum mechanical effect where changes in the local magnetic field induce changes in the resistance of the films [35,36]. Using these sensors and antibodies coupled with a magentic bead label, they

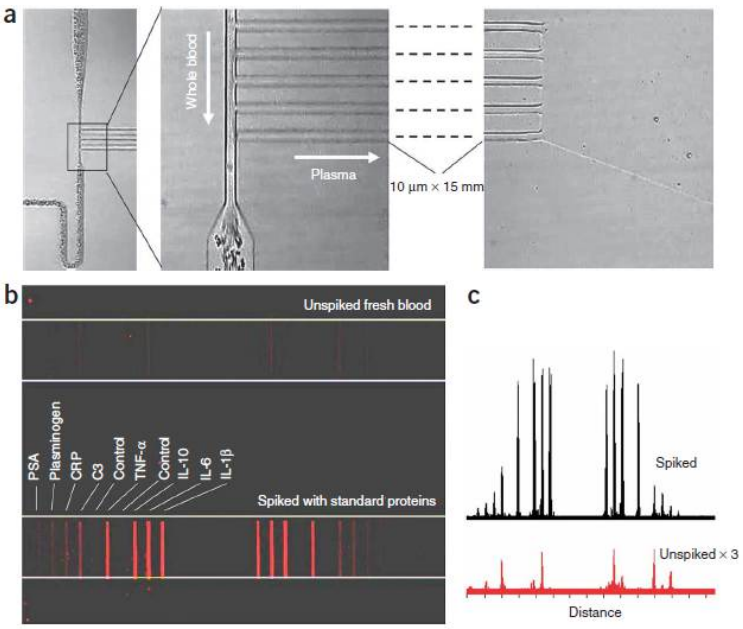

Figure 2.9: a: Microscope pictures of the separation of plasma from whole blood. b: Fluorescent barcode arrays showing detection of the eight proteins. c: Quantification of the results from b. From [33].

are able to demonstrate detection of carcinoembryonic antigen, a colon and breast cancer tumor marker, spiked into PBS down to 5 fM without bead amplification (Figure 2.10). By adding additional magnetic beads for amplification of the signal, they were able to bring this detection limit down to 50 aM. They compared their technology to in-house ELISA of the same protein, demonstrating a wide dynamic range of 5 fM-5 nM, compared to ELISA's dynamic range of only 1 pM-100 pM.

Using this technology, they were able to demonstrate the multiplexed detection of BSA, Ltf, Survivin, CEA, and five other proteins in many different fluidic environments, including PBS, mouse serum, lysis buffer, human urine, and human saliva. They took this one step further by monitoring the CEA, EPCAM, and VEGF protein levels in xenograft tumor-bearing mice over time (Figure 2.11). This technology is an example of another real application where protein levels can be monitored directly from bodily fluids. All it lacks are the use of the magnetic label, which could alter protein properties, and a demonstration from human bodily fluids.

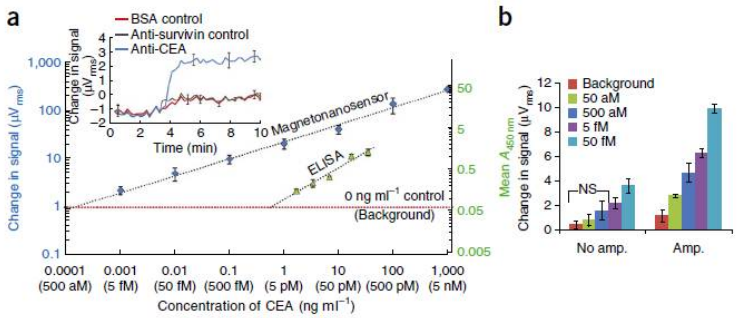

Figure 2.10: a: Concentration curve of response versus concentration of CEA. Dynamic range of 5 fM-5 nM is demonstrated, compared to ELISA. b: comparison of results with and without amplification, showing a detection limit of 50 aM for CEA after amplification. From [32].

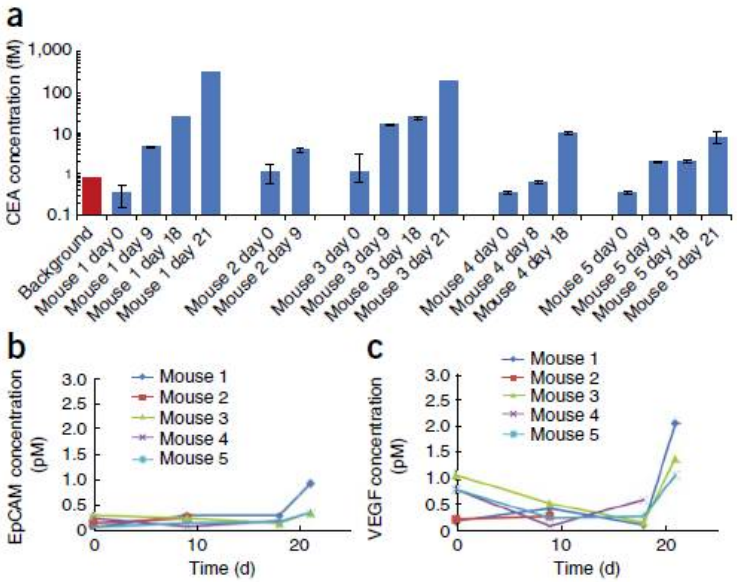

Figure 2.11: Detection over time of CEA, EpCAM, and VEGF from blood from xenograft tumor-bearing mice. From [32].

2.4 Field-Effect Transistor Based Sensors

This section will cover the most relevant background and literature for the rest of the work — that for field-effect transistor biosensors. FET devices refer to the category of devices that use the influence of electric fields at the gate of the transistor on the source-drain current. Most biomolecules are inherently charged depending on their isoelectric point and the pH of the buffer solution. As this charge comes in close proximity with the gate of the FET, the charge influences the surface potential of the transistor, which modulates the carrier concentration and thus the source-drain current. The main benefits of using a FET technology for sensors include:

- High sensitivity due to the inherent gain achieved by the amplification of source-drain current due to surface potential modulation
- Label-free detection due to the charge based detection scheme
- Low per unit cost due to the mass scalability of transistors
- Ease of integration with necessary exterior electronics
- Amenability to scale-up with VLSI design

This section will cover relevant background for FETs in general and a brief examination of the concept of isoelectric point. It will then dive into reviewing the relevant literature for capacitive sensors, ion sensitive field-effect transistor (ISFET) sensors, extended gate FET (EGFET) sensors, nanoscale FET sensors, and finally for work regarding theoretical considerations for bioFETs.

2.4.1 Basic Metal-Oxide-Semiconductor FET (MOSFET) Theory

This section will give a brief overview of basic MOSFET theory with very little reference to biological sensing. The focus will be on relevant basic concepts that will be necessary for understanding FET biosensors.

The simplest form of a field effet device is a two-terminal metal-oxide-semiconductor capacitor (MOSCAP). The threshold voltage for a standard MOSCAP is typically given by:

$$V_t = V_{FB} + 2\phi_f - \frac{Q_s}{C_{ox}} \tag{2.3}$$

with V_{FB} given by:

$$V_{FB} = \phi_{ms} - \frac{Q_f}{C_{ox}} - \frac{Q_{it}(\psi_s)}{C_{ox}} - \frac{1}{C_{ox}}\int_0^{t_{ox}} \frac{x}{t_{ox}}\rho_m(x)dx - \frac{1}{C_{ox}}\int_0^{t_{ox}} \frac{x}{t_{ox}}\rho_{ot}(x)dx \tag{2.4}$$

where:

- Q_f represents the fixed charge in the oxide, considered to all be at the semiconductor/oxide interface
- Q_{it} represents the interface oxide trapped charge, which is a function of the surface potential psi_s
- ρ_m is the mobile charge density, which is distributed throughout the oxide and change position due to applied biases over time
- ρ_{ot} is the oxide trapped charge, which is distributed throughout the oxide

Fixed charge is important because it can cause large shifts in threshold voltage, increasing the voltages needed to turn the device on. For fluidic biosensors, it is especially important to keep this as low as possible because higher voltages will need to higher leakage currents. Interface oxide trapped charge can lead to degradation of device turn-on, as can be seen in Figure 2.12. It can be removed with low temperature H_2 anneals. Both interface oxide trapped charge and mobile charge can lead to instability in CV characteristics of the MOSCAP and thus eventually in the IV characteristics of the MOSFET. Reducing these densities is extremely important to reduce the overall noise of the device. Oxide trapped charge is similar to fixed charge, but is of less concern because it is typically further from the critical oxide-semiconductor interface.

MOSFETs are essentially MOSCAPs with a source-drain terminal that allows current to flow as a function of the surface potential term ψ_s, and therefore the applied gate voltage. The expression for the drain current is well known:

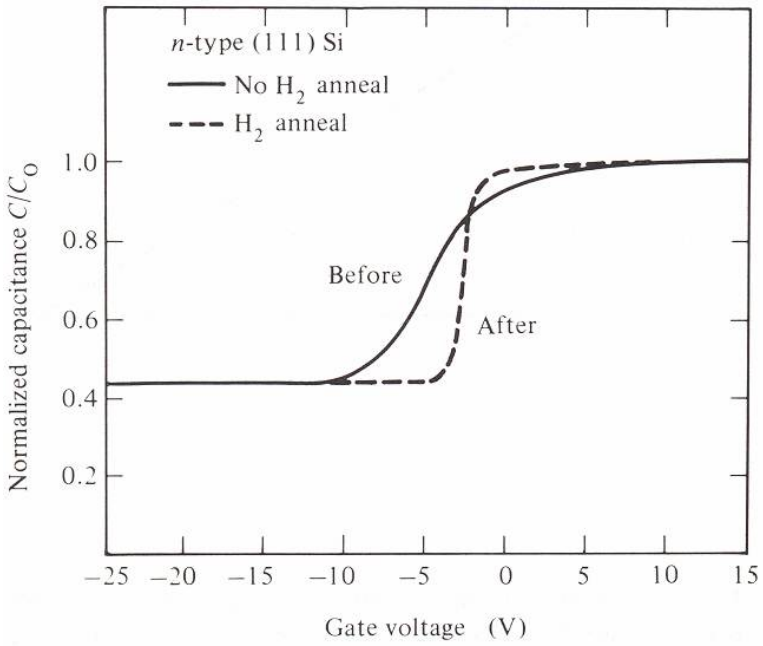

Figure 2.12: CV curves showing the effect of interface trapped charge, from [37].

$$I_d = C_{ox}\mu\frac{W}{L}[(V_{gs} - V_t)V_{ds} - \frac{1}{2}V_{ds}^2] \tag{2.5}$$

for the triode region, when $V_{DS} < V_{DS(sat)}$, where

$$V_{DS(sat)} = V_{GS} - V_t \tag{2.6}$$

For the saturation region, when $V_{DS} > V_{DS(sat)}$, the drain current is given by:

$$I_d = C_{ox}\mu\frac{W}{2L}(V_{gs} - V_t)^2 \tag{2.7}$$

where C_{ox} is the insulator capacitance, μ is the mobility of the carriers, W is the width of the active area, L is the length of the device, V_{gs} is the Gate voltage and V_t is the threshold voltage, which was described in Equation 2.3. What is important to note here is that in the triode region, I_d is proportional to $(V_{GS} - V_t)$, whereas in the saturation region, it is proportional to $[(V_{GS} - V_t)]^2$. Another case to address is when V_{GS} is less than the threshold voltage. This is called the subthreshold region, and here the source-drain current is given by:

$$I_d = \frac{1}{S} e^{(V_{GS} - V_t)} \tag{2.8}$$

where S is the subthreshold slope, and has a physical minimum limit of 60 mV/decade.

The important characteristics of any MOSFET, particularly for biosensing applications, include:

- On-current I_{on}: the max saturation current achieved
- Off-current I_{off}: the current still passing from source to drain when $V_{GS} << V_t$
- Subthreshold slope, S
- Transconductance g_m, which is the change in current due to change in gate voltage above threshold:

$$g_m = \frac{\Delta I_d}{\Delta V_{GS}} \tag{2.9}$$

- Leakage current I_G: the current passing through the gate oxide into the gate electrode
- Repeatability of threshold voltage for many sweeps: this is directly related to the noise of the device
- Threshold voltage spread over many devices

All of these characteristics need to be optimized, typically via various fabrication steps, for both dry MOSFETs and for bioFETs.

2.4.2 Isoelectric Point

The isoelectric point (pI) is the point at which a molecule or surface has a net charge of zero. In buffer solutions at a pH at the isoelectric point of a molecule, the molecule carries zero net charge. As the pH is reduced, then the molecule or surface will start to gain net positive charge — the further away from the isoelectric point, the more net charge the molecule or surface

will have. Similarily for pH values above the isoelectric point, net negative charge will be added to the protein.

The mechanism for the changing charge of the molecule or surface is fairly straightforward. All surfaces or molecules can have individual components (amino acids for proteins, the phosphate backbone for DNA, or functional groups on surfaces) that can experience protonation or deprotonation as a function of the pH of the external environment. At high concentrations of H^+ in solution (low pH), it will be favorable for H^+ to be added to these components, thereby increasing the net positive charge of the molecule. Each of the individual components of the molecule can have a protonation/deprotonation reaction with a certain pKa. The pI of a molecule then, is typically the mean of all the pKas for the relvant charged domains on the molecule or surface. This will be discussed in more detail in Section 2.4.4.

The isoelectric point and the pH of the buffer solution are important considerations when dealing with FET biosensors which are purely charge based. It is critical to know what charge and approximate magnitude of charge will be present on the surface of the biosensor or intrinsic to the analyte being targetted. Most commonly, the charge of proteins can be measured via capillary electrophoresis experimentally [38], which is a very good experiment to perform before attempting to work with any specific protein.

The pI for the DNA phosphate backbone is around 0, meaning that DNA is almost always negatively charged in aqueous solutions. Silicon dioxide has a pI of around 2-3, aluminum oxide around 8-9, and hafnium oxide around 7-7.5.

2.4.3 Capacitive Sensors

Simple capacitor structures can be used as sensors of biological molecules. In these schemes, typically the top metal gate of a MOSCAP is replace by a fluid gate and an ionic fluid that makes contact to the gate oxide. Capacitance can then be measured from the fluid gate to the bulk, or capacitance-voltage curves can be measured. As molecules bind to the surface of the gate oxide, the surface potential (ψ_0) changes, which will change the surface potential in the silicon (ψ_s) and thus the carrier concentration in the silicon, which affects the overall measured capacitance. This technique fails to take advantage of

the transconductance and subthreshold gain of a MOSFET device.

Using such structures, the detection of DNA hybridization and of small molecules has been demonstrated [39]. Polymerase chain reaction (PCR) products have also been monitored in a label-free fashion [40], and this has been integrated with a PCR chamber on the same chip [41]. 12-mer oligonucleotides have been detected down to 2 nM with a planar device [39]. The same scheme was also used for the detection of heparin, a blood coagulant and its small molecule derivatives down to nM concentrations [42].

High-k dielectrics have been utilized in this scheme as well to increase the response seen by the sensor. The charge induced in the silicon (and thus the capacitance) is a linear function of the gate oxide capacitance. Bulk field-effect transducers with a functionalized Al_2O_3 gate were shown to successfully detect dopamine down to 70 μM and tyrosinase down to 0.25 enzyme units [43]. The same device also was used to monitor the phosphorylation of a peptide by casein kinase II with a detection limit of 1.5e-3 U/mL. Successful regeneration of the surface could be achieved with the treatment of alkaline phosphatase [44]. Another example of DNA hybridization down to 3 μM was demonstrated with a similar sensor [45]. Hafnium oxide, which has a gate dielectric of around 20-25, was shown as a gate dielectric for a similar capacitive sensor for detection of streptavidin down to 48 μg/mL, which corresponds to slightly less than 1 μM [46]. Sample CV curves showing the shift due to the binding of streptavidin are shown in Figure 2.13.

Though capacitive sensors are good proofs of concept that the binding of biomolecules can cause shifts in the surface potential in fluid that can then induce changes in charge in the semiconductor, the sensitivity limits are typically quite high. This is predominantly because such architectures fail to take advantage of one of the most attractive characteristics of the FET design, the high current gain as a function of applied gate voltage.

2.4.4 Ion-Sensitive-Field-Effect Sensors (ISFETs)

The first documented use of a field-effect device in fluid for sensing was demonstrated by Bergveld in 1970 [47]. Since then, a plethora of research articles, reviews, and products have spawned from the base technology. Perhaps the most successful story has been the now widespread use of the tech-

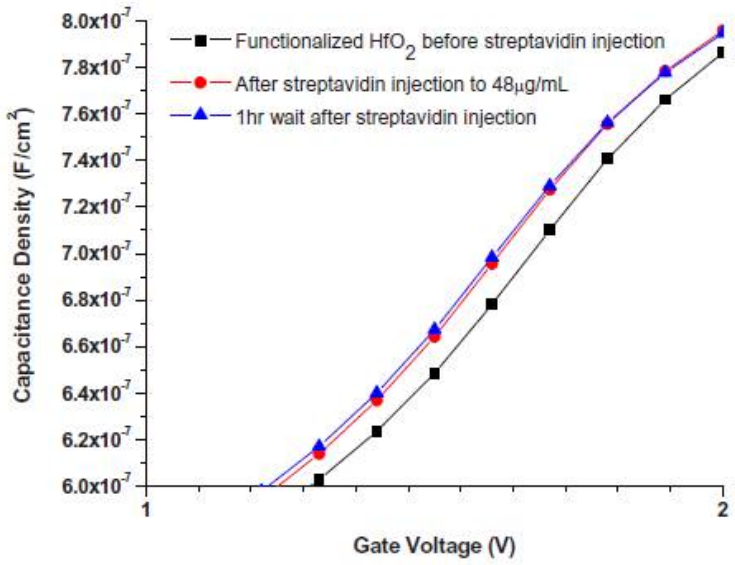

Figure 2.13: Shift due to the binding of streptavidin on CV curves on a hafnium oxide capacitive sensor, from che10b

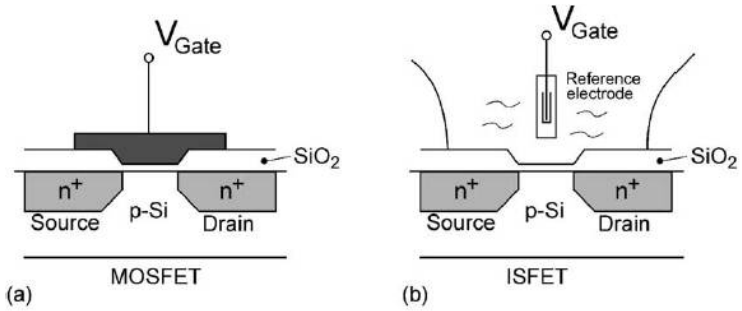

Figure 2.14: Schematics comparing an ISFET to a MOSFET, from [48].

nology for electrical pH sensors. The basic difference between an ISFET and a MOSFET is demonstrated in Figure 2.14. An ISFET is essentially a MOSFET where the top metal gate is replaced by an ionic fluid and a reference electrode. This leads to a few important differences that will be discussed in this section.

Remarkably, nearly all of the equations discussed in Section 2.4.1 still hold. All of the MOSCAP equations with the exception of the equations for threshold voltage and flatband voltage are directly applicable for ISFETs. Equations 2.5 and 2.7 still hold without modification. The main difference between the ISFET and MOSFET is quite intuitive: the metal gate in a MOSFET is

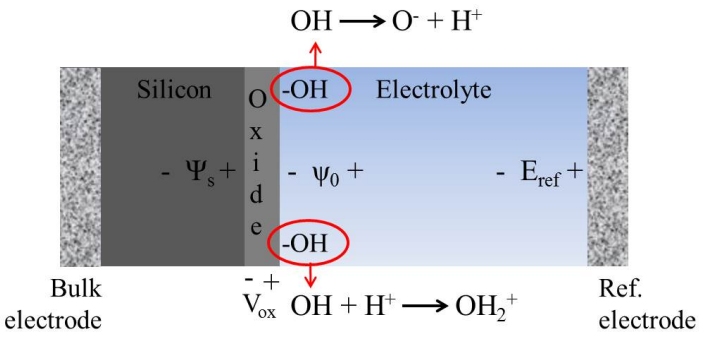

Figure 2.15: Schematic showing the potential drops in an ISFET system.

replaced by a system consisting of the reference electrode in solution and the fluid that connects the reference electrode to the gate dielectric. The main difference then is a modification of the equation for flatband voltage:

$$V_{FB} = \phi_{ms} - \frac{Q_{eff}}{C_{ox}} \tag{2.10}$$

where we are using the short form for convenience. For an ISFET, the ϕ_{ms} term is replaced by a few terms that describe the potential drops:

$$V_{FB} = E_{ref} + \chi^{sol} - \psi_0 - \frac{Q_{eff}}{C_{ox}} \tag{2.11}$$

These terms are illustrated in Figure 2.15. E_{ref} is the reference potential drop which is present for any electrode in solution, and which should be independent of pH for a proper reference electrode. χ^{sol} is the surface dipole potential of the solvent, and is very similar to the electron affinity of silicon mentioned previously. ψ_0 is the potential drop at the surface of the gate dielectric as before. From Figure 2.15 and Equation 2.11, we can write the equation for the threshold voltage of the ISFET:

$$V_t = E_{ref} + \chi^{sol} - \psi_0 - \frac{Q_{eff}}{C_{ox}} + 2\phi_f - \frac{Q_s}{C_{ox}} \tag{2.12}$$

Of all of these terms, the only term in theory that should be affected by changes in pH or charge at the surface is the ψ_0 term, a fluid surface potential term which is a strong function of all the charge directly at the gate dielectric surface. Any shifts in pH or addition of charge in solution, then, will affect only ψ_0, and a one-to-one relationship between shifts in ψ_0

and the threshold voltage from Equation 2.12 should be observed. In reality, however, other terms in Equation 2.12 can also be dependent on solution pH — most notably E_{ref} can vary if the reference electrode is not perfect and additional charge in the Q_{eff} term can be added upon ion incorporation into the gate dielectric from the fluid. Normal I_dV_d curves can be measured as function of the applied reference voltage as well as the solution pH, which serves directly as an adjustment of the surface potential of the device.

The sensitivity of the fluid surface potential to pH (and thus to the V_t of the ISFET) can be shown to be modeled by:

$$\Delta\psi_0 = -2.3\alpha\frac{RT}{F}\Delta pH \tag{2.13}$$

with

$$\alpha = \frac{1}{(2.3kT/q^2)(C_s/\beta_s)+1} \tag{2.14}$$

where R is the universal gas constant, T is the temperature in Kelvin, q is the charge of an electron. β_s is the surface buffer capacity, which is the ability of the oxide surface to deliver or taken up protons given a change in pH at the surface, and is given by [49]:

$$\beta_s = -\frac{1}{q}\frac{\delta\sigma_0}{\delta pH_S} \tag{2.15}$$

where σ_0 is the surface charge per unit area and pH_S is the local pH right at the surface. C_s is the differential double-layer capacitance, or the ability of the electrolyte solution to adjust the amount of stored charge as a result of a small change in the electrostatic potential:

$$C_s = -\frac{\delta\sigma_{DL}}{\delta\psi_0} = \frac{\delta\sigma_0}{\delta\psi_0} \tag{2.16}$$

where σ_{DL} is the charge in the fluid double layer. As can be seen from Equation 2.14, α is a dimensionless parameter that has a maximum value of 1. For α=1, Equation 2.13 reduces to $2.3(RT/F)\Delta pH$, which translates to a maximum Nernstian pH sensitivity of 58.2 mV per pH at 20 °C. As can be seen from Equation 2.14, an α value of 1 is achieved with higher surface buffer capacities and lower differential double-layer capacitances. These are properties of the surface - in the case of ISFETs, of the gate dielectric. The

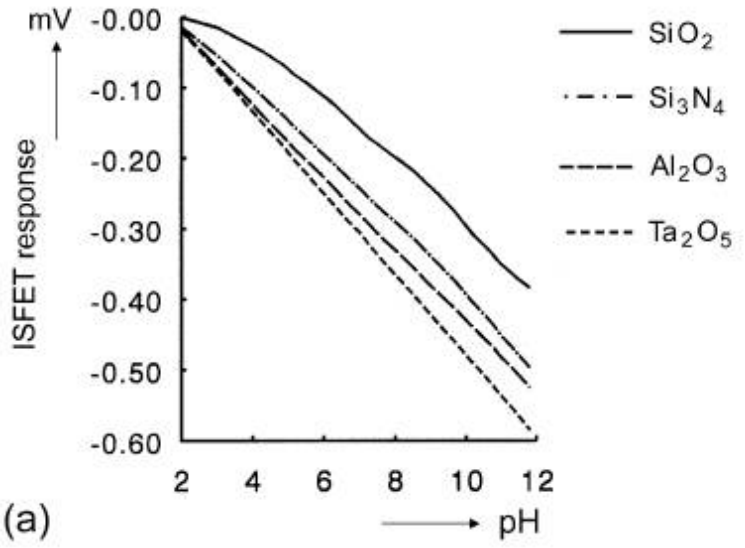

Figure 2.16: The response of four ISFETs with different gate dielectrics to changes in pH, from [48].

pH responses for ISFETs with four different gate dielectrics are shown in Figure 2.16. Tantalum oxide exhibits the best pH sensitivity, followed by aluminum oxide, silicon nitride, and silicon oxide, again due to differences in β_s and C_s.

This theory is intended mostly for ISFET response to pH, but can be altered to account for biomolecules that attach in solution. The situation becomes more difficult because it is often times extremely difficult to judge how close biomolecules can really approach the surface and thus how much they will influence ψ_0.

ISFETs for the detection of pH are extremely well established. Several works have shown the repeatable detection of pH close to the Nernstian limit [48,50–57]. Typically, the ISFET can be combined with sometimes complex biasing circuits to integrate the signal processing electronics with the sensor, taking full advantage of the integratability of the technology. Much less work has been on biosensing of molecules [58–62], with sensitivites typically in the μM range. In one interesting work of note, the researchers used a CMOS chip fabricated by a real foundry (Taiwan Semiconductor Manufacturing Company), etched back all of the excess metal and interlayer dielectric layers, including the polysilicon gate, to expose the gate dielectric [63]. The gate dielectric in this case was silicon dioxide, only a few nanometers thick.

They showed detection of dopamine down to the fM range using a sophisticated feedback circuit integrated with the ISFET that could bias the device to maximize sensitivity and to measure threshold voltage as a function of time. Much progress has also been demonstrated towards theoretical models of the ISFET response to pH [48, 49, 64]. Most of this theory is directly translatable to Nanoscale bioFETs, and so is very important to understand and apply correctly.

2.4.5 Extended Gate Field-Effect Sensors (EGFETs)

EGFETs are a subgroup of ISFETs that are essentially MOSFETs with either a floating metal gate or a dielectric on top of the floating metal gate is the sensing membrane [65, 66]. EGFETs offer the following possible advantages over ISFETs:

- Protection of the gate dielectric from potentially harmful ionic solutions, especially over time where ions from the solution can be incorporated in the gate dielectric.
- Ease of integration with VLSI CMOS circuits, where the gate is an important step of the process that is very difficult to extricate in a scalable fashion.

With these two advantages, work has been demonstrated showing the increased stability of such extended gate devices over time as well as true integration with many devices simultaneously detection pH changes or moelcular events as well as complex amplification and signal processing electronics [67–71]. Sensitivities to pH changes are typically less than counterpart ISFET devices (on the order of 40-50 mV/pH), most likely due to the existence of parasitic capacitances due to the lead length from extended gate to the actual transistor channel [72]. Arrays of devices have been demonstrated to be capable of monitoring extracellular potential changes of cells, taking full advantage of the scalability of the technology [67]. EGFETs can also enable the possibility of integration with geometries that are not typically compatible with the FET. For example, the extended gate can be placed into an etched microfluidic channel removed from the transistor itself [73]. Using

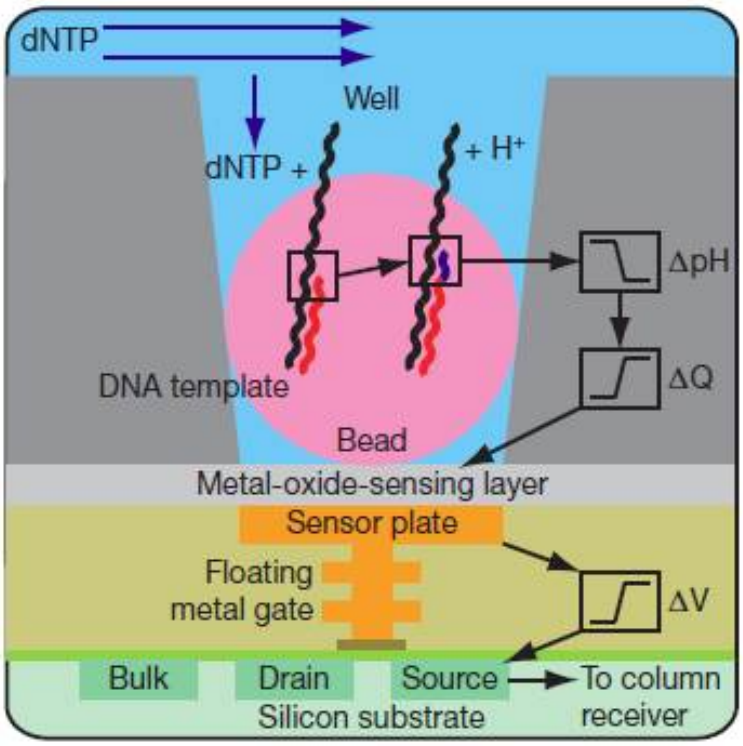

Figure 2.17: Schematic demonstrating the cross section for one EGFET device from the Ion Torrent chip, from [13].

such a structure, biotin-streptavidin binding has been detected via a change in dielectric constant [73].

The most prominent demonstration of the use of EGFETs has been Ion Torren's work in Nature in 2012, an example of a next generation sequencing instrument that uses the FET technology [13]. Their technology shows true integration of millions of CMOS devices on the same chip for use in sequencing, a real world demonstration that the FET technology can find direct use in a biomedical application. Briefly, their technology uses extended gate field-effect transistor devices with a Ta_2O_5 sensing membrane layer for the detection of shifts in pH (Figure 2.17). PCR beads containing DNA template molecules and DNA polymerase are introduced into wells above each device containing shjort strands of DNA to be sequenced. One by one, the four dNTPs are introduced to the well. If the dNTP flown in matches the next base pair to be copied in the DNA strand, the polymerase binds to the DNA, initiates a copy, and protons are released into the solution. This lowers the overall pH of the solution, which modulates the source-drain current as

described in Section 2.4, allowing for detection of the binding event. From this, the strand can be sequenced base by base. In their 2011 Nature paper, Ion Torrent demonstrated the full sequencing of Gordon Moore's DNA with 10.6 fold coverage. This sequencing effort was compared to a gold standard using the ABI SOLiD sequencing, and was found to be over 99.95% accurate.

2.4.6 Nanoscale Field-Effect Sensors

Nanoscale field-effect sensors are simply ISFET sensors that have been scaled down to the nanoscale. By virture of reducing the size of the devices to orders of magnitude close to the molecules to be detected, sensitivity limits can be vastly improved, with the possibility of eventual single molecule detection. ISFETs have been around for nearly four decades by the time of this work. In the last 11 years, renewed interest has been kindled in the FET sensing area, sparked by a landmark Science publication in 2001 [74]. In this work, silicon nanowires 20 nm in diameter were grown using a bottom-up approach using vapor-liquid-solid (VLS) growth, which uses nanoscale metal particles as catalysts on a semiconductor substrate to grow the nanowires. Such an approach is deemed "bottom-up" since the nanowires are grown and individually flow aligned instead of being defined via lithography or some other top-down technique. Bottom-up approaches are notoriously difficult to scale to mass manufacturing. In this work, the silicon nanowires were flow aligned to an oxidized silicon substrate and contacted on either end with metal leads to form the source and drain contacts. By functionalizing the silicon dioxide gate dielectric with aminopropyltriethoxysilane (APTES), they were able to demonstrate linear response to changes in pH over values from 2-9 by measuring the conductance of the device with an AC measurement technique. Such a technique applies a small AC voltage on top of a DC bias to the drain of the device, and measures the resulting impedance/conductance of the device using a lock-in amplifier. This conductance changes upon binding of surface charge to the device, indicating a change in pH or binding event. The devices were then functionalized with biotin and used for the detection of streptavidin down to 25 pM. These results are illustrated in Figure 2.18. It is important to note here that after the introduction of streptavidin, the measured conductance increases and stabilizes even after washing with

a pure buffer solution in a subsequent step. This work demonstrated the first nanoscale biological detection of molecules as a proof of concept. The lower limit of sensitivity is comparable to or even slightly worse than what is possible with ELISA today. It is difficult to evaluate the real limit to their detection, however, because of a lack of discussion of the noise they experienced with the devices, making it impossible to determine their signal to noise ratio for both pH detection and for molecular detection.

Scott Manalis's group at MIT published in 2002, showing DNA detection down to 2 nM with an electrolyte-insulator-semiconductor (EIS) structure which was essentially a capacitive structure like that discussed in Section 2.4.3 with a multi-layer poly-L-lysine/DNA structures, where repeated exposure to PLL/DNA layers was repeated while the surface potential was being monitored via capacitive measurements with a Ag/AgCl fluid electrode [39]. They showed detection of a DNA strand matched to the probe on the surface as well as lack of signal for a mismatch. It is important to note that using the PLL attachment strategy for the DNA, it is expected that the DNA phosphate backbone will lie horizontally on the surface, allowing most of the charge to be in close contact to the channel of the device.

Charles Lieber's group at Harvard published the detection of single-stranded DNA in NanoLetters in 2004 with a similar device architecture, demonstrating detection down to 10 fM [45]. Peptide nucleic acid (PNA) molecules were used as the probe molecules on the SiO_2 surface for higher affinity to the single stranded DNA. Their first concentration versus response curve is shown in Figure 2.19 for two different nanowire devices.

Lieber's group also published the detection of single viruses in PNAS in 2004. By functionalizing their SiNW devices with antibodies complementary to influenza type A virus, they were able to image in real time as fluorescently modified virus particles passed their sensors while simultaneously observing changes in conductance (Figure 2.20) [75]. Responses as high as 20-40 nS were observed for single virus particles in a solution of concentration 100 virus particles/μL of solution. As the virus particles left the vicinity of the devices, they observed a return of the original conductance value.

Williams's group at Hewlett-Packard Laboratories demonstrated the first top-down fabrication of nanowire structures on silicon-on-insulator (SOI) wafers in 2004 [76]. The top silicon was patterned via e-beam lithography followed by reactive-ion-etching (RIE). The devices were 50 nm wide, 60 nm

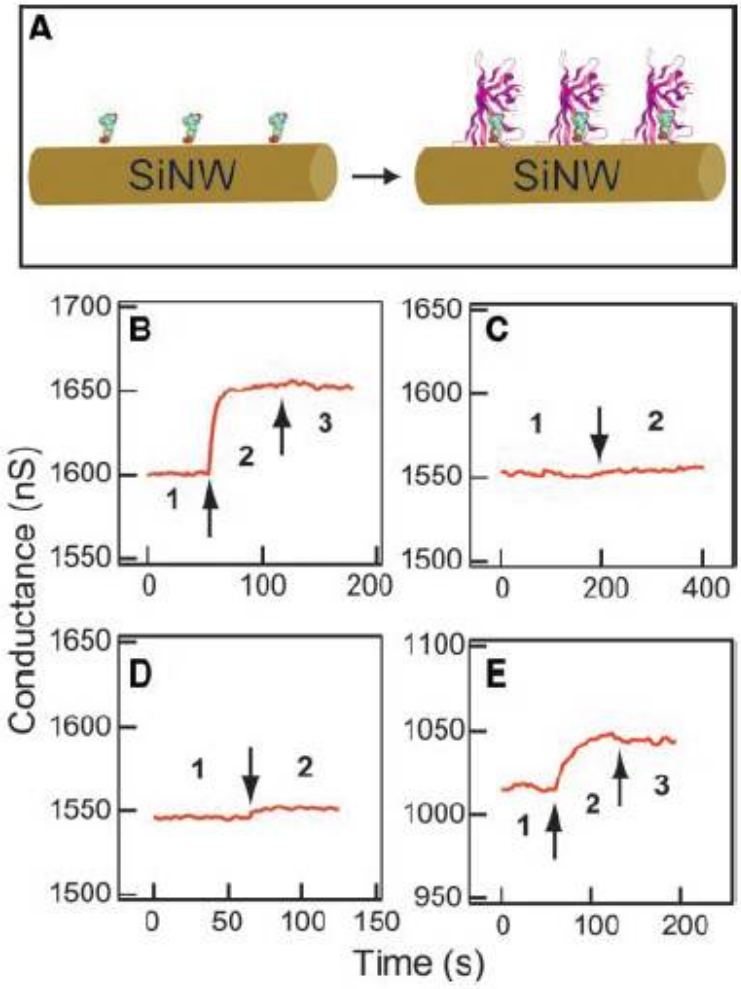

Figure 2.18: The response of biotin-functionalized silicon nanowire devices to streptavidin. A: Schematic of the binding of streptavidin to a nanowire. B: Conductance versus time where region 1 is a buffer solution, region 2 is the addition of 250 nM streptavidin, and region 3 is a buffer wash. C: Conductance versus time for an unmodified FET showing no response to streptavidin. D: Conductance versus time for a biotin-modified FET, but to streptavidin pre-blocked with biotin. E: Conductance versus time for 25 pM streptavidin. From [74].

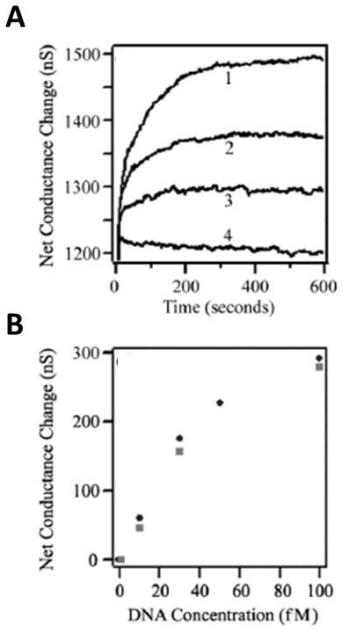

Figure 2.19: Detection of single stranded DNA. A: Conductance versus time when exposed to (1) 100 fM, (2) 30 fM, (3) 10 fM, and (4) 1 fM of single stranded DNA. B: Conductance change versus concentration for the four different concentrations, with 2 different devices (square and circle). From [45].

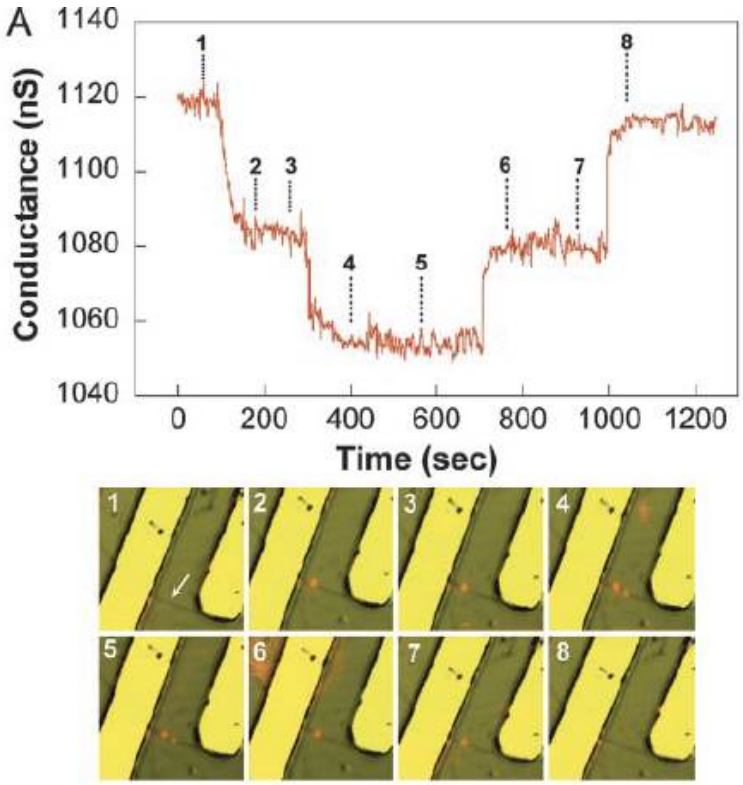

Figure 2.20: Detection of single virus particles. Top: Conductance versus time as virus particles pass by the sensors. Bottom: Merged bright field and fluorescence pictures of the virus particles as they pass by the wire, showing that the change in conductance corresponds to proximity of the virus to the wires. From [75].

high, and 20 μm long, with 3 nm thick silicon dioxide as a gate dielectric. Using a vapor deposited silane layer, they linked probe DNA to the surface and introduced complementary DNA while monitoring the conductance of their wires. Detection as low as 25 pM DNA solution was demonstrated.

In 2006, Lieber's group demonstrated the multiplexed detection of three cancer biomarker proteins: PSA-α1-antichymotrypsin (down to 2 fM), carcinoembryonic antigen (down to 0.55 fM) and mucin-1 (down to 0.49 fM) [77]. Nanowire devices were both p and n-type on the same chip, and were functionalized with an aldehyde propyltrimethoxysilane layer. The aldehyde group was then coupled to antibodies with high affinity for the target protein of interest by spotting the different antibodies on the same chip on different nanowire devices. They were able to flow solutions containing just one protein one by one, and saw responses only to the devices functionalized with the relevant antibody, with very little changes in conductance for the mismatched proteins. Even further, they were able to detect 0.9 pg/mL of PSA spiked in donkey serum without any purification steps, and even the PSA from unpurified human serum. These results are illustrated in Figure 2.21. Interestingly, the conductance signals after wash steps returned to the same baseline value, which is puzzling if the proteins are indeed covalently binding to the surface.

In 2007, Mark Reed's group at Yale University demonstrated the first comprehensive results with a top down, CMOS compatible fabrication process [79]. They used silicon-on-insulator (SOI) wafers, defined their nanowire sensors with e-beam lithography, and etched the silicon patterns in the top silicon with an anisotropic wet etchant, tetra-methyl-ammonium-hydroxide (TMAH). This resulted in nanowires that were 50 nm in width and 25 nm in thickness. The devices employed native silicon dioxide as their gate dielectric, but were shown to have very limited lifetimes in fluidic environments and low stability levels. Using an open PDMS well in contrast to the microfluidics of the Lieber group, they used two tubes (one input and one output) to exchange all fluids. The devices exhibited stepwise pH resolution as they could change the pH in real time and monitor the source-drain current. Using these top down devices, they demonstrated the detection of streptavidin down to 10 fM, and showed negative controls of quenced streptavidin that did not bind to their biotin functionalized surface. Streptavidin binding was additionally confirmed via fluorescence images. Finally, they demonstrated

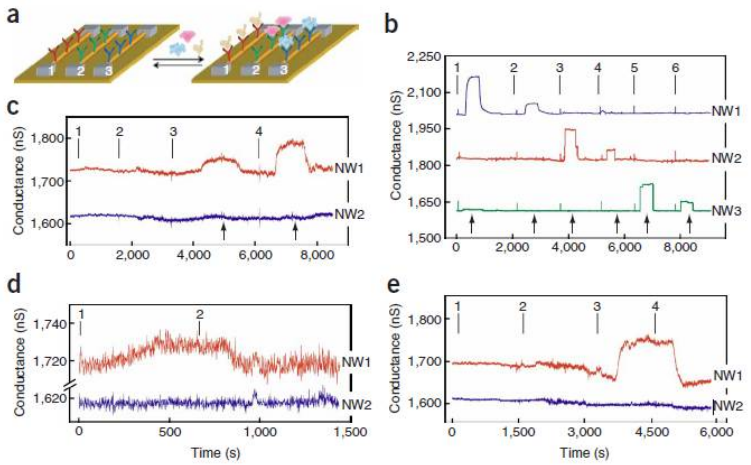

Figure 2.21: Multiplexed sensing of proteins. a - Schematic showing different antibodies on different devices. b - Conductance versus time for the introduction of PSA, CEA, and mucin-1 sequentially over three different devices functionalized with three different antibodies. c - Donkey serum containing PSA. d - Donkey serum spiked with 90 pg/mL of PSA. e - human serum containing PSA. From [78].

detection of mouse immunoglobulin G (IgG) and mouse immunoglobulin A (IgA) by functionalizing their devices with probe molecules (goat anti-mouse IgG and goat anti-mouse IgA). They were able to detect these large proteins down to 100 fM, by monitoring the source-drain current in real time as the solution was introduced to the chip. They showed the cross talk between these two proteins, and observed a signal only when the matched proteins were introduced to the substrate. PEG also provided another negative control, yielding no change in current. An SEM image of one of their devices and the protein detection results can be seen in Figure 2.22.

In 2010, Reed's group used their platform for detection of important antibodies from whole blood [80]. In their approach, they separated the sensing platform from the blood by use of a separate microfluidic purification chip. This chip has been functionalized with antibodies complementary to the proteins of input before the introduction of blood. The blood is inputted into this chip, allowed to settle to capture the relevant proteins out of solution, then is washed thoroughly to rinse out all the rest of the non-specific entities in the blood. The photoliable bonds connecting the proteins to be detected are then cleaved with UV irradiation, and the free proteins are then flown over the

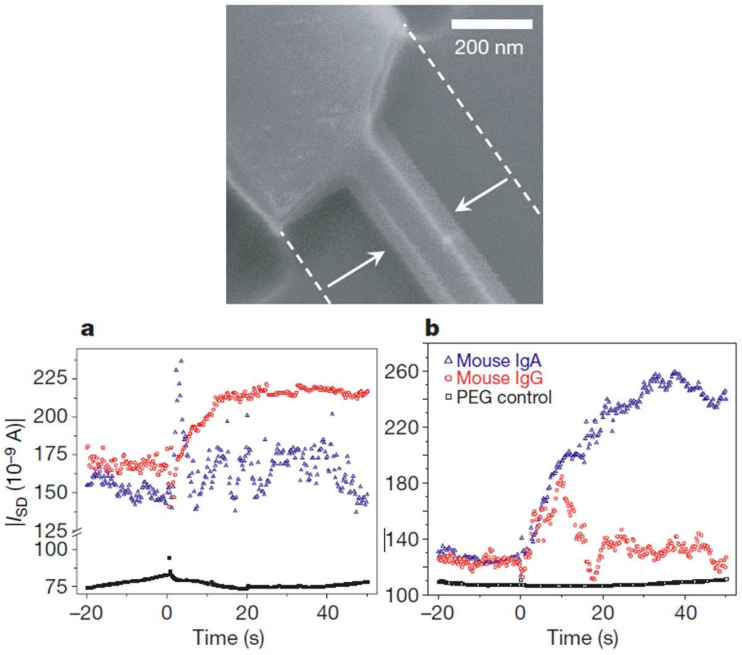

Figure 2.22: Top - Top view of a top-down CMOS compatible nanowire for biosensing. Bottom, a: Detection of 100 fM mouse-IgG (red), very little response to 100 fM mouse-IgA (blue), and no response to PEG (black) with a anti-mouse-IgG probe. b: The same three molecules introduced to a substrate functionalized with anti-mouse-IgA probe instead. From [79].

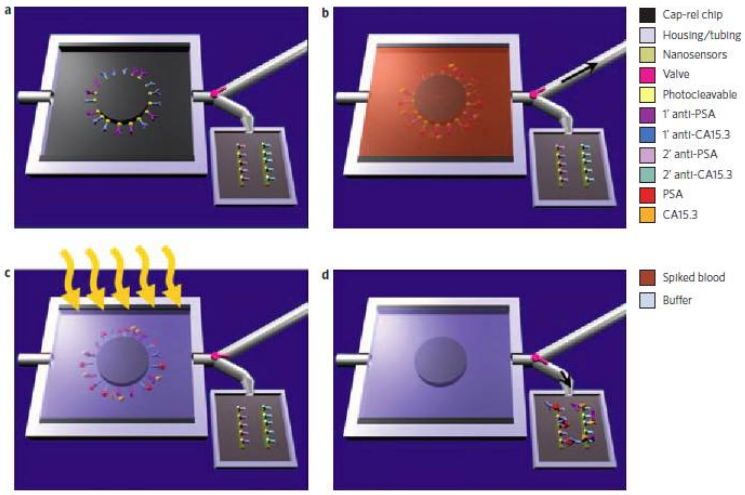

Figure 2.23: a - The two platforms without introduction of fluid. The larger platform contains antibodies to capture the proteins of interest. b - Blood containing the proteins of interest is introduced to the microfluidic purification chip, allowing the proteins to bind to their antibodies. c - After the proteins have bound, a low ionic strength buffer is used to wash, and UV light is introduced to cleave the proteins from the surface. d - The resultant solution, containing the relevant proteins are then flown over the nanowire FET sensors. From [80].

sensor chip in a low ionic concentration buffer suitable for sensing. This process is illustrated in Figure 2.23. Using this methodology, they were able to introduce blood containing both of the proteins they detected, prostate specific antigen (PSA) and carbohydrate antigen 15.3 (CA15.3) simultaneously, to devices functionalized with anti-PSA (Figure 2.24a), anti-CA15.3(Figure 2.24b). No cross talk between devices was seen, and the unspiked blood samples showed no response. Detection limits were down to 2.0 ng/mL for PSA, and 15 U/mL for CA15.3. This was the first and, to this date, only demonstration of using nanowire FET biosensors for detection of relevant proteins from bodily fluid.

Van der Berg's group at the University of Twente in the Netherlands published a very thorough work demonstrated the pH characterization of high-k dielectric Al_2O_3 devices in 2011 [81]. They described a very detailed site binding model which explained the relations between the bulk pH of the solution, the local pH experienced at the surface, and the surface potential response on their nanowire devices. Their devices were fabricated with a

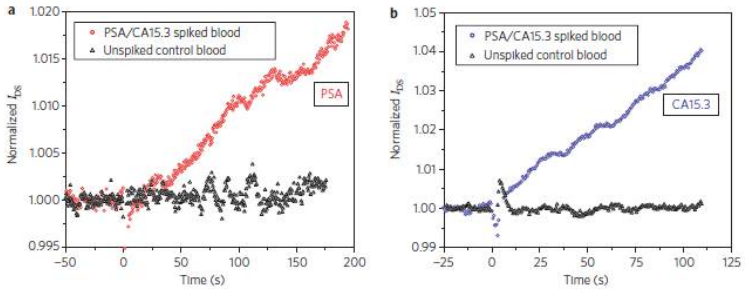

Figure 2.24: a - Introduction of 2.5 ng/mL PSA and 30 U/mL CA15.3 spiked blood and unspiked blood to sensor functionalized with anti-PSA. b The same blood samples introduced to a sensor functionalized with anti-CA15.3. From [80].

top-down approach similar to Reed's with e-beam lithography formation of the nanowires, but used an ALD aluminum oxide layer (20 nm thick) as the gate dielectric. The model described was very similar to the that first demonstrated by Bergveld's group in 1996 [49], and indeed originated from the same University. They compared their aluminum oxide devices to comparable traditional silicon dioxide devices, and showed improved sensitivity (57.8 mV/pH for Al_2O_3 vs. 45 mV/pH for SiO_2). They were able to use their model to also back out important factors such as buffer capacity and differential capacitance, which were discussed in Section 2.4.4.

Much other work has been published in the field, making it difficult to cover all important work in detail. Briefly, work utilizing CMOS compatible fabrication technique nanowires was shown to be selective [82] and sensitive of DNA hybridization down to 10 fM of concentration (for a hybridization time of 60 minutes). The method of surface functionalization and the probe used for detection play an important role, and recently organophosphonate based functionalization of PNA was used for the detection of DNA using top-down fabricated nanowire devices [83].

Besides the one-dimensional silicon structure, biomolecule detection has also been demonstrated using silicon-on-insulator (SOI) structures. There have also been reports of creating larger scale silicon-on-insulator (SOI) devices [84–86]. For example the adsorption of multilayers were detected by monitoring the conductance of SOI resistor structures [87]. SOI field-effect structures have also been incorporated with etched microfluidic channels for micro total analysis systems as an effort to demonstrate the integration capa-

bility on a common platform [88]. Recently such devices were demonstrated to detect the binding of biotin/streptavidin down to pM concentrations [89], approaching that demonstrated with silicon nanowires.

In summary, a plethora of work has shown detection of various molecules and processes, including DNA [39, 45, 76, 90–92], miRNA [93], PNA [94], cancer biomarkers [77, 79, 95–97], viruses [75], neuronal signals [98], and cell response to various stimuli [99, 100]. In addition, a host of parameters have been varied and examined including top down [79, 92, 96, 97, 100–104] or bottoms up fabrication [45, 74, 75, 77, 95, 98], AC [39, 45, 74–77, 98] versus DC [79, 91–93, 96, 97, 100–102, 104] measurement schemes, use of a fluid gate [91,101,102,105,106] or lack thereof [39,45,74–77,79,96,98,100,104,107], use of a backgate [79, 89, 92, 100–102, 104, 105, 107, 108], the operation of devices in accumulation [45, 74, 75, 77, 79, 98, 100, 106, 107] or inversion [104] mode, etc. Focused efforts have been made to determine the effect of the ionic strength of the buffer [91, 107], the effect of charge distance from the surface [92], the effect of biasing voltages [105, 106], and the effect of device width [104].

2.4.7 Theoretical Considerations

The high sensitivity achieved with such one-dimensional sensors is usually attributed to improved electrostatics owing to the high surface to volume ratio of the sensors. Also, such nanowire sensors have the potential to act as an electronic hose, in which depletion of only a segment of the wire will result in a dramatic decrease of total current through the wire.

Experimental demonstration of the capability of such one-dimensional sensors was the first step towards realizing ultra-sensitive real-time, label free sensors which could be multiplexed and densely integrated to yield a cost effective bio-molecule monitoring platform. However, an adequate theoretical framework to explain these results has been lacking, hindering the further development and optimization for the wide range applications of this technology.

Nair and Alam previously tackled this problem of providing device design guidelines by considering the electrostatics of the system [109]. They have also explained the increased sensitivity observed with the nano-biosensors by

considering the diffusion-capture kinetics of the target molecules [110], which showed geometry dependent properties - diffusion of the target molecules to the device is enhanced as the dimensionality of the active area decreases. In a more recent work [111] they combine these two approaches to provide a coherent theoretical framework and explain some of the puzzling properties seen with the nano-biosensors. Importantly, the model accurately predicts the logarithmic dependence of device response on the target molecule concentration. The simplified analytical solutions provide important insight into the steady state and transient sensor response dependence on parameters such as analyte concentration, buffer ionic concentration, and pH. The model can easily be modified and expanded for the modeling and optimization of more complex situations, which will allow the accurate prediction of sensor performance and further optimization of nano-biosensors for novel applications.

Specifically, the dimensionality of the system plays an important role in the dynamic response of the sensor and for lower dimensional systems the diffusion-capture considerations stipulate a higher density of molecules on the surface for transient conditions [111]:

$$N(t) \sim k\rho_0 t^{(1/D_F)} \tag{2.17}$$

where N is the time dependent density of the conjugated molecules (bound targets) on the surface, k is a geometry dependent constant, ρ_0 is the target concentration in the solution and D_F is the fractal dimensionality of the system.

The response may not correspond to the expected net charge of the analyte if the molecule binds in a directed way, as is shown with the electrostatic binding of BSA on the oxide surface [112]. The positive residues end up pointing in the negatively charged oxides surface, hence an increase in the surface potential is registered instead of the decrease that might be expected considering the net charge of the molecule.

One potential limitation of field-effect sensors is the electrolyte that can be used. Due to the fact that the fundamental mechanism of detection involves surface charge sensing, the counter ions in the solution will screen the surface and make the device less sensitive. It is not possible to sense charge separated from the surface by approximately the Debye length, which is given by [111]:

$$\kappa^{-1} = \sqrt{\frac{\epsilon_0 \epsilon_r kT}{2q^2 I_0 N_A}} \tag{2.18}$$

where ϵ is the permittivity of free space, ϵ_r is the relative dielectric constant of the buffer, k is the Boltzmann's constant, T is the temperature, q is the elementary charge, I_0 is the ionic concentration, and N_A is Avagadro's constant. Thus, the sensitivity of the devices degrade with the increased ionic strength of the buffer. Screening limits the detectable distance of the analyte from the sensor surface [92] because the amount of charge mirrored in the active area will decrease with increasing separation. One proposal to use the counter-ions to the advantage of sensing is to design the system to utilize the redistribution in the counter ion concentration [113, 114] to sense the hybridization of DNA.

Some questions still exist as to how several of the biosensing results, specifically for the very low concentrations of molecules down to fM concentrations, can exhibit such sensitive detection results in such small time scales, on the order of a few minutes [115]. Simulation work has been completed to examine the diffusion kinetics of capture based detection, with the general conclusion that without enhanced transport of the molecules to the surface, hours or even days should typically be needed for such sensitive detection. This is an area still not clear in the literature that needs further exploration.

2.5 What is Needed?

From a clinical cancer based perspective, there is a great need for a device that can:

- Screen for a wide variety of relevant biomolecules, including certain genes (DNA sequences), RNA sequences, microRNA sequences, cancer biomarkers and other proteins relevant to cancer pathways, simultaneously
- Yield results, including data analysis, in a week or less
- Cost significantly less than $1000 per test

If such a device were to be created, it would find immediate use in cancer clinics across the United States and Europe for personalized medicine and for the evaluation of the efficacy of cancer treatments. For the FET biosensor technology to reach such a goal, several challenges need to be overcome, including but not limited to:

- Extending device lifetimes in fluid. This is one parameter that is often glossed over in the literature, but it is well known in the field to be a significant problem.
- Increase the repeatability and reliability of devices. Results are typically from only a few devices and sometimes are not fully representative of most devices fabricated. Device to device variation can be very large, which makes scaling very difficult.
- Reasonable methods for converting body fluids in high ionic strength environments with a wide variety of different biological species into cleaner buffer solutions with the analytes to be sensed.
- Reduction of false positives and negatives from all of the non-specific entities present in bodily fluids.
- Demonstration of reasonable dynamic ranges for concentrations for the analytes that are known to be clinically relevant for cancer.

The rest of this dissertation will focus on steps towards these goals.

CHAPTER 3

FABRICATION AND ELECTRICAL TESTING OF SIO_2 DEVICES

3.1 Introduction

This chapter will describe the baseline fabrication process used for the rest of the dissertation and will discuss various electrical setups used for measuring device characteristics.

The first few iterations of the devices used silicon dioxide as the gate dielectric. SiO_2 is the most commonly used gate dielectric in silicon FETs, due to ease of formation and great dielectric properties. Schematics demonstrating the important final cross sections are shown in Figures 3.1 and 3.2 for three nanowire devices. Section 3.2 will describe the fabrication process in detail. Processes in subsequent chapters will build off this baseline process with various improvements and optimizations.

3.2 SiO_2 Device Fabrication

The baseline process included the following steps, which will be described in more detail later in this section:

- 8" bonded SOI wafers (SOITECH) doped p-type at $10^{15}/cm^2$ with BOX thickness of 145 nm and superficial silicon thickness of 55 nm were laser cut into 4 wafers by Ultrasil Corp.
- Wafers were oxidized for 11 minutes at 1000 °C to grow 30 nm of oxide and were placed into buffered oxide etch (BOE) to thin down the top silicon to around 350 Å.
- A double layer resist strategy was used with 100 nm/95 nm of LOR 1A/PMMA to define the smaller patterns (the 50 nm nanowires and

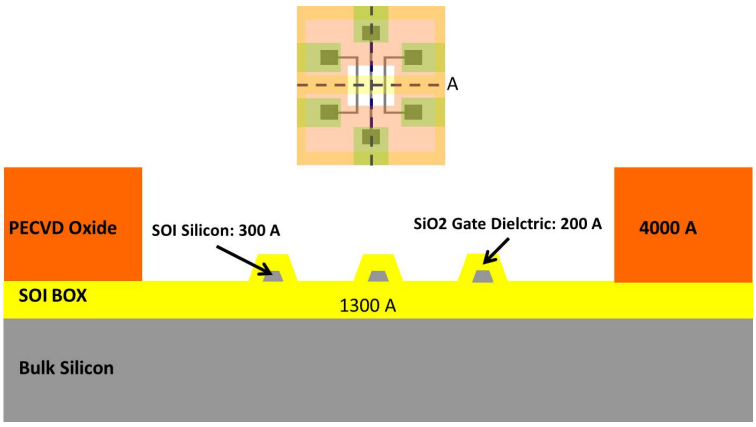

Figure 3.1: Final cross sections through a horizontal cut through three nanowire devices.

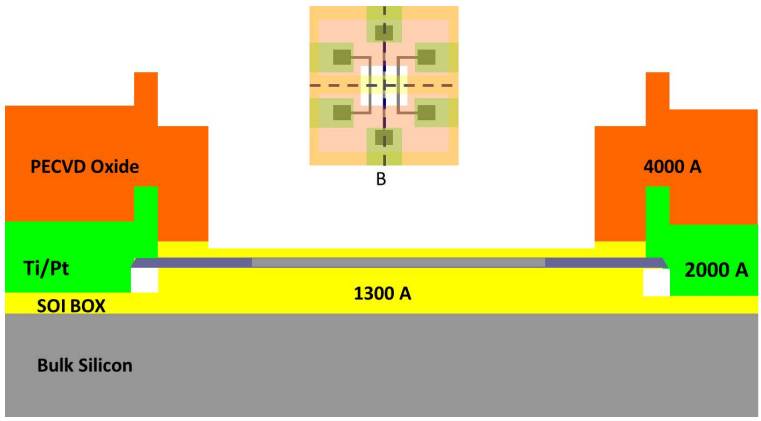

Figure 3.2: Final cross sections through a vertical cut through three nanowire devices showing the channel, and source and drain electrodes.

connections) using electron beam lithography, with dosages varying from 1700 μC/cm^2 to 2000 μC/cm^2 for the different designed patterns. The wafers were then placed into 60% CD-26 developed diluted with water for 1 minute to create an underetch profile to assist liftoff. 250 Å of chrome was then evaporated, followed by immersion in Remover PG for 1 hour at 70 °C for liftoff.

- Optical lithography was performed with a double layer resist of LOR 3A/Shipley 1805 to define larger silicon features, such as the nanoplates and mesas to connect to metal interconnects. 250 Å of chrome was then evaporated, followed by immersion in Remover PG for 1 hour at 70 °C for liftoff to complete the full chrome hard mask used to define the active silicon.

- The wafer was placed into a brief BOE dip to remove native oxide, then was placed into 60 °C TMAH for 1 min, 20 seconds to transfer the pattern from the chrome hard mask to the active silicon layer.

- The chrome hard mask was then etched off using CR-14, a wet chrome etchant. Visual and AFM characterization was performed to determine the yield and thickness of the devices.

- Wafers were then dry oxidized for 6 minutes at 1000 °C to form an implant slow down layer.

- Optical lithography was then employed to form a photoresist mask for doping implantation of the source/drain regions of the devices. Wafers were doped with boron at 10 KeV at a dose of 10^14 cm^{-2} and a tilt of 7°.

- At this point, the gate dielectric was formed. The wafers were dry oxidized for 3 minutes at 1000 °C to form a gate oxide of around 150 Å. This also served as a dopant activation step.

- Wafers were then subjected to a forming gas anneal to remove interfacial traps at 500 °C for 10 minutes in 5% H2 in nitrogen.

- Next, vias were formed in the silicon mesas with optical lithography and subsequent BOE etch to make solid, crack-free connection between

metal interconnects and the silicon layers. AFM was performed over these regions to determine the silicon thickness (around 220 Å) and the gate dielectric thickness (around 150 Å).

- 250 Å of titanium followed by 750 Å of platinum were then evaporated and lifted off over a double layer resist of LOR 3A/Shipley 1805 to pattern the metal traces.

- A rapid thermal anneal was then performed at 550 °C for 2 minutes in a N2 environment. This is a key step to ensure that the devices have good contact resistance, which translates into healthy source-drain currents dominated by the resistance of the channel instead of the resistance of the source-drain contacts.

- After electrical testing to determine the yield of the devices at this step, 4500 Å of PECVD silicon nitride was deposited using a mixed frequency recipe for use as an insulation layer.

- Holes were then opened over the pads of the device using a Freon RIE etch, and a thick (2000 Å of titanium followed by 8000 Å of gold) metal layer was deposited and lifted off using the same mask to form the thick gold pads for wire bonding

- Optical lithography was then used to open holes directly over the pads on the external part of the chips. The silicon nitride was etched using a dry CF_4 RIE etch (90 W, 36 mtorr, 15 minutes). A thick pad layer was then evaporated and lifted off for wire bonding (2000 Å/8000 Å of Ti/Au).

- Wafers were then diced into 4 mm x 9.5 mm pieces.

- Next, etchback windows were opened directly over the active regions of the devices using optical lithography. Devices were etched on a die by die basis (CF_4 RIE, 90 W, 36 mtorr, time varied) with constant visual inspection to ensure that the etch stopped on the top oxide gate dielectric.

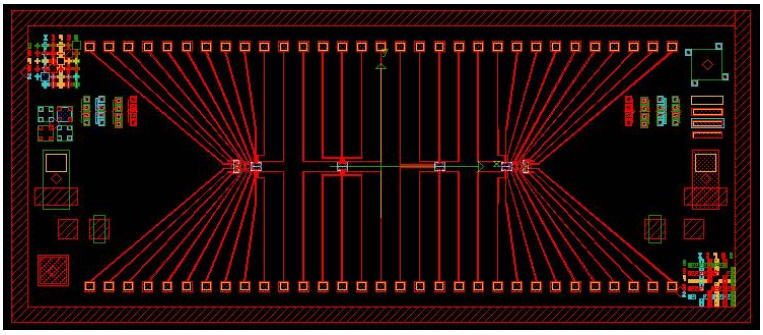

Figure 3.3: Die mask file for the silicon dioxide devices

3.2.1 Mask Design

The die level mask is shown in Figure 3.3. Dies were 4 mm x 9.5 mm in size, and contain four modules of nanowires with five devices per module as well as eight nanoplate devices. SEM images of the different designs are shown in Figure 3.4. Designs included:

- Five 50 nm wide nanowires separated by 200 nm (upper left).
- Five 50 nm wide nanowires, separated by 200 nm, 400 nm, 800 nm, and 2 μm (upper right).
- Four devices, with widths of 50 nm, 200 nm, 400 nm, and 1 μm, separated by 200 nm, 400 nm, and 1 μm (lower left).
- Nanoplate devices with widths of 2 μm, separated by microns (lower right).

3.2.2 Nanowire Definition

The first and most important step of the fabrication process was the formation of the active silicon layer that serves as the conduction channel for the device. Most specifically, for the devices with widths smaller than the lithographical limit, electron beam lithography was required for definition. However, because a light field mask is required to define the devices, we had two options: either the use of a negative e-beam resist for wire definition, or the development of a metal liftoff process that could serve as a hard mask

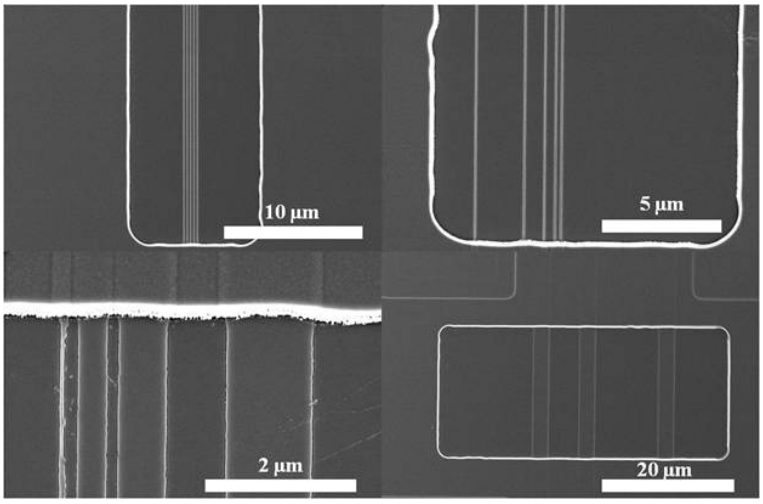

Figure 3.4: SEM images of the different available devices with different widths.

for etching of the silicon to form the wires. We chose to go with the latter process, due to the difficulty and expense of procuring a negative e-beam resist. A schematic showing the strategy for formation of the wires is shown in Figure 3.5. Initial efforts to perform the liftoff with a single layer resist (positive tone PMMA), however, proved to be unfruitful, most likely due to chrome residue that interfered with the liftoff procedure (Figure 3.6). A double layer approach was chosen to solve this problem, using a thin liftoff resist (LOR 1A, 300 nm) followed by the standard positive e-beam resist layer. After optimization of the exposure energy to form the 50 nm lines that we wanted, we were able to form the chrome hard mask for wire definition (Figure 3.7).

After the nanowire chrome hard mask was formed, a lithography step was performed to define the additional chrome hard mask to form larger silicon features (silicon mesas) that are too large to be formed by e-beam lithography. These include the silicon plate structures and larger mesas that interconnect to the edges of the wires formed by e-beam. We used a double-layer resist strategy (LOR3A/Shipley 1805) for ease of liftoff, followed by 250 Å of chrome to form the full hard mask.

After the hard mask was fully formed, including both nanoscale and microscale structures, the pattern needed to be transferred from the hard chrome mask to the underlying silicon. Previous iterations employed a dry

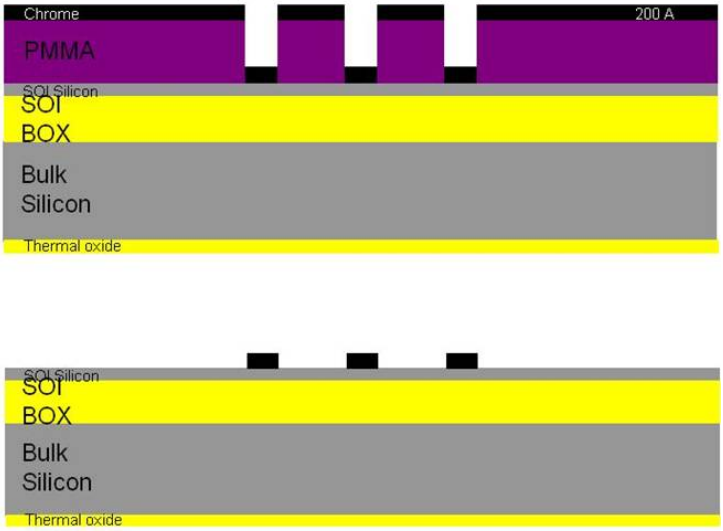

Figure 3.5: Schematic showing the method for formation of the nanowires.

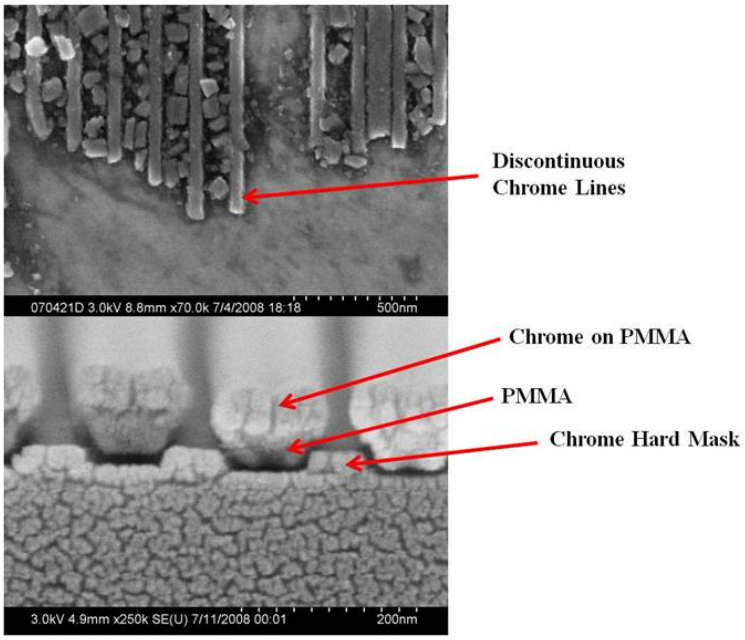

Figure 3.6: Top and cross sectional SEM images showing issues with defining the Cr hard mask for the nanowires.

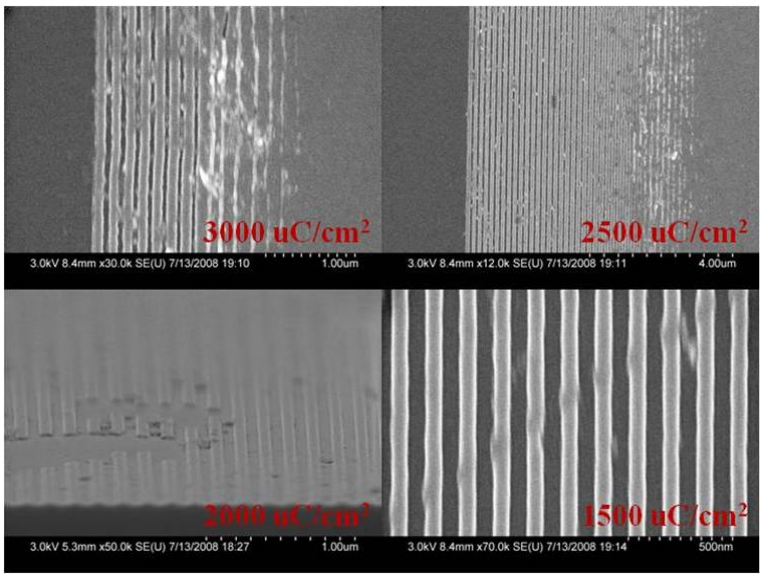

Figure 3.7: Optimization of e-beam dosage for the formation of the nanowires.

reactive ion etch at this step to form the silicon structures, but we observed electrical damage which caused device degradation, consistent with literature [116]. We instead opted to use a TMAH etch at elevated temperatures, which etches preferentially along the 111 planes, resulting in a trapezoidal shaped device as will be seen in the cross sections. The etching time was carefully optimized to ensure that minimal undercut of the chrome mask occured to preserve the expected widths for the devices. SEM top view images and cross sections of the wires and plates are shown in Figure 3.8. The smallest nanowire width was typically around 50 nm, while plates were 2 μm.

3.2.3 Ion Implantation for Doping

Ion implantation is a commonly used process for doping of semiconductors where ions of a material are accelerated in an electric field and impacted into the surface of the semiconductor. It was chosen for ease of use and repeatability. Important parameters to optimize include dose energy, tilt, and the thickness of a slowdown layer over the silicon to be doped. TSUPREM, a semiconductor manufacturing software available from NanoHUB from Purdue, was used to simulate appropriate conditions for doping. We found that over $10^{19}/\text{cm}^2$ doping density could be achieved with 10 keV with a SiO_2

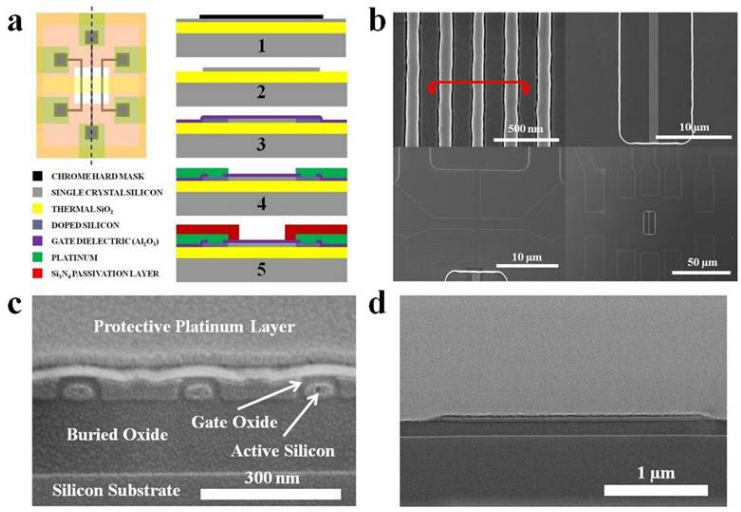

Figure 3.8: Schematic illustrating the fabrication process, SEM top views (b), and SEM cross sections (c,d) of the devices.

slowdown layer 75 Å thick. The results from the simulation for these conditions showing the doping density versus distance from the surface in μms is shown in Figure 3.9. The presence and thickness of the slowdown layer is a very important parameter because without such a layer, ions typically would penetrate all the way through the extremely thin silicon layer, and implant into the buried oxide. Achieving doping levels in the source/drain regions of the sensors higher than 10^{19} was extremely important to achieve as low series and contact resistances as possible so that device performance was dominated by the resistance of the undoped silicon channel.

3.2.4 Formation of Vias

In previous iterations of the devices, the gate oxide over the source-drain mesas was fully etched away prior to the deposition of the metal source-drain leads that connected the source/drain mesas to exterior pads on the chip for probing. A wet dilute buffered oxide etch was used for this oxide removal. After testing of devices in fluid, however, it became clear that this led to undercutting issues of underlying buried oxide used for isolation of the devices from the back substrate. To resolve this issue, we introduced another mask for opening of via holes over the source and drain of the silicon mesas as shown in Figure 3.10. This also allowed us to acquire AFM images

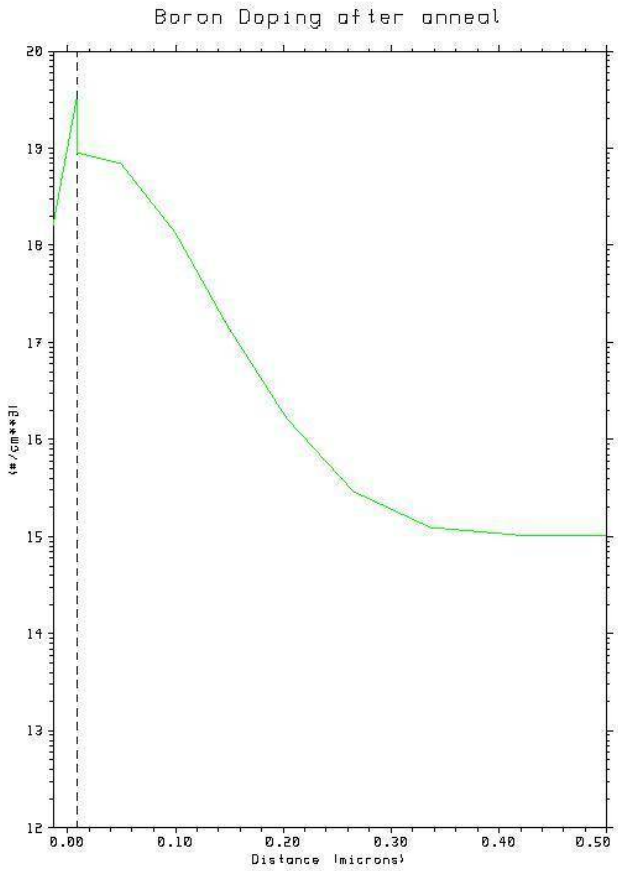

Figure 3.9: Doping simulation showing the final concentration of dopants versus distance from the surface using TSUPREM from nanoHUB at Purdue.

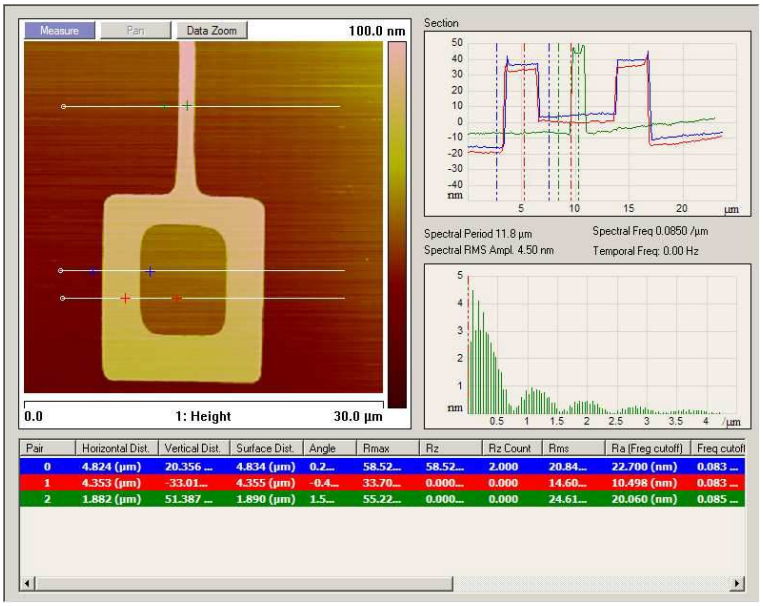

Figure 3.10: AFM images and software allowing for the extraction of important thicknesses after the formation and etching of vias.

of the device at the step, yielding important information about the exact thicknesses of the active silicon layer and the gate dielectric. The silicon was found to be approximately 220 Å thick, and the silicon dioxide to be 150 Å.

3.2.5 Source/Drain Metal Contacts

Initially, gold was chosen for source and drain metal leads due to high selectivity for various etches, and because the thick pads for wire bonding are typically gold due to its malleable nature. However, we observed debilitating adhesion issues of the PECVD nitride passivation layer to gold metal traces, as can be seen from the cross sectional SEM in Figure 3.11. Approximately 250/750 Å of Ti/Pt was deposited instead, which resolved the adhesion issues.

A critical step after the patterning of the metal traces was the formation of an ohmic contact between the metal and the underlying doped silicon source/drain. The overall resistance for a measured device is a sum of all the series resistances:

$$R_{total} = R_{lead} + R_{C(drain)} + R_{device} + R_{C(source)} + R_{lead} \tag{3.1}$$

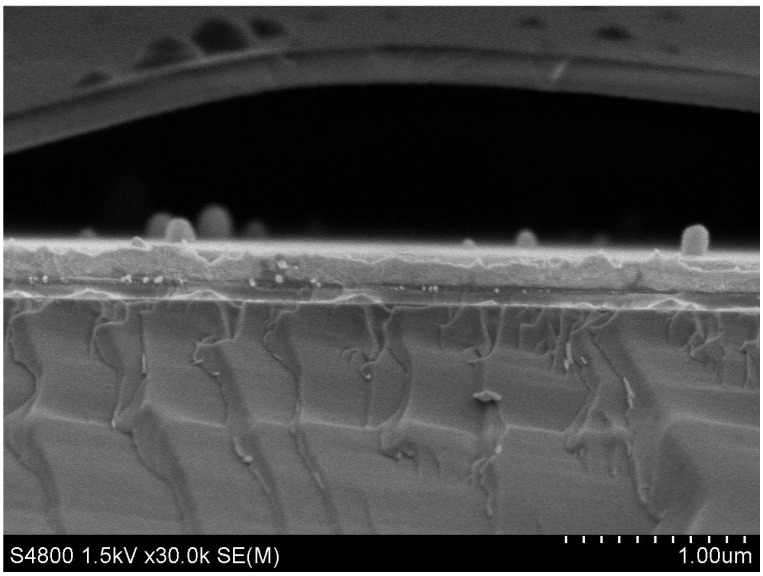

Figure 3.11: Cross sectional SEM image showing lack of adhesion between the passivation PECVD oxynitride and a Ti/Au metal layer.

If either of the R_C terms is on the same order of magnitude as R_{device}, then the overall resistance will be dominated by the contact instead of the carriers in the device. The contact resistance is of course independent of any events in fluid, and so device signal-to-noise ratio will suffer significantlly if the contact resistance is not lowered [117]. It is of utmost performance, then, to: a - ensure that the metal-semiconductor junction is ohmic instead of rectifying and b - to make sure that the resistance of this junction is as low as possible, preferably at least two orders of magnitude lower than the device resistance.

The contact resistance for a metal contact on a semiconductor is a strong function of one of two characteristics: the work function difference between the metal and semiconductor or the surface properties of the semiconductor. If a large density of surface states is present at the semiconductor surface, then the Fermi level is pinned by the surface states and the barrier height is determined by the surface properties of the semiconductor. In the abscence of these surface states, the barrier height is determined mainly by the metal-semiconductor work function difference. Silicon has behavior in between these two extremes, and so for this work the specific contact resistance is a strong function of both the work function difference and the doping concentration of the silicon at the surface.

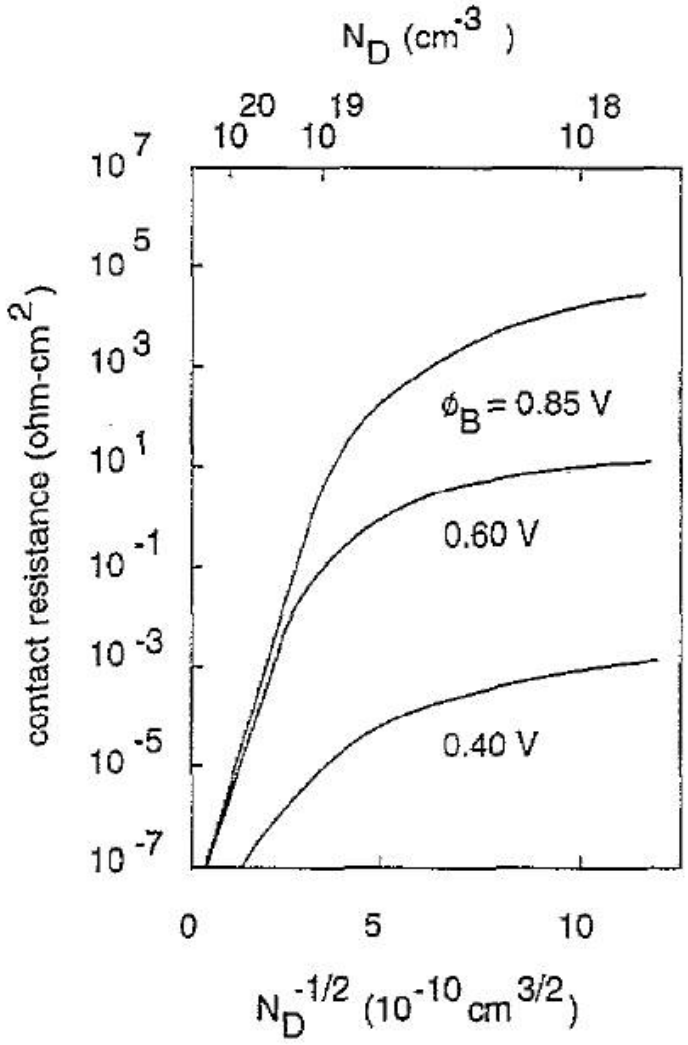

Figure 3.12: Contact resistance as a function of doping and work function of silicon, from [118].

The Schottky barrier height for Ti-Silicon is around 0.6 eV [118]. This value is quite low, and so the contact resistance is mostly dominated by the doping level of the silicon. Figures 3.12 and 3.13 illustrate the dependence of contact resistance on doping of silicon and work function. The doping levels here are concentration of activated dopants, which is the reason for the high temperature oxidation step after doping (in addition to forming the gate oxide). The solubility of dopants in silicon increases with temperature, and typically wafers are brought to above 1000 °C for this reason.

Titanium silicide needs to be formed at the titanium/silicon junction to convert the metal-semiconductor junction from rectifying to ohmic. Non-

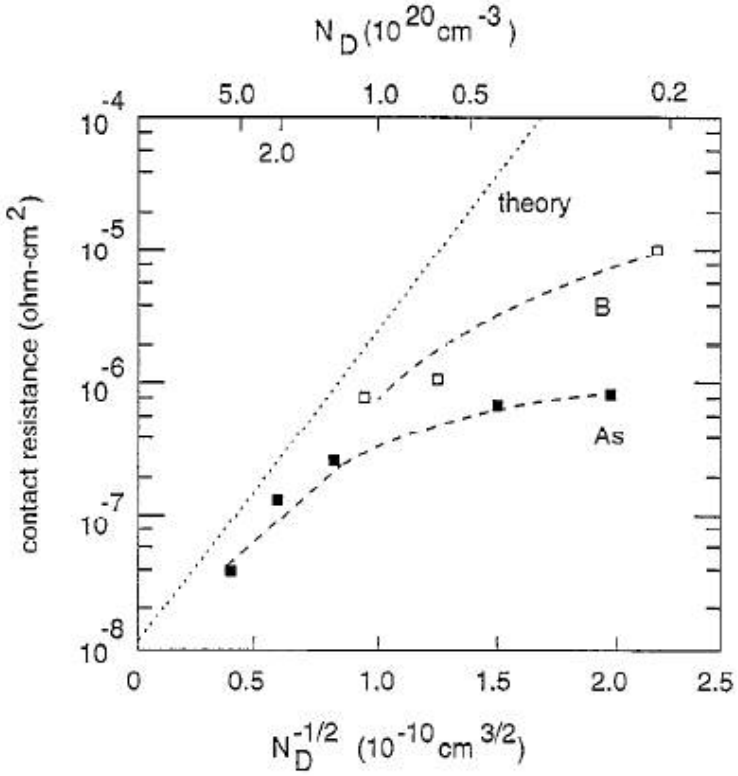

Figure 3.13: Contact resistance as a function of doping in silicon, from [118].

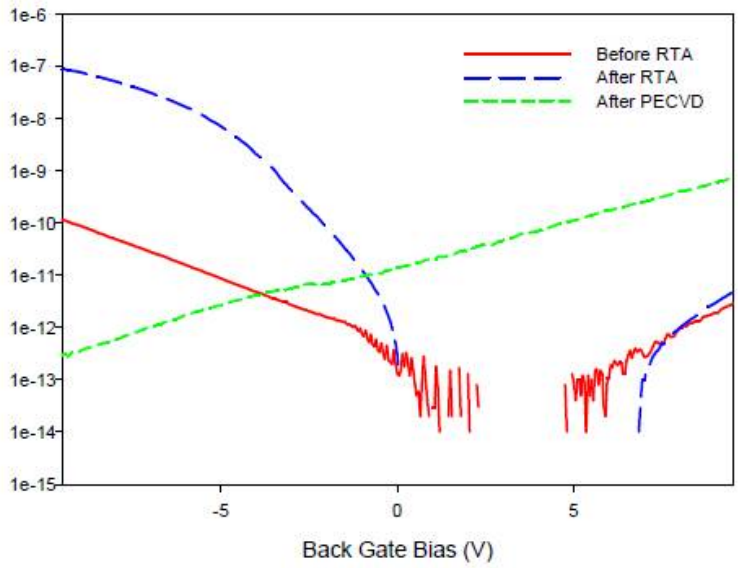

Figure 3.14: Drain current versus backgate voltage for a nanoplate device before a rapid thermal anneal for ohmic contact formation, after the RTA, and after the PECVD passivation layer has been deposited over the devices.

ohmic behavior can kill device behavior, as can be seen in Figure 3.14, which shows transfer characteristics for a nanoplate device before and after the formation of an ohmic contact. In the microelectronics industry, silicides are commonly formed via increasing temperature, allowing diffusion of the silicon into the metal. However, for thin films it can be a challenging task to form the silicide without fully consuming the silicon. For our devices, the silicidation had to be rapidly controlled with a rapid thermal anneal for a very specific amount of time. To determine this sensitive recipe, a wafer was sacrificed and diced into many small pieces after the metal deposition step. These pieces were used to optimize the recipe for the lowest resulting contact resistance, and this recipe was used for the real wafers.

Each die contained a test structure used to measure contact resistance, which is shown in Figure 3.15. The bar shown in the figure is fully doped, so that the total resistance is given by Equation 3.1, where R_{device} is a simple resistance of the doped bar. Since the spacing from A to B, B to C, and C to D are equal, the resistance values for A to B, A to C, and A to D can be plotted on the same plot. When a linear fit is performed to this data, the intercept at Unit Resistor = 0 yields a value that is twice the contact resistance. Using this technique, the recipe for the rapid thermal anneal was

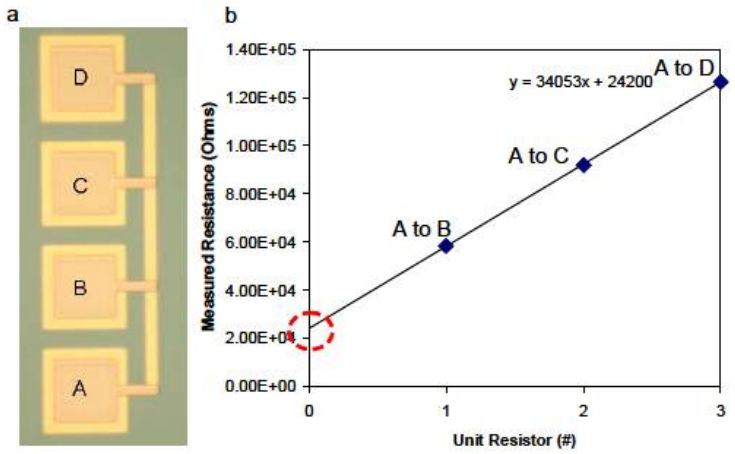

Figure 3.15: a - The test structure used to extract contact resistance. b - A sample plot showing how contact resistance could be extracted.

determined. The spread across the machine used was 5-10 °C across a 4" wafer, a disparity enough to increase the contact resistance by one order of magnitude. Contact resistance as a function of anneal temperature is shown in Figure 3.16. Though the optimal temperature was found to be 570 °C, 550 °C was chosen due to an observed increase in flexibility around that temperature range.

3.2.6 Etchback of the Passivation Layer

The passivation layer used was a 4500 Å thick PECVD oxynitride that was found to have good adhesion to the surface and low leakage in fluid. Leakage in fluid was characterized by patterning metal leads on an oxidized substrate, deposition of the oxynitride, and measurement of leakage paths in fluid. After deposition of the oxynitride, holes directly over the devices needed to be etched in order to expose the devices to the fluidic environment for sensing.

Wafers were patterned with the photoresist mask for etching back the windows over devices, then were diced into 4x9.5 mm pieces. Each of these pieces with the photoresist mask still intact were invidually used during the etchback process. Initially, a wet process with buffered oxide etch (BOE) was preferred due to the ease of use and lack of damage to the devices. However, this resulted in large leakage currents in fluidic environments. The cause

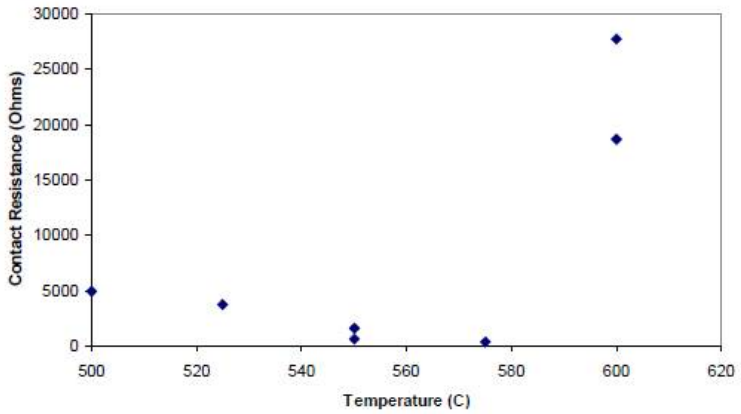

Figure 3.16: Dependence on extracted contact resistance versus RTA temperature.

for this is illustrated in Figure 3.17. Parts a and b show images of a device which have not yet been etched and the regions where the PECVD film growth fronts meet at. Figure 3.17c shows a device which has been etched to thin down the dielectric layer over the active area. Premature etching of the dielectric at the device edges indicates that the echant had reached those locations well before the intended time. Further study of the prematurely etched region revealed that the etchant was attacking the buried film from an epicenter equidistant from the etched edges. These observations indicate that the wet etchant had traveled through the voids to cause premature etching of the buried oxide layer. These voids are seen by the etchant only after some of the top layer on the dielectric has been etched as indicated by the amount of material removed at the device edges.

This problem was resolved with the use of a dry etch for releasing the devices. By switching to a directional etch (Dry CF_4 RIE etch), the problem of an isotropic etchant that could seep through these cracks was avoided. Resulting cross sections using this method were shown in Figures 3.8c and d. Dies were etched back on a die by die basis, with careful monitoring of the etch time to ensure that the gate dielectric was not overetched. By comparing the color of the buried oxide window to a known control sample, we were able to etch the passivation layer with less than 20 Å overetch of the gate dielectric, as was confirmed by cross-sectional SEM.

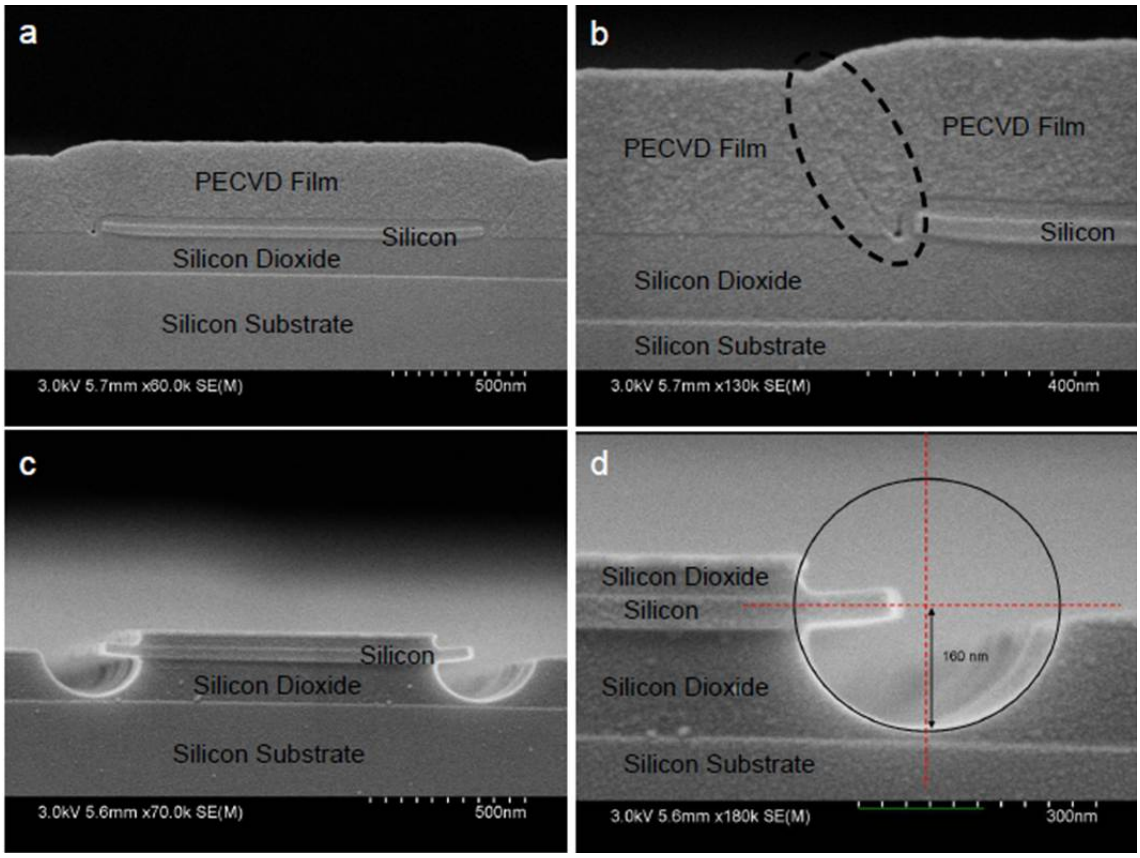

Figure 3.17: SEM micrographs of devices before and after the wet etch. a - Before the etch, b - Magnified view showing the void caused by the PECVD film growth fronts meeting, c - After wet etching the PECVD layer, d - Close-up showing the origin of the isotropic wet etch corresponding to the location of the void shown in part b.

3.3 Electrical Testing in Fluid

This section will briefly describe the method for electrical testing of devices in fluid. This method was also used for the aluminum oxide devices described in Chapter 5. Goals for the electrical setup include:

- Ability to make electrical contact to multiple devices to obtain device characteristics
- Enable convenient switching between devices
- Ability to introduce fluid to the devices without interfering with electrical characteristics
- Ability to change fluids over the devices with little residue of previous fluids

3.3.1 Electrical Circuit

All of the presented device structures are p+/p-/p+ devices which need to be operated in accumulation mode (if the conduction channel was inverted, creating a p+/n+/p+ structure, the back-to-back p-n junctions would prevent electron conduction). Conduction, then, was dominated by hole conduction with negative applied substrate biases or fluidgate biases. The schematic used for testing the devices is shown in Figure 3.18. A potential is applied between source and drain terminals of the device while the drain-source current is monitored. In addition, a bias is applied to the substrate, dubbed V_{BG}. An on-chip platinum fluid gate that was patterned during the formation of the metal interconnects could be used as an extra fluidic gate when testing the device in fluidic environments.

3.3.2 Dry Backgate Characteristics

Initially, contact was made to the devices without fluid. Tungsten probe needles made contact to the pads on the outside of the chip with micromanipulators. A low resistance metal chuck made contact to the backside of the die for application of backgate voltages. Typical dry electrical characteristics for a 50 nm SiO2 silicon nanowire FET device are shown in Figure

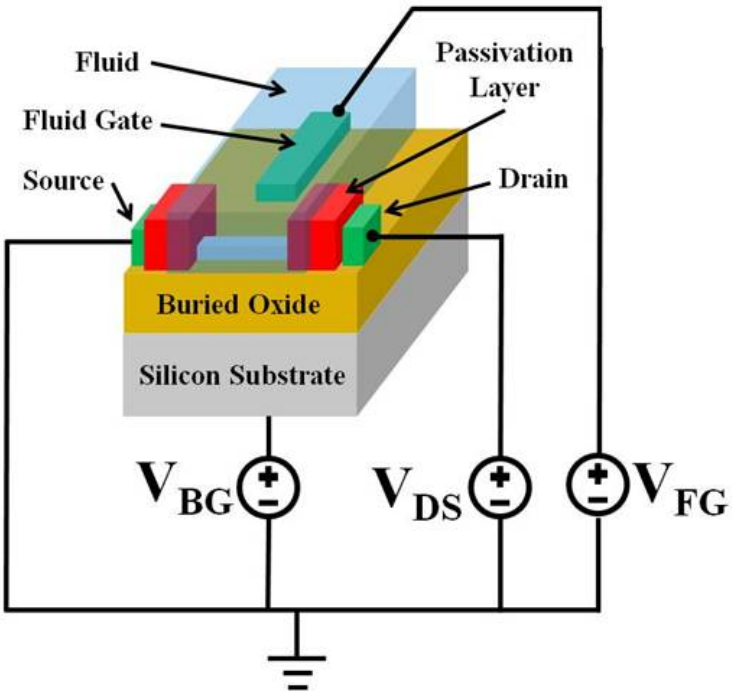

Figure 3.18: Schematic for electrical testing of the FET devices.

3.19, which plots the measured source-drain current I_{DS} versus the applied substrate bias (V_{BG}). Also measured is the gate leakage current, which is the current at the node where the substrate bias is being applied. For defective devices, this gate current could rise to of the same order of magnitude or higher than the drain source current, most likely due to point defects in the buried oxide insulation layer. The gate current, then, was a good indication of device failure and was always monitored in any experiment to ensure that the device was functioning as desired. Normal transistor behavior was observed, with saturation, subthreshold, and cutoff regions of operation. The device shown has measured contact resistance of less than 1 kΩ, and thus has a saturation current close to the maximum allowable current for the device cross sectional area (around 1 μA). Due to the low oxide capacitance because of the thickness of the buried oxide layer, very high voltages were needed to fully turn on the device.

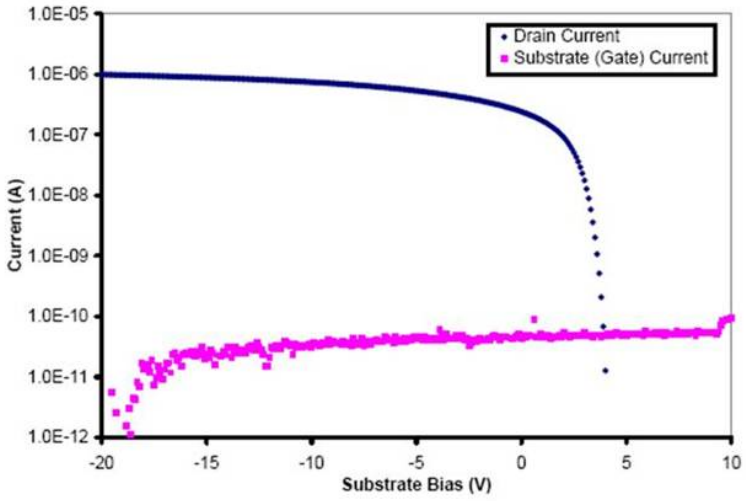

Figure 3.19: Transfer characteristics of a 50 nm silicon dioxide nanowire device (blue). Backgate leakage current for the same device (pink).

3.3.3 Electrical Connection for Testing of Multiple Devices in Fluid

The 4 mm x 9.5 mm chips were placed into ceramic packages (Global Chip Materials 28 pin lead sized brazed package) as shown in Figure 3.20. Microfluidic channels were fabricated using commonly employed SU-8 master wafers, and were then aligned to the chip using a mask aligner, and individual devices were contacted using wire bonding to the package. Teflon tubing was inserted into the ends of the channel, and the entire setup was covered with slow drying epoxy to insulate the devices and to mitigate fluid leakage issues. The entire ceramic package was then placed into a custom designed PC board connected to a computer that could individually address any of the devices that were wire bonded. Fluid was exchanged using the tubing and syringe pumps with syringes containing the various different solutions. Electrical current measurements and applied biases were controlled by a semiconductor parameter analyzer (Keithley 4200). Each device consisted of a source contact and a drain contact connected via wire bonding to a switch matrix that could choose between any of 10 different devices. Universal back gates and fluidgates were used for all devices, also connected via wire bonding to the ceramic package which was in turn connected to the semiconductor parameter analyzer. A schematic demonstrating this electrical setup for an AC measuring scheme is shown in Figure 3.21. In this scheme, the conductance

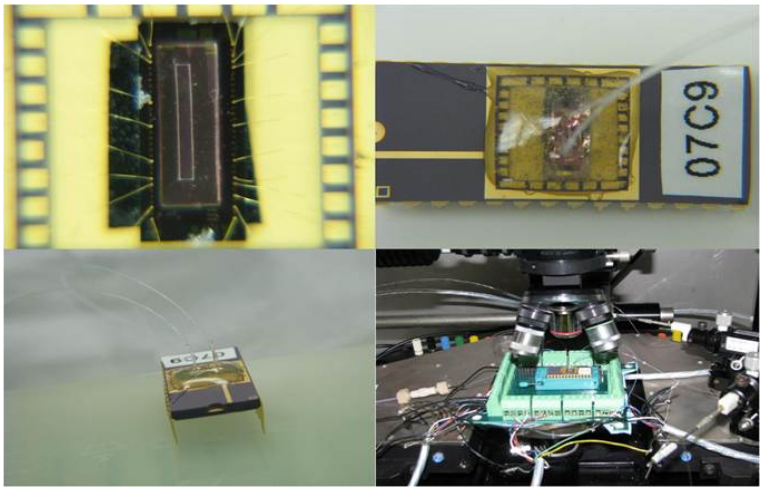

Figure 3.20: Measurement Setup. Upper left: Chip placed in a ceramic package, with a microfluidic channel and individual devices wire bonded. Upper right and lower left: Ceramic package covered in epoxy for insulation with microfluidic tubing. Lower right: Ceramic package placed into a PC board with connections to allow for the addressing of any desired device.)

of the device can be measured at a 0 V DC bias, which is convenient for fluidic measurements as was discussed in Chapter 2.

3.3.4 Transfer Characteristics in Fluid

Typical transfer characteristics for a 50 nm wide nanowire and a 2 μm wide nanoplate are shown in Figure 3.22, using the on chip platinum electrode as a fluid gate. The source-drain voltage for the devices is 0.1 V for operation in the linear regime of the FET devices. For all silicon dioxide oxide devices, if the source-drain is not specified in this dissertation, V_{DS}=0.1 V. Normal behavior is seen, with a subthreshold slope of 228 mV/decade for the plate device and 289 mV/decade for the wire. Figure 3.23 shows the current into the fluid gate for these devices. Leakage currents for the nanoplate devices were approximately two orders magnitude higher for plate devices on average, probably due to defects in the oxide in the increased area over the nanoplates. As can be seen from the graphs, the threshold voltage is around 0.5 V or so, showing minimal fixed charge in the devices. In addition the standard deviation in threshold voltage for five sweeps was typically 10 mV or less for devices regardless of the width, which is not ideal but not debilitating for

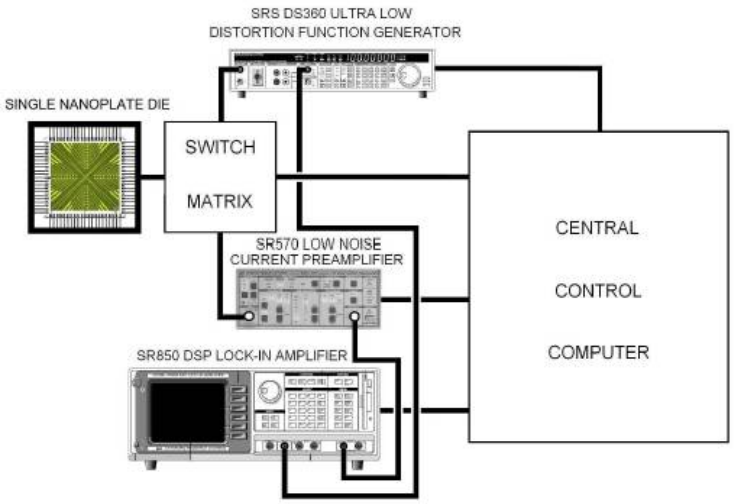

Figure 3.21: Schematic for an AC measuring scheme with a central control computer that can control a switch matrix to switch between any of the devices wire bonded on chip.

detection experiments as long as the signal is greater than 30 mV.

3.4 Conclusions

In conclusion, this chapter has demonstrated the baseline process that future fabrication iterations and chapters will be built on. Several important issues with the device fabrication were illustrated, including the definition of the nanowires using e-beam lithography and liftoff, doping concerns, contact resistance, proper insulation of the devices in fluid, and the etchback step to expose the devices to fluid. We additionally illustrated the basic electrical setup that enables use of multiple devices in a convenient, integrated fashion in fluid environments with easy fluid exchange steps. This platform will be referenced for the remainder of the dissertation.

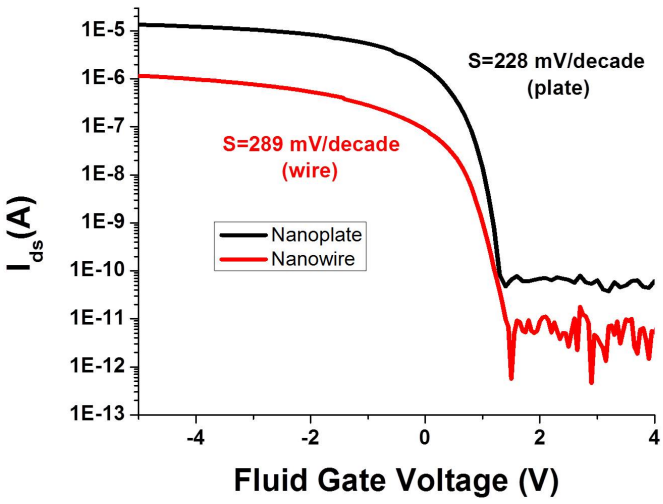

Figure 3.22: Transfer characteristics for a nanoplate device with width 2 μm and a nanowire device with width 50 nm.

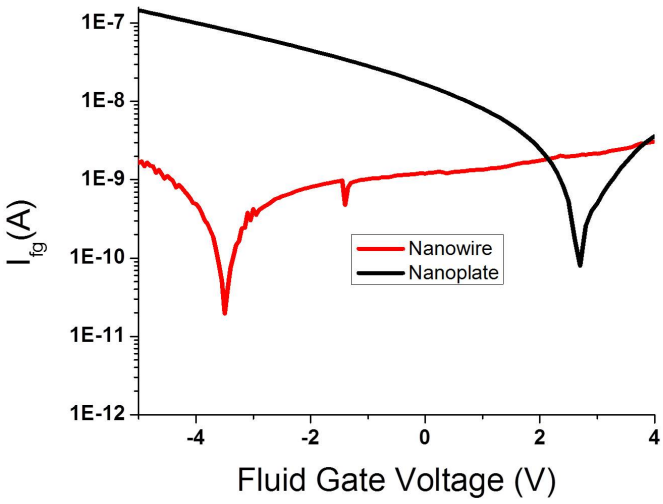

Figure 3.23: Current into the fluid gate for a nanoplate and nanowire device.

CHAPTER 4

BIOMOLECULAR DETECTION USING DEVICES WITH A SIO_2 GATE DIELECTRIC

4.1 Introduction

This chapter will discuss applications of the devices described in Chapter 3. Both nanowire and nanoplate devices were used for various applications, including the detection of pyrophosphate molecules for sensing DNA polymerase reactions on DNA surfaces, of DNA match and mismatches sequences, and of mouse-immunoglobulin antibodies. The results here show that the fabricated devices are sensitive charge sensors that can be used for a variety of applications.

4.2 Electrical Detection of Pyrophosphate from DNA Polymerase Reactions

The work demonstrated in this section was executed in collaboration with Grace Credo, Oguz Elibol, and Madoo Varma at Intel Corporation [119]. Inorganic phosphate, or PPi, is a commonly known byproduct of DNA or RNA polymerase reactions for nucletotide base incorporations for DNA copying during cell division or for a variety of other applications such as polymerase chain reaction (PCR). Such reactions are critical for a wide variety of biological processes in living systems [120]. Pyrophosphate and diphosphate are very small molecules ($P_2O_7^{4-}$) which are highly mobile, which makes for easier and higher density detection with FET devices. These pyrophosphate molecules are a natural progression for testing FET sensors after initial pH testing before detection of larger molecules such as nucleic acids and proteins are attempted. With appropriate reaction components in solution, PPi and protons are repeatedly generated for a single reversible nucleotide base ad-

dition at the DNA polymerase binding site. As opposed to the detection of protons, as is employed in the work by Ion Torrent [13], PPi detection can be much more specific to the nucleotide reaction event, since many factors have the potential to adjust solution pH [121, 122]. Typically, detection of the activity of DNA polymerase and subsequent PPi release is accomplished using optical techniques such as chemiluminescence [122]. However, electronic biosensing offers an attractive alternative for many of the reasons already discussed in this dissertation.

In this work, we describe the use of nanoplate field-effect sensors, the fabrication of which was shown in Chapter 3, for the specific detection of pyrophosphate generated from on-chip DNA polymerase reactions. We illustrate the chemical modification of these SOI FETs with a compound technique that results in uniform films containing both a PPi specific chelator and DNA colonies on the surface. We then demonstrate the chip's electrical response to PPi alone, where chelators on the surface can capture the PPi and bring the molecules close to the gate dielectric of the devices, changing the source-drain current of the devices. The chelator molecules were designed for the specific binding of pyrophosphate that is released upon DNA polymerase-catalyzed base incorporation reactions. A schematic illustrating the chemical surface functionalizations is shown in Figure 4.1. dNTPs for the four possible bases are present in the solution, along with active DNA polymerase molecules. As dNTPs diffuse to the surface, they can attach to DNA colonies present on the surface which react with the DNA polymerase to result in a copy of the DNA base, which produces PPi as a byproduct. These PPi molecules can diffuse to other sites on the surface of the devices that contain chemical chelator molecules that can bind the PPi, which can be sensed by the device. Next, we demonstrate the use of the devices to sense the PPi generated off chip by mixing all of the reaction components together. Finally, the DNA colonies on the chip are amplified with rolling circle amplification (RCA) to generate increased sites for PPi generation, and the polymerase nucleotide addition reactions performed on chip are sensed by the FET devices.

Methods for silanizing the surface with 3-aminopropyltriethoxysilane (APTES) and subsequent chemical addition steps, including the development and attachment of the PPi binding chelator, the attachment of DNA colonies, and the rolling circle amplification steps for DNA, have been published [119, 123]

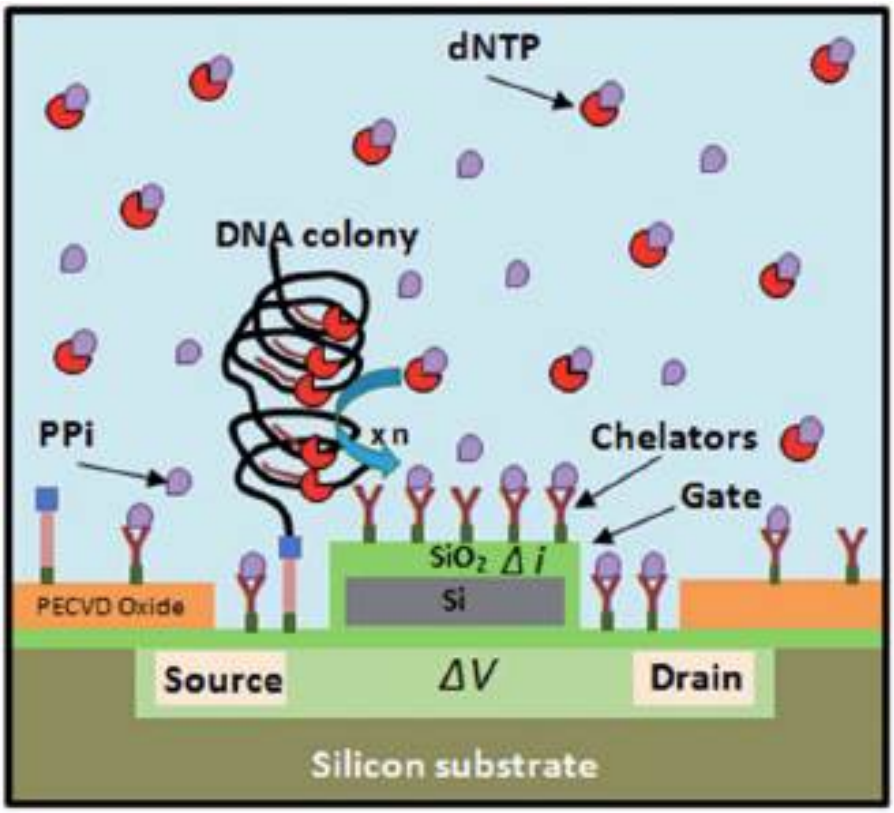

Figure 4.1: Schematic illustrating the chemical functionalization for the reponse to PPi generated from reactions on the surface. From [119].

and will not be discussed here. All electrical measurements were performed by sweeping the backgate of the devices from -10 V to +2 V instead of using the on chip fluid gate or an off chip reference electrodes. The source-drain potential was always kept at 100 mV for all measurements. An open PDMS well was used to contain fluid over the devices, and could be easily removed to rinse and re-use chips for several experiments. For RCA of the DNA, circular DNA was first attached to the surface, and one strand of the circular DNA was amplified to produce multiple copies of the same sequence. PCR was used to amplify one strand of a circular double-stranded DNA sequence. In this case, the sequence amplified was a 260 bp fragment of the pUC19 plasmid. This resulted in much higher densities of DNA on the surface available for interaction with the DNA polymerase in the on chip PPi generation studies.

Response of the devices to pure PPi in solution at various concentrations is shown in Figure 4.2. Stepwise shifts in the threshold voltage are seen for for 0.3, 0.6, 1.3, and 5.0 μM, with saturation after this concentration. These results show that the chelator molecules can bind the PPi at high density and induce shifts in the surface potential for the FET devices. The devices could be re-used in the same buffers or different buffers and conditions with significantly degrading the devices (Figure 4.2c).

Next, the devices functionalized with the dual composition film of both the chelator and the rolling circle amplified DNA colonies were exposed to the three conditions of varying degrees of complexity: (1) the exposure to 25 μM of pure PPi (Figure 4.3b and c), (2) the exposure to a solution containing the off chip reaction results of perfect match dGTP reaction solution which should contain high levels of PPi due to the reaction of the DNA polyermase in solution and to a control with mismatched primers (Figure 4.3d), and (3) the exposure to a 37 °C solution with just the DNA poymerase and dNTPs, demonstrating an on chip PPi generating reaction that could be sensed by the devices (Figure 4.3e) and a similar control reaction containing no DNA polymerase. All results were extracted from the average of three separate measurements on the same device to each solution. The schematic demonstrating all these varieties of reactions is shown in Figure 4.3a. These results demonstrate that the activity of DNA polymerase via binding of PPi can be detected successfully on the surfaces of our nanoplate bioFETs. The concentration of PPi on the surface is expected to be around 1-10 μM from

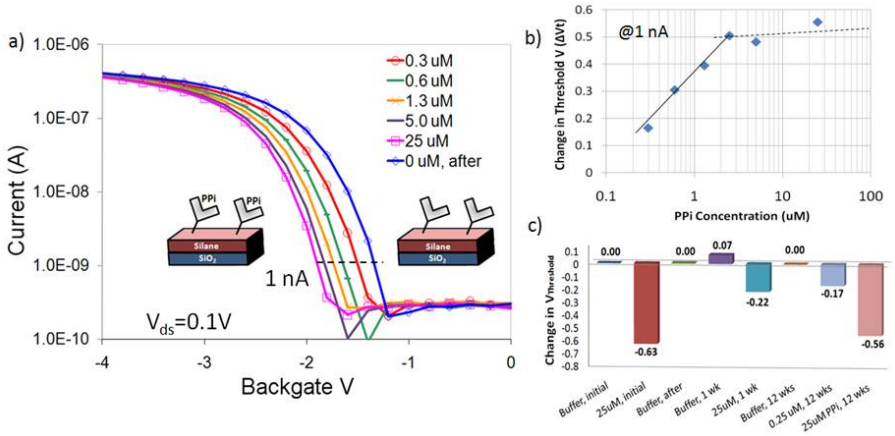

Figure 4.2: a: IV characteristics of a chelator modified device when exposed to varying concentrations of PPi, and after treatment with a dilute acid to remove the PPi. b: Shift in threshold voltage for the curves shown in (a). c: Shift in voltage needed to induce 1 nA of current through the devices as a function of surface modification and buffer composition over many days. From [119].

the magnitude of the shifts in threshold voltage, correspondoing to at least 2500 PPi molecules per DNA colony for a single base incorporation for a total of around 7.5x10^9 PPi molecules.

4.3 Detection of DNA Hybridization

The sensitive and selective detection of biomolecules, especially of DNA, is important for a number of applications, from gene sequencing to diagnostics of hereditary diseases by monitoring gene mutations. The silicon dioxide devices were used for the sensitive detection of DNA match and mismatch sequences. This section will describe the experiments, including the method for surface functionalization to attach the DNA to the surface, electrical characterization methodology, experimental sensing results, and a simulation model to support and help understand the results. The results in this section were extracted using a much simpler scheme for fluid placement and electrical measurement. Devices were simply probed with tungsten probes with micromanipulator, and DNA attachment and sensing were carried out with small droplets of fluid that were placed directly on the DNA surface

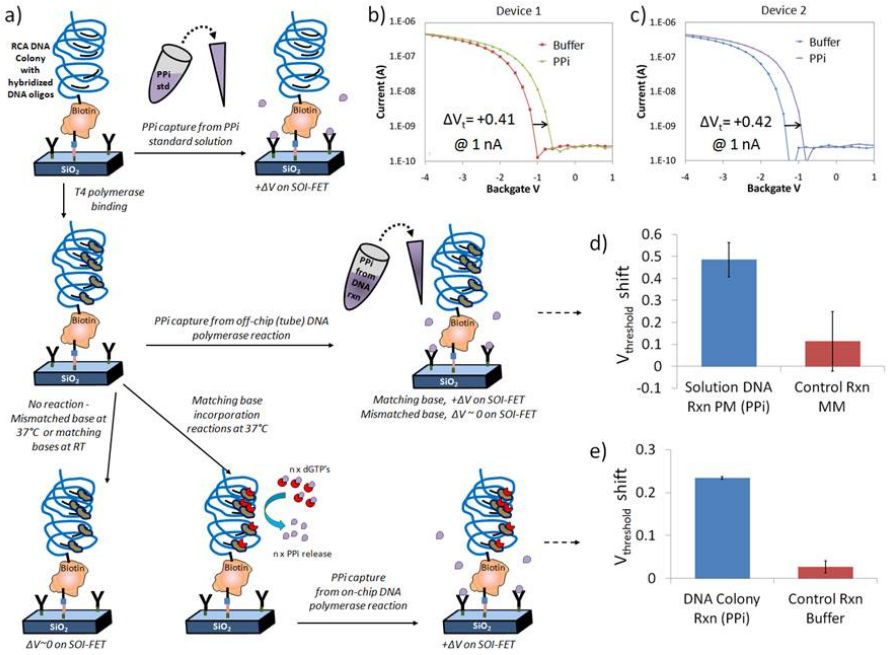

Figure 4.3: a: Schematic of a simplified chelator + DNA colony device surface as it is exposed to three different PPi standard solutions (top row), PPi generated in a reaction tube by polymerase reactions incorpoarting a matching DNA on linear DNA in solution (middle row), and PPi generated by multi-base (dGTP + dCTP) incorpoartion ractions on surface immobilized RCA DNA colonies (bottom row), b-c: response of two different devices on the same chip to 25 μM PPi standard solution in 1x PBS buffer. d: bar graph representing average of 3 measurements on same device after exposure to perfect match dGTP off-chip reaction solution, resulting in a positive change in threshold voltage (+0.49 V) compared to the control mismatch nucleotide solution (+0.11 V). e: bar graph representing the average response on the same device after 3 independent on-chip DNA polymerase reactions at 37 °C, generating PPi, compared to incubations in reaction buffer with no DNA polymerase. From [119].

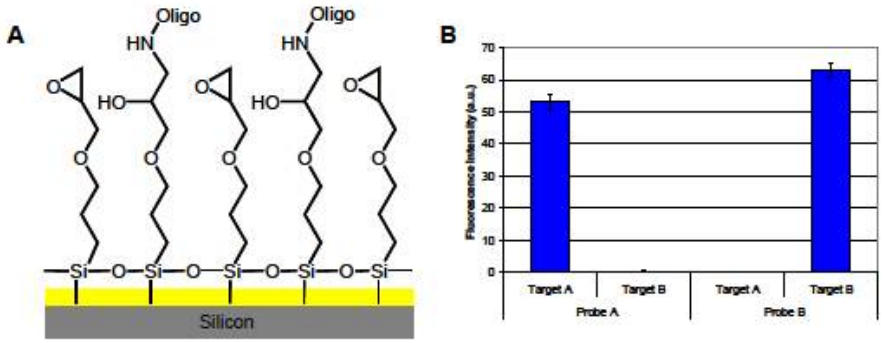

Figure 4.4: Surface chemistry for oligonucleotide immobilization. A - Schematic illustrating the DNA probe immobilized on the transducer surface using an epoxide functionalized surface. B - Fluorescence intensities for combinations of probes immobilized on the surface with epoxide chemistry and targets exposed on the surface.

without microfluidics. This allowed for a simple scheme for experiments. Due to the often high leakage currents in fluid when using a fluid reference electrode with the silicon dioxide devices, the device backgate was used as the main gate to accumulate the channel for transfer characteristic and current measurements.

4.3.1 Surface Functionalization

Epoxysilane coating on the devices was performed following previously established procedures [124]. Chips were cleaned with (H_2O_2 : H_2SO_4)(1:1) for 15 min, rinsed with copious amounts of DI water, and then were dried under high purity N_2 flow. Chips were then transferred into a glove box purged with nitrogen for protection from humidity. Next, chips were immersed in a 2.5% solution of (3-glycidoxypropyl)trimethoxysilane (Sigma-Aldrich) in anhydrous toluene, and were allowed to incubate at room temperature for about 24 hours. After incubation, chips were rinsed in toluene and methanol to remove species not covalently bound to the surface. Then the chips were placed in an oven at 120 °C for 30 min. We have observed that this coating retains functionality for at least a week after the procedure. For the experiments reported in this work, 10 μM probe molecules in a 150 mM sodium phosphate buffer (pH 8.5) were attached on the surface immediately after the bake by

Table 4.1: DNA sequences used for the experiments.

Probe A	5'-CCAACGGTTGGTGTGTG-C6-Amine-3'
Probe B	5'-CCAACGGACGTCGAATG-C6-Amine-3'
Target A (Match)	5'-CACACACCAACCGTTGG-C6-ROX-3'
Target B (Mismatch)	5'- CATTCGACGTCCGTTGG-C6-ROX- 3'

spotting 5 μL of the solution on the chip and incubating in a high humidity chamber for about 2 hours. The sequences of the oligonucleotides used for the experiment (Sigma Genosys) are listed in Table 4.1. A schematic of the resulting surface is illustrated in Figure 4.4A. The chip was then immersed in a pre-hybridization buffer, consisting of BSA (bovine serum albumin) 1% w/w in 3x SSC (saline sodium citrate) buffer for about one hour at room temperature to minimize the non-specific binding of species in further steps. This step enhances the target selectivity by blocking any unreacted active epoxy sites that might still be present on the surface. Experiments performed with fluorescent target molecules on functionalized non-patterned SiO_2 surfaces showed no detectable non-specific binding using this procedure (Figure 4.4B).

4.3.2 Electrical Measurements

Electrical measurements were performed with no further packaging of the device. The PECVD passivation layer provides adequate isolation of the metal leads from the electrolyte for the electrical measurements. Hybridization experiments with the sensors were performed by placing a 2 μL drop of DNA suspended in a 0.01x SSC buffer on the device (Figure 4.5A) using a micropipette, then measuring the source-drain current (Keithley 4200) through the device as illustrated in Figure 4.5B. During the measurements, the substrate was biased as a back gate, modulating the conductance of the device in order to obtain the device current as a function of the back gate bias. During the measurements, leakage current was monitored (at the substrate contact) to ensure the integrity of the devices and no significant leakage current was observed. Five minutes were allowed to pass for the hybridization (this settling time was chosen based on simulations of diffusion-limited capture of

molecules on sensor surface, which will be discussed in the next section), after placing the drop of solution containing the analyte at the appropriate concentration on the device. Subsequently, the current through the device as a function of the back gate bias was measured. In order to ensure that the actual hybridization event was being measured, the device was rinsed and spotted with the buffer solution only, and the current through device was measured again. This procedure was used first to measure the response to a mismatched sequence from concentrations of 10 fM to 1 μM, followed by response to a matched sequence in the same concentration range using the same device. Although a reference electrode for fixing the bias of the fluid was not used for the measurements, we have observed that the signal was stable when the data was obtained in the accumulation region of the device, and data is presented from this region. We observed instability in the sub-threshold region (likely due to the absence of reference electrode), and thus this data was not used.

4.3.3 Results and Discussion

The epoxy group on the surface reacts with amine groups on the probe DNA through a nucleophilic reaction to form a covalent bond. Epoxy functionalization has advantages in several aspects, such as a relatively high density of sites and reduced non-specific binding compared to other techniques [124]. For example, we have observed a significantly more uniform coating of probe DNA using epoxysilane when compared to using a poly-L-lysine modified surface. Also, with experiments performed with non-amine modified DNA oligonucleotides, we observed effective immobilization of the molecules on the surface. This suggests that the epoxide group reacts not only with the amine modification, but also with nucleophilic groups anywhere in the molecule. Thus, the probe molecules are linked more intimately to the surface, resulting in a higher sensitivity due to the proximity of the DNA backbone charge to the surface. On the other hand, the resulting configuration of the probe molecule may decrease the target binding affinity, which will severely degrade the device performance as discussed later. The orientation of the probe molecules and its surface chemistry dependent affinity is a topic which needs further experimentation and attention. The response of the device

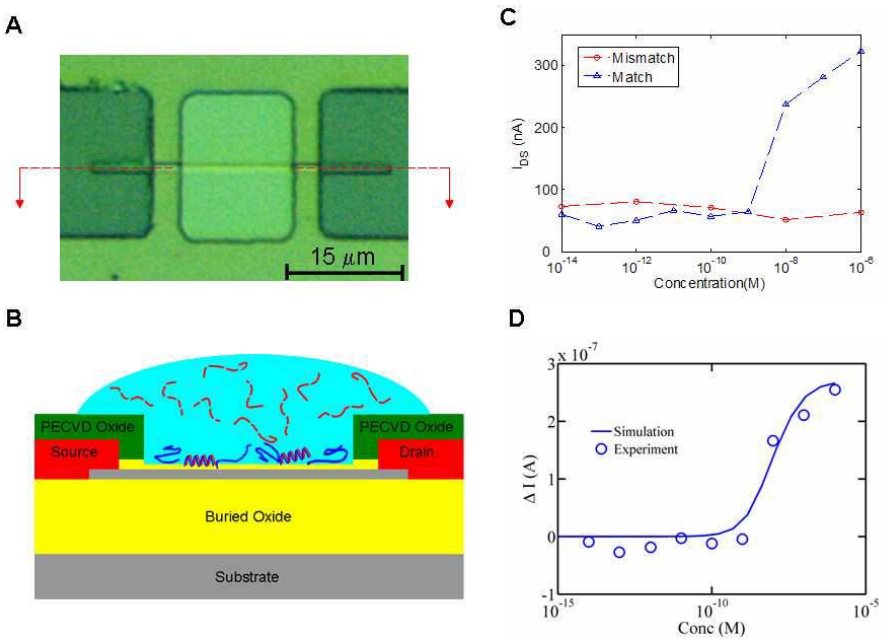

Figure 4.5: DNA hybridization detection using nanoscale thickness field-effect devices. A - Top view optical micrograph of a device. B- Illustration showing the cross-section of a device during the experiment. Solid blue lines represent the probe DNA, and the dashed red lines represent the target DNA. Substrate is biased during the experiments, and it acts as a back gate. C-Current versus analyte (match and mismatch) concentration measured in pure buffer after introducing the DNA. Source drain bias = 0.03 V, Back gate bias = -7 V. D - Change in current versus matched DNA concentration for the experimentally observed conditions (circles) and numerical simulations (solid line).

to mismatch and matched sequences of DNA, obtained by monitoring the source-drain current as a function of the analyte concentration, is shown in 4.5C. This measurement was executed by biasing the device in accumulation. The detection limit for the sensor for DNA hybridization was determined to be between 1 and 10 nM, while no detectable non-specific binding was observed in the range of concentrations used.

The sensor response obtained by simulations (by Pradeep Nair) predicts the experimental trends (Figure 4.5D). Finite measurement time (about 300 sec) and actual device dimensions were taken into account. The key parameters extracted using the model are: reaction coefficient $k_A = 2x10^7$ M^{-1} and surface concentration of DNA $N_0 = 3x10^{12}cm^{-2}$ (other parameters used are based on experimental conditions and literature: buffer concentration $I_0 = 1mM$, diffusion coefficient $D = 6x10^{-7}cm^2/s$ and oxide thickness $t_{ox} = 4nm$). We also perform measurements without the fluid on the devices before and after the hybridization experiments. Draining the fluid reduces the net amount of counter-ions around the hybridized molecules and we intend to explore the possibility of any improved sensitivity in dry measurements. Dry measurements also obviate the need of a reference electrode. Our measurements showed a net shift in the device characteristics associated with the hybridization event as shown in Figure 4.6A. The shift in the transfer curve of the device is an expected characteristic of the gating of the channel, which is a characteristic of any field-effect device [125]. Fluorescence images taken before and after the experiment (Figure 4.6A inset) also verify the attachment of the target molecules on the active area.

Excellent matches between simulations and experiments were obtained (see Figure 4.6B). Device simulations indicate that the observed shift in experimental device characteristics can be explained due to a net surface charge concentration (i.e., the net charge of the bio-molecules after screening due to the presence of any counter-ions, if any) of $\sigma_0 = 1.5x10^{11}qcm^{-2}$. This extracted charge density is about 20% of the net induced charge density in wet experiments (while detecting same concentration of target molecules). This indicates that although draining out the fluid reduces the net counter-ions, significant dissociation of hybridized molecules can also occur during the draining process.

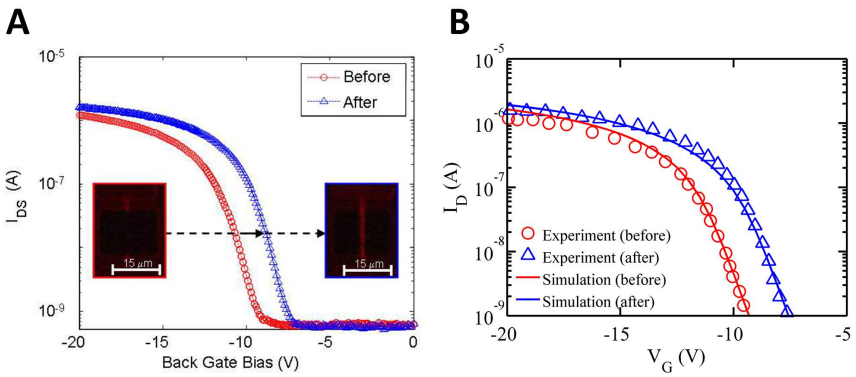

Figure 4.6: DNA hybridization detection using dry measurements A - Source drain current as a function of the back gate bias before (red circle) and after (blue triangle) the experiment. Inset shows the fluorescence image of the device before (left-hand side, red outline) and after (right-hand side, blue outline) the experiment. B - Comparison of the experimentally observed and numerically calculated curves.

4.3.4 Conclusions

In conclusion, we have demonstrated the operation of a nanoscale thickness SOI field-effect transducer as a DNA sensor, and through the verification of our simulation model provided a conceptual framework for the extension of this work to biomolecular field-effect sensing in general. Hybridization events with the matched sequence can be detected, and the device shows good selectivity, an important figure of merit for detection of analytes contained in real-life biological samples. The surfaces were functionalized using a versatile epoxy silane chemistry which can easily be extended to a wide range of biomolecules for immobilization. The measurement conditions were chosen based on simulations for a diffusion dominated regime. Experimental results are in good agreement with our proposed model and suggest a detection limit of 1-10 nM for the hybridization detection of DNA.

4.4 Detection of Immunoglobulin Proteins

To demonstrate the use of the silicon dioxide devices as protein sensors, we next used the devices for the sensitive detection of mouse-immunoglobulin (mouse-IgG1) from buffer solution. Antibodies are typically much larger

than DNA molecules and can be much more difficult to detect due to the distance of charge from the surface. This section will discuss the surface chemistry attachment protocol to attach the antibodies to the surface and the electrical results achieved with the silicon dioxide nanowire devices. Two sets of devices were used in these experiments. To explore the effect of the gate dielectric oxide thickness on results, the gate oxide was intentionally overetched in the last step of the device fabrication. This resulted in devices with both 80 Å thick and 150 Å SiO_2 gate dielectrics. The setup used for all fluid exchange with the exception of the surface functionalization and for all electrical measurements is as described in Section 3.3.3.

4.4.1 Surface Functionalization

To attach the antibodies to the surface, we employed a well studied vapor deposition of aminopropyldimethoxysilane (APDMS) [126]. We had previously characterized this vapor deposition extensively. Briefly, the devices were cleaned in an oxygen plasma environment at 300 W for 5 mins, then were immediately placed into a glass container containing a vial with 200 μL of pure APDMS mixed with 1% by volume of triethylamine (TEA), which acted as a catalyst for the reaction. The entire glass vial was sealed, and placed in an oven at 80 °C for at least four hours. The thickness of the monolayer as a function of time, showing the expected thickness of around 8.5 Å after saturation is shown in Figure 4.7. Through a variety of surface characterization techniques demonstrated previously [126], we have shown that this monolayer has high density, good uniformity, and good robustness in ionic fluids.

After the silane deposition, the devices were rinsed with acetone, methanol, and DI water, then were blowdried with nitrogen. The devices were then immediately placed into a vial containing a dual NHS-ester PEG linker molecule in DMF for at least 2 hours. This linker molecule contains NHS-ester functional groups on both sides which link to amine groups with high affinity and stability. The structure of this molecule as well as the entire attachment scheme is shown in Figure 4.8. After the attachment of the linker molecule, the devices were then placed in Texas Red labeled 10 μM goat anti-mouse IgG overnight to attach the probe protein molecule to the surface. Electrical

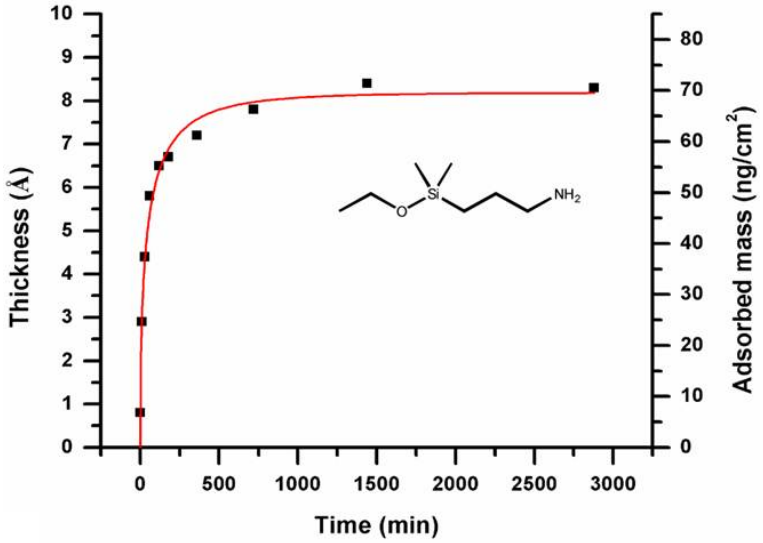

Figure 4.7: Deposition of APDMS as a function of time, measured by ellipsometry.

curves taken by sweeping the platinum reference electrode were taken before and after this attachment, and are shown in Figure 4.9. The fluorescence pictures showing the high density attachment of the Texas Red labeled probe before and after attachment are shown in the inset. A large threshold voltage shift and increase in fluorescence are observed, showing that the probe antibody has attached to the surface in high density.

4.4.2 Electrical Results

To demonstrate the selectivity of the devices, several control experiments were devised. Since IgGs are very large proteins (150,000 MW), larger proteins must also be utilized to demonstrate an effective selectivity. To test the non-specific binding of the devices a completely inert molecule, polyethylene glycol, of MW 100,000 was chosen as well as a similarly structured molecule in rabbit IgG. These molecules and proteins were flown over the device in 1 pM concentrations for 5 minutes and the Id-Vg curves taken in 1mM NaHCO3, 1mM KCl, pH 8.4. The curves for a nanowire device are shown in Figure 4.10B, and indicate little to no binding of these agents. The low salt concentration is utilized since the Debye charge screening length is proportional to the inverse square of the solution ionic strength. Thus, the lower the salt

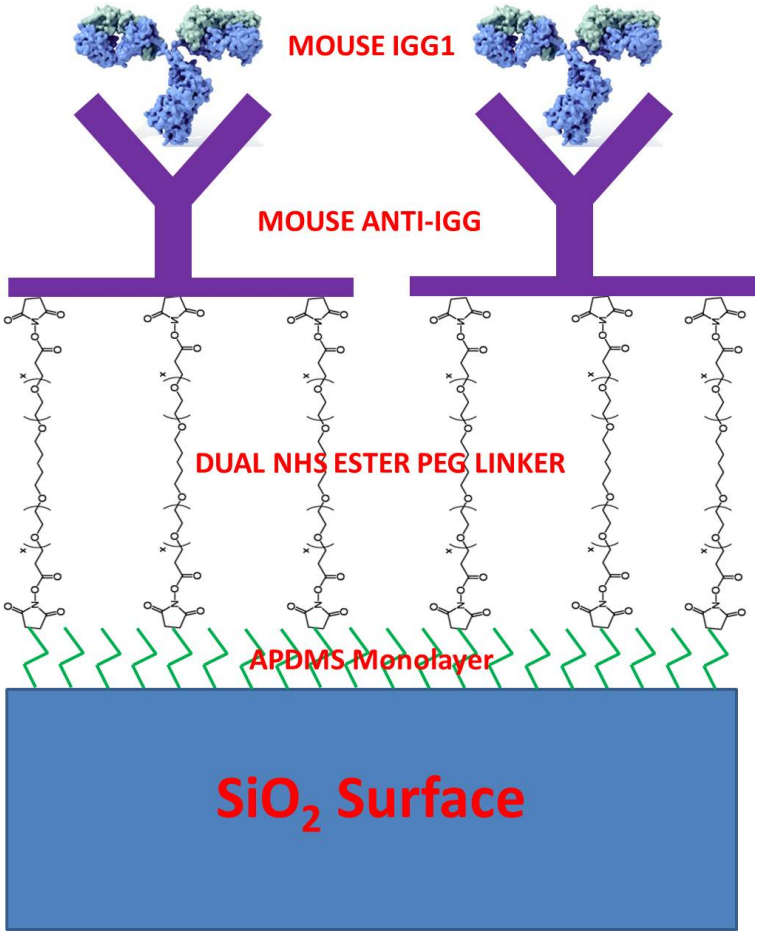

Figure 4.8: Schematic showing the surface functionalization scheme for attachment and detection of the mouse-IgG1 molecules.

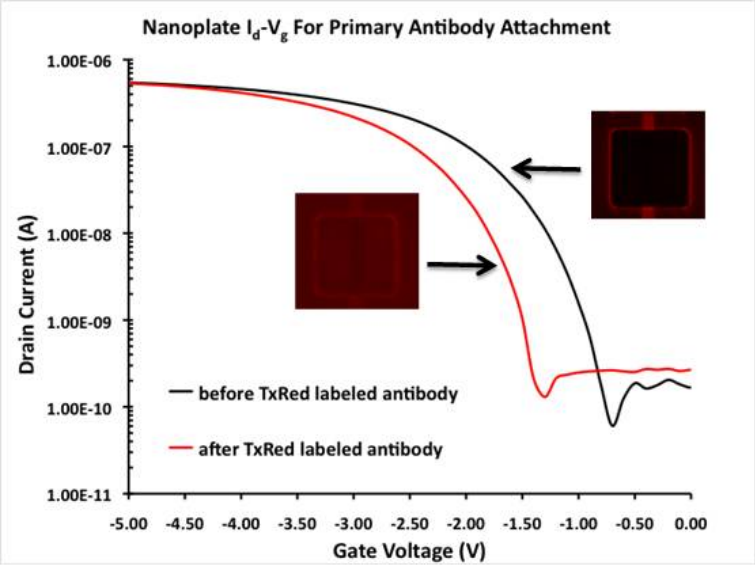

Figure 4.9: Electrical transfer characteristics and fluorescent pictures showing the attachment of the goat anti-mouse IgG.

concentration, the larger the amount of the protein charge density coupled to the device. Similarly, when concentrations of mouse IgG 1pM and above are introduced to the device, the threshold shifts are pronounced and can be seen in the Id-Vg curves for specific binding in Figure 4.10A.

The nanowires were exposed to even lower concentrations of mouse IgG, down to 8fM, while showing threshold shift magnitudes of over 200mV at this low concentration, as shown in Figure 4.11. As the mouse IgG concentration increases, the threshold voltage change saturates out, indicating binding sites on the device surface have saturated over the measuring time. The large dynamic range of the sensor, from 10fM (100fg/mL) to 10nM (100ng/mL), allows it to be compatible with a large volume of protein analytes found in organisms. The sensitivity of the nanowires to proteins as a function of oxide thickness was also tested using two different device sets, with 80 Å and 150 Å thick silicon dioxide gate dielectrics. By having a thinner oxide, the capacitance of the device increases allowing for changes in the oxide/electrolyte surface potential to lead to higher changes in silicon channel charge density. The nanowires were titrated with mouse IgG concentrations of 1 pM, 100 pM, and 10 nm, and the change in the threshold voltages plotted vs. the IgG concentrations (Figure 4.11B). A markedly lower response is seen with the 150 Å device, as is expected, demonstrating the importance of both

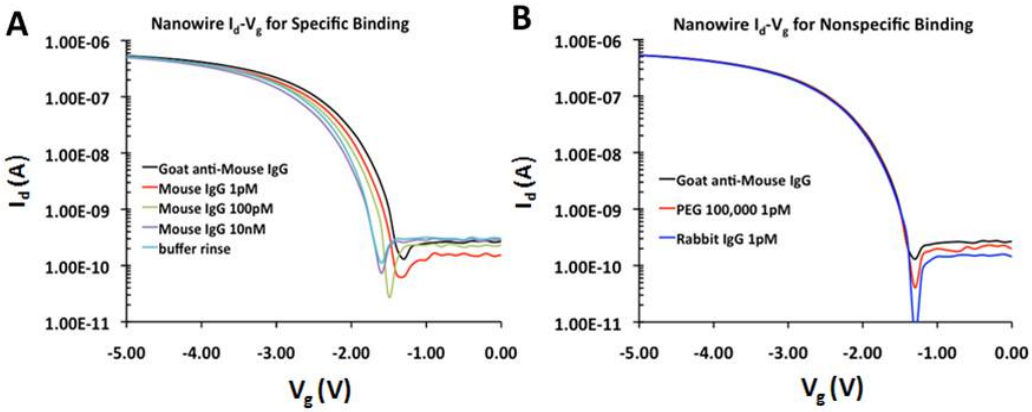

Figure 4.10: $I_d - V_g$ curves of a nanowire for various mouse IgG concentrations and the buffer rinse are shown in (A). The threshold voltage shifts to left with increasing protein concentration. Transfer curves for 1 pM concentrations of nonspecific binding analytes are in (B), showing a lack of threshold response.

the top oxide capacitance and the distance from the charge to the silicon channel.

4.4.3 Conclusions

In conclusion, we have used a very well characterized silane chemistry to attach goat anti-mouse IgG antibodies to the surface with high density. Using these probe molecules, we were able to detect mouse-IgG1 down to concentrations of 8 fM without hitting noise barriers, indicating that lower limits are possible. This demonstrates the silicon dioxide nanowire FET devices as true ultrasensitive biosensors of large protein molecules.

4.5 Conclusions

This chapter has demonstrated the sensing applications using the silicon dioxide devices as evidence that such devices can be used as powerful sensors of various biological entities. We showed the use of the devices as sensitive detectors of pyrophosphate byproducts of DNA polymerase activity, which can be used for a variety of applications, from PCR detection to sequencing

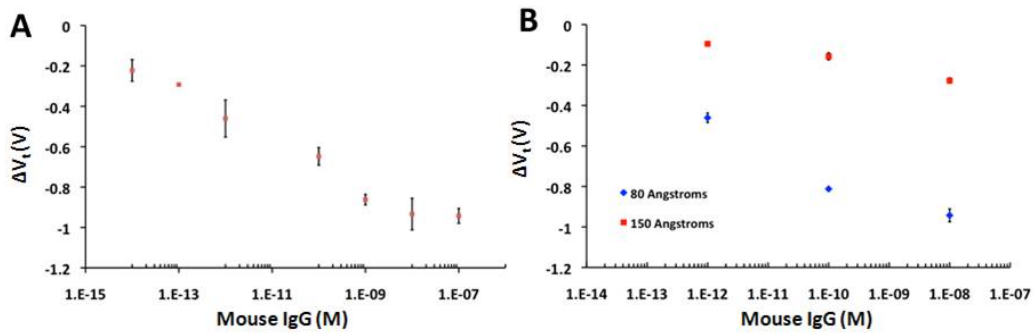

Figure 4.11: Change in threshold voltage of a nanowire for mouse IgG concentrations from 8 fM to 80 nM for an 80 Å thick oxide is in (A). A comparison between the threshold voltage shift for an 80Å and 150 Å oxide thickness is shown in (B) for the same mouse IgG concentrations. The shifts for the 80 Å oxide are much larger than for the 150 Å oxide.

by synthethis. We then showed the detection of short DNA oligomers down to 1 nM concentrations with the use of nanoplate FET biosensors. Finally, we demonstrated the detection of large protein molecules, mouse-IgG antibodies, down to 8 fM concentrations. These sensors serve as a baseline for improvements for the rest of this dissertation, which will describe various fabrication iterations and elucidate the criteria which can be enhanced.

CHAPTER 5

ALUMINUM OXIDE: A HIGH-K DIELECTRIC FOR IMPROVED PH SENSING

5.1 Introduction

This chapter will describe the development of high-k dielectric FET sensors for improved detection of pH. It will describe the fabrication differences from the baseline process discussed in Chapter 3, discuss the improved electrical characteristics of the device, illustrate the importance of proper backgate biasing for pH measurements, compare the pH results achieved with devices to that of the silicon dioxide baseline devices, and briefly discuss the effect of device width on pH sensitivity.

5.2 Fabrication Differences

A schematic illustrating some of the important steps in fabrication is shown in Figure 5.1. The main deviations from the baseline process in Chapter 3 were as follows:

- Dopant slowdown layer. The devices did not have a dopant slowdown layer, due to the necessity for removal of this slowdown before the deposition of the gate dielectric. For nanowire devices especially, such removal would be extremely difficult without compromising the buried oxide layer underneath. Simulations were performed to determine the effect this would have on doping concentration. Doping levels were shown to possibly decrease by as much as one order of magnitude (from $10^{20}/\text{cm}^2$ to $10^{19}/\text{cm}^2$). As a result, higher source-drain voltages were often needed. In all cases for aluminum oxide devices, if V_{DS} is not explicitly specified, it was set at 1.0 V. This still places the devices in the linear regime, but increases the source-drain current to well beyond

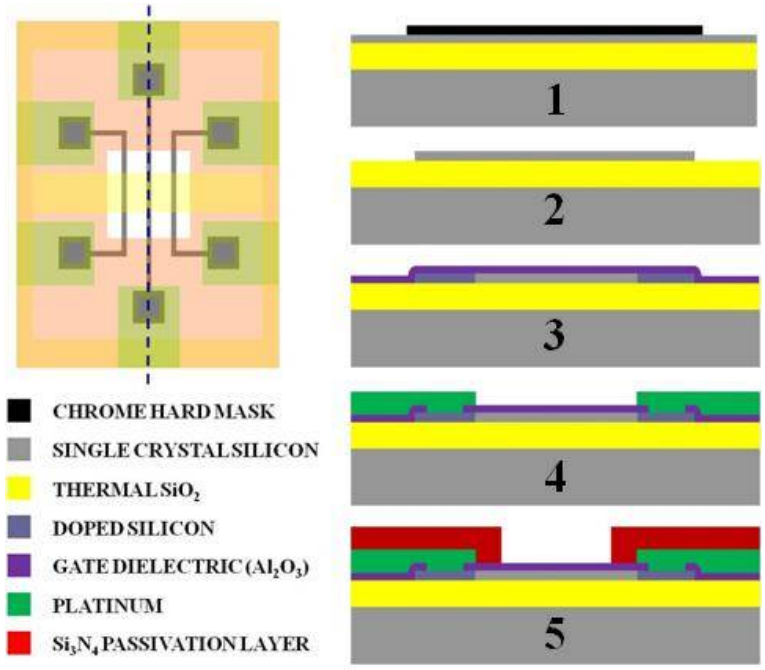

Figure 5.1: Fabrication process for the Nano-FETs. 1 – Patterning of chrome hard mask via electron beam and optical lithography. 2 – Wet etch of the active silicon area with TMAH. 3 – Deposition (Al_2O_3) or growth (SiO_2) of the gate dielectric. 4 – Deposition and patterning of platinum as the metal contact; contact is made with via holes into the silicon. 5 – Deposition of Si_3N_4 passivation layer, followed by etchback to expose the devices and the fluid gate.

the measured noise.

- Formation of gate dielectric: For the silicon dioxide devices, the gate oxide was thermally grown with careful timing to ensure that the target thickness was achieved. For these aluminum oxide devices, the thickness of the gate dielectric could be controlled with much more precision. 75 cycles of atomic layer deposition (ALD) was used for conformal deposition of the aluminum oxide layer, typically with a thickness of 150 Å compared to the 100 Å thick SiO_2 devices.

- Final etchback step: For the silicon dioxide devices, the final etchback step to create holes above the devices to expose the channel to the fluidic enivonrment was executed on a die-by-die basis, with careful timing to ensure that the gate dielectric was not damaged if an overetch of the PECVD oxynitride occurred. The ALD Al_2O_3 layer served as an extremely good etch stop in the dry CF_4 RIE step (etch selectivity of more than 60:1 for PECVD oxynitride:Al_2O_3 [127]). As a result, for the aluminum oxide devices, the final etchback step could be performed on a wafer level, which enormously adds to convenience and scalability of the process. Furthemore, the physical gate dielectric thickness from die to die had much less variability for the Al_2O_3 devices, again due to its excellence as an etch stop.

Besides these three modifications, the fabrication for the devices used in this chapter was extremely similar to the baseline process.

5.3 Choice of a Fluid Electrode

Ideally, the fluid electrode chosen should be a standard reference electrode with a surface potential that is independent of environmental conditions: that is, the E_{ref} term in Equation 2.11 should not be a function of pH, time, ionic concentration of solution, or any other environmental factor. The internationally accepted primary reference is the standard hydrogen electrode (SHE) or normal hydrogen electrode (NHE), which consists of a platinum electrode in solution with an unlimited supply of H_2 gas. All other electrodes are typically cited with potentials vs. the NHE. For example, the commonly

used silver-silver chloride (Ag/AgCl) electode has a potential of 0.197 V vs. NHE [128]. Standard reference electrodes have a shift in potential vs. NHE, but can still be used to bias solutions reliably if their phases have essentially constant compositions over time and solution conditions.

Ag/AgCl electrodes are the most commonly used electrodes for this purpose, since it is difficult to use an electrode with hydrogen gas. Another common electrode is called a saturated calomel electrode (SCE), which has an electrochemical half cell $Hg/Hg_2Cl_2/KCl$. If a standard electrode is not used to bias the fluid, then adjustments need to be made to the measurements to ensure that any changes in the surface potential at the reference electrode itself are accounted for.

In the rest of the experiments in this chapter, the on-chip platinum electrode (without H_2 gas) was used to bias the fluid. This was due to ease of use in a closed microfluidic channel, which was deemed to be the best solution for clean exchange of fluids over the chip. However, without hydrogen gas to replenish the surface of the platinum electrode, platinum is well known to have a surface potential that changes both as a function of time in solution [128] and pH [128, 129]. To account for this effect in all measurements, the open circuit potential for platinum vs. a standard reference electrode, a silver-silver chloride electrode, was measured as a function of both solution pH and time in solution. Results are shown in Figures 5.2 and 5.3. These experiments were performed in the Robinson buffer solutions that were used in the pH measurements that will be described later. Both of these experiments were repeated numerous times because most of the results in this chapter depend on these measurements. A slope of -41 mV/pH vs. Ag/AgCl and 1.95 mV/min vs. Ag/AgCl was noted for the on-chip platinum electrodes. This data has been used as a correction factor for all pH data shown in this chapter. Without these correction factors, the data can appear to be quite misleading: for example, the devices were believed to exhibit pH detection highly exceeding the Nernstian limit before these issues were clarified.

5.4 Carrier Simulations

To obtain the carrier concentration profile inside the silicon channel as a function of the back gate bias, we used Medici with the two-dimensional pla-

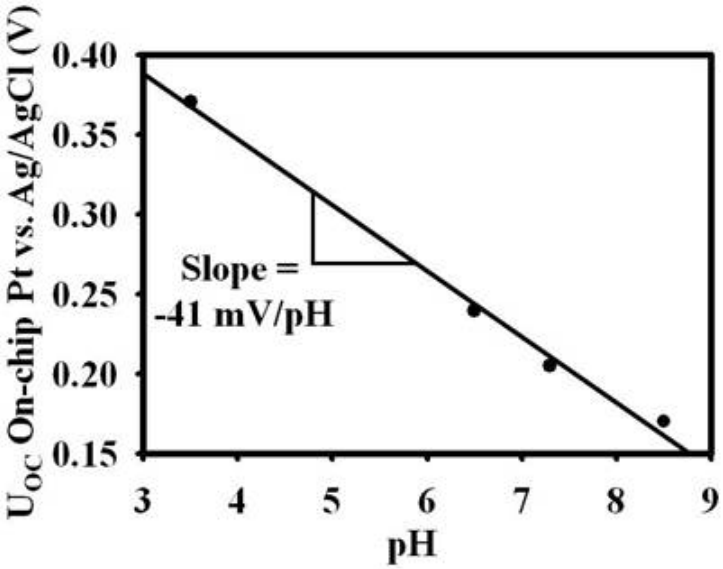

Figure 5.2: Measured open circuit potential between the on chip platinum fluid gate and a reference Ag/AgCl electrode as a function of pH.

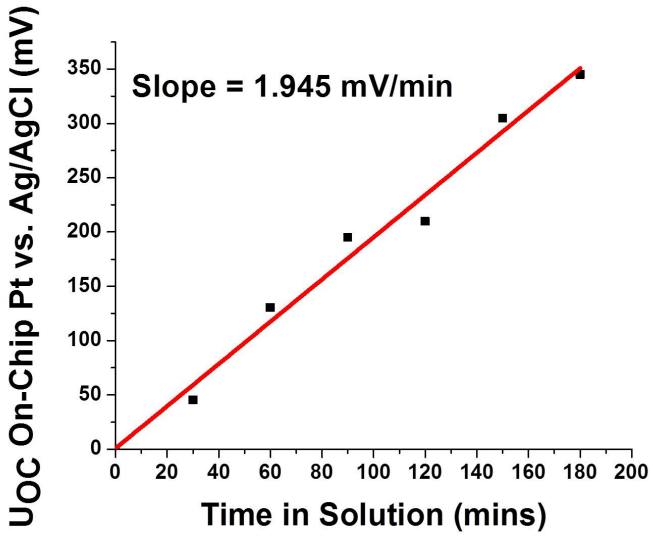

Figure 5.3: Measured open circuit potential between the on chip platinum fluid gate and a reference Ag/AgCl electrode as a function of time in fluid.

nar structure. We modeled the electrolyte between fluid gate and top oxide as an insulator with thickness of 5 nm and dielectric constant of water (78.5 in the simulation). Since we used 5 mM electrolyte in the experiment, the corresponding Debye length (-5 nm) can be reasonably used for the thickness of electrolyte layer. We also assumed that the fluid gate bias is negative (-1 V in the simulation), and the OH surface group is a negative (-10^{13} cm^{-2} in the simulation) fixed charge on the top oxide surface since the usual range of electrolyte pH is higher than the point-of-zero charge (pH_{pzc}) of SiO_2 surface, which is equal to 1-3. To see the effect of the back gate bias, we used two different values of V_{BG} for the simulation: -7 and +3 V.

5.5 Calculation of Threshold Voltage

Threshold voltage for each of the transfer curves was extracted using a simple constant current method that is demonstrated in Figure 5.4 (shown for a silicon dioxide 50 nm wide nanowire device). Because the subthreshold slope was observed to be relatively constant for varying pH (the curves are parallel to one another at different pH values), simply extracting the voltage at which the source-drain current dipped below a certain value could be used as a first order measurement of the threshold voltage shifts induced by changes in pH.

5.6 Theory

Fundamentally, for traditional MOSFETs, ISFETs and nanoFETs, the change in channel charge resulting from potential changes at the oxide/fluid interface is given by:

$$\sigma_{silicon} = -C_D \Delta\psi_0 = \frac{\epsilon_r \epsilon_0}{t_D} \Delta\psi_0 \tag{5.1}$$

where C_D is the dielectric capacitance, $\Delta\psi_0$ is the change in surface potential at the oxide/fluid interface, ϵ_r is the dielectric constant of the gate dielectric (3.9 and 9 for SiO_2 and Al_2O_3, respectively) [130], and t_D is the thickness of the dielectric. The coupling of changes in potential at the surface to changes in charge in the silicon, given by the dielectric capacitance, is a critical factor that ultimately determines device sensitivity. To increase

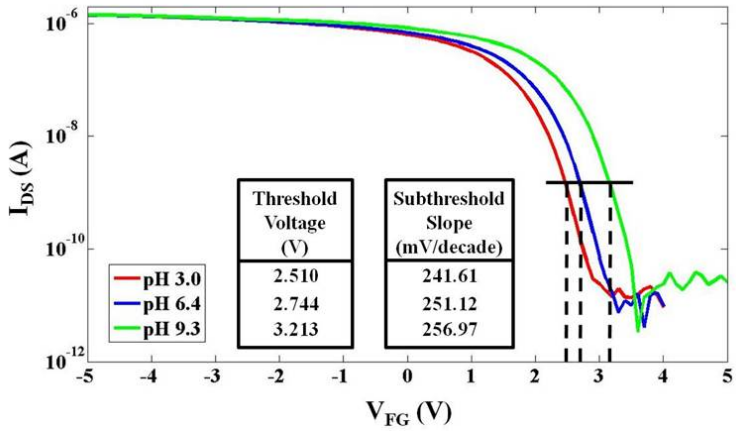

Figure 5.4: Extraction of threshold voltage shifts. The transfer curves for a 50 nm wide nanowire device immersed in pH solutions of 3 different pH values (3.0, 6.4, and 9.3) are shown, included with the threshold voltage and subthreshold slope of each curve. Since the curves are relatively parallel to one another, the threshold voltage shifts can be extracted by simply calculating the voltage at which each curve dips below a current threshold.

this coupling, either the thickness of the gate dielectric can be reduced or a material with higher dielectric constant can be used. For example, the recurrent theme with traditional SiO_2 MOSFET devices was to reduce the gate oxide thickness continuously until undesirable gate leakage currents crippled device operation [131]. When similar devices are used in ionic fluids as is the case with FET biosensors, these leakage issues are even further exacerbated. Thus, a logical solution to this problem is to use thicker gate dielectrics with higher dielectric constants for devices which exhibit similar if not higher sensitivities when compared to silicon dioxide devices. The increased thickness of these high-k dielectric devices results in robust devices that are much less susceptible to gate leakage issues. Al_2O_3 is known to be a good compromise between available high-k dielectric due to a dielectric constant that is higher than that of SiO_2 without substantially sacrificing the band gap of the oxide, which is another important consideration for reducing gate leakage currents [130]. Our work here demonstrates the first such use of a high k-dielectric as the gate oxide for nanowire biosensor applications. We use pH sensing as a benchmark to study the effect of three critical parameters on the device performance using experimental results and supporting simulations: the employed gate dielectric, the use of a back gate, and the device

width. We demonstrate that our devices are stable and operate in fluidic environments for up to 8 hours, quantified by threshold voltage stability and leakage current characterization. In addition, we performed a robustness comparison of the aluminum oxide devices and more typical silicon dioxide devices to show that the high-k dielectric devices exhibit better functionality over many electrical sweeps in fluidic environments. This is primarily due to the possibility of increasing the thickness of high-k device gate dielectrics without compromising sensitivity. Next, we discuss how the back gate bias condition can be optimized to lower the effective electrical thickness of the device, thereby enhancing sensitivity. This is a general technique that can be used for any gate dielectric or sensing platform that employs a back gate structure. This technique was then used to perform a direct comparison of the observed pH response of 150 Å thick Al_2O_3 devices to 100 Å thick SiO_2 devices. The high-k dielectric devices exhibited an average improvement of pH sensitivity over their counterpart SiO_2 devices of around 2. Lastly, we perform a comparison of the pH responses of Al_2O_3 devices with identical characteristics except for differing widths. We show that when using the back gate bias optimization technique, pH response is virtually independent of device width. This opens the possibility of the use of microscale devices that are much easier to fabricate with the use of standard lithography.

5.7 Electrical Device Characterization

Initial Al_2O_3 device characterization was performed in air (without fluid on the devices) utilizing the back gate (V_{BG} in Figure 5.5). Both 50 nm wide nanowire devices and 2 μm wide nanoplate devices showed normal transistor behavior as the drain source current (I_{DS}) was measured while the back gate voltage was varied (Figure 5.6). Next, the devices were placed in a 0.01x phosphate buffered saline (PBS) solution to measure the characteristics in fluid. The fluid gate voltage (V_{FG}) was swept from -5 to +5 V for backgate biases from +5 to -8 V (Figure 5.7). This demonstrates full double gate operation of the device; device current is modulated effectively by the fluid gate, and the different back gate biases correspond to shifts in the threshold voltage of the I_{DS}-V_{FG} curves. Very similar characteristics were observed with silicon dioxide devices as was shown in Chapter 3. Shifts in threshold voltage

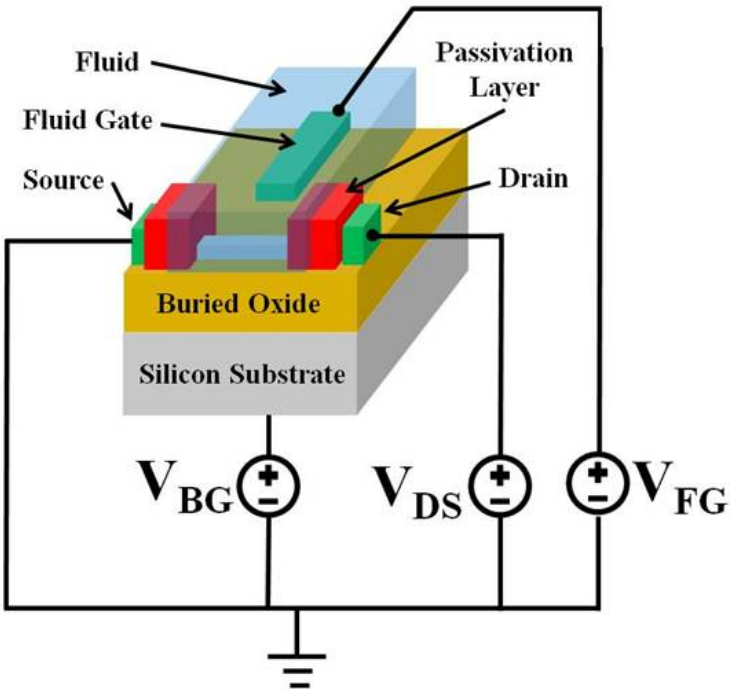

Figure 5.5: Schematic demonstrating the measurement scheme for the nanoFETs. DC voltages are applied to the back substrate as a backgate (V_{BG}), to the on chip platinum reference electrode as a fluid gate (V_{FG}), and to the drain (V_{DS} = 1 V for all experiments). Current is recorded from source to drain for the device.

transfer curves were used for most experiments as a measure of changes in surface potential of the silicon to allow for comparisons that minimized the effect of device to device variation.

The devices were found to be very reliable for fluidic measurements, which was quantified by measuring the threshold variation, leakage currents, and device lifetimes in fluid. To determine the minimum observable shift in threshold voltage that could be considered real, we quantified the representative noise by measuring the threshold voltage of five aluminum oxide nanowire devices as a function of time for up to 8 hours, which is much longer than any typical experiment should take. The devices showed excellent threshold voltage stability over 8 hours in fluid (Figure 5.8), and also showed minimal changes in leakage currents even when tested over 10 months where the same device was exposed to fluid for about 30 minutes for each measurement (Figure 5.9). This device stability can be attributed to the proper protection of

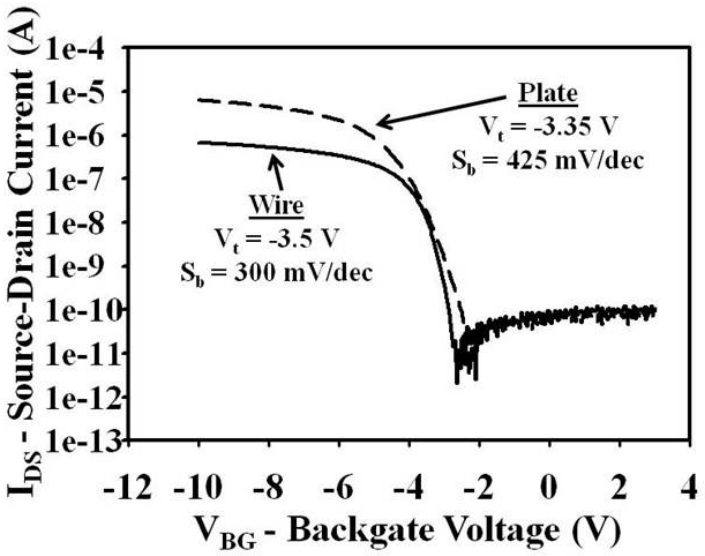

Figure 5.6: Typical dry device operation for Al_2O_3 nanoFETs: both a 50 nm wide silicon nanowire and a 2 μm wide silicon nanoplate. Source-drain current (log scale) as a function of the applied backgate voltage. Included are the extracted threshold voltages and subthreshold slopes for the devices.

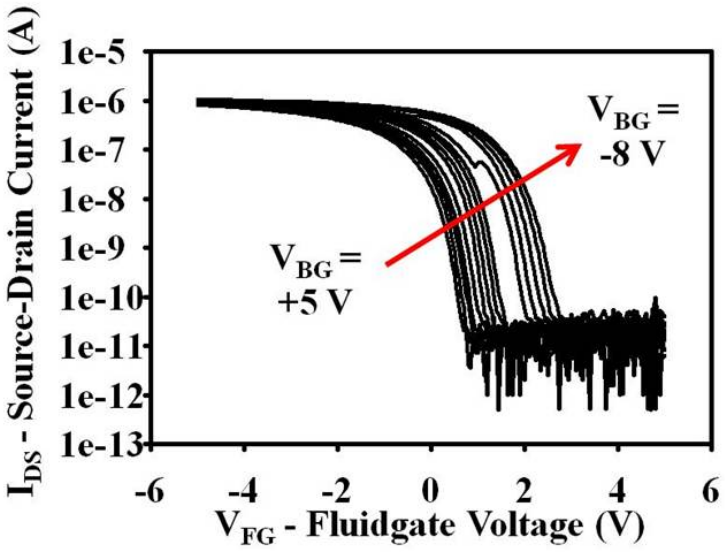

Figure 5.7: Measured source-drain current for an Al_2O_3 nanoFET in pH 7.4 0.01xPBS buffer solution the applied fluid gate is swept for many different applied backgate biases.

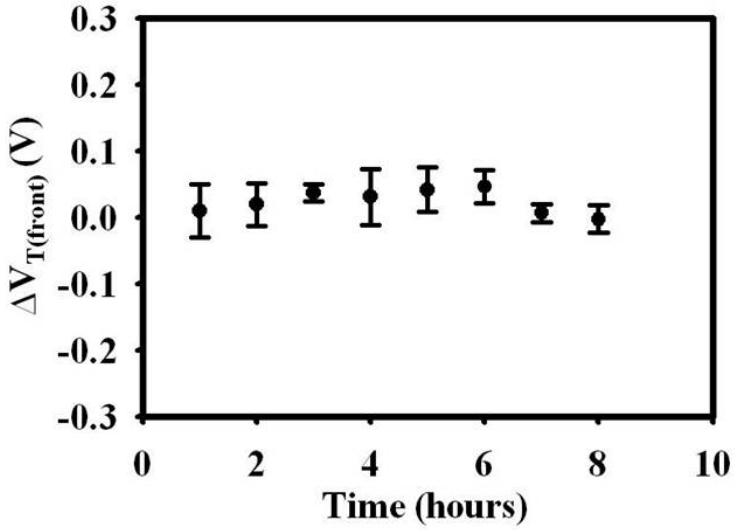

Figure 5.8: Front threshold voltage versus time for 5 Al_2O_3 nanoFET devices demonstrating device stability. Very little shift in threshold voltage over time is observed for up to 8 hours in Robinson buffer (pH 7.5). This allows us to determine our minimum detectable shift in threshold voltage (50 mV).

the electrical components from fluid with the silicon nitride insulating film as shown from the cross sections of the device. From the minimal threshold voltage drift, we found the minimum detectable change in threshold voltage for our system to be around 50 mV; any shifts in the raw data below this amount were not considered to be numerically significant. In addition, a study was performed directly comparing device robustness of the Al_2O_3 devices to typical SiO_2 devices. When the two sets of devices were exposed to the same pH solutions and biasing conditions, a large percentage of the SiO_2 devices began to fail much earlier than the Al_2O_3 devices (Figure 5.10). Device failure was defined as either the presence of leakage currents higher than the source-drain current or as the lack of normal transistor behavior. The predominant factor responsible for this increase in device robustness is a thicker gate dielectric layer; with the Al_2O_3 devices a 150 Å thick gate dielectric could be used, whereas for the SiO_2 devices a thinner gate dielectric (about 100 Å) was needed to see reasonable pH response.

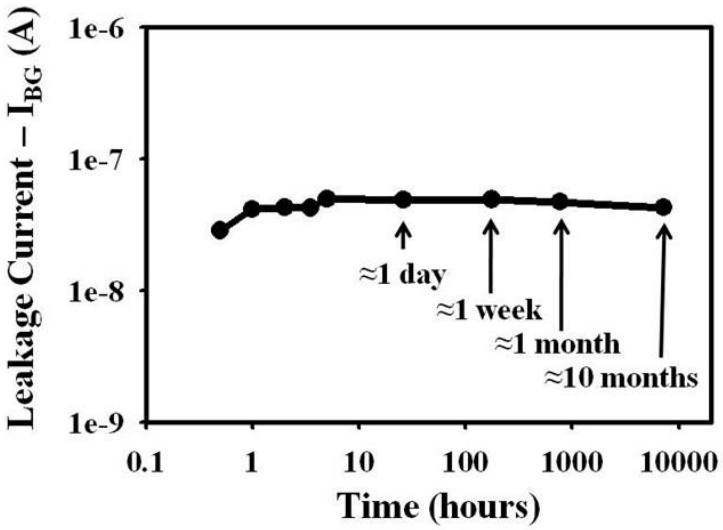

Figure 5.9: Measured back to front leakage current as a function of time in 0.01x PBS for a 50 nm wide aluminum oxide nanowire device. Devices are observed to maintain low leakage currents many months after initial measurement in fluid.

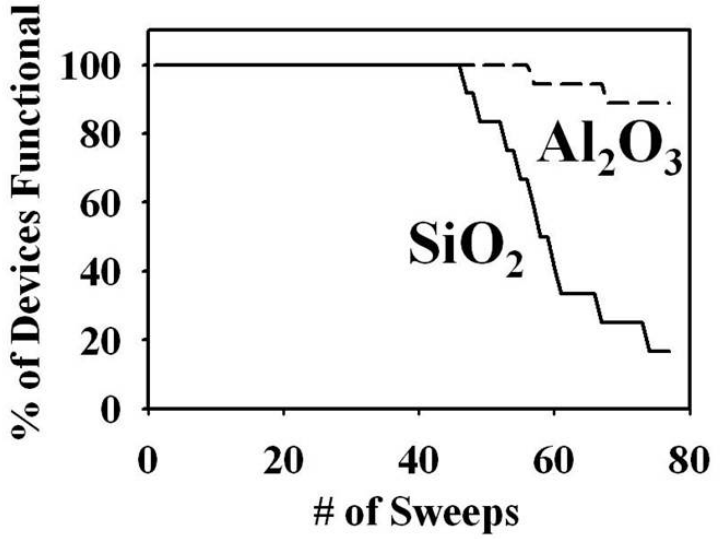

Figure 5.10: Device failure for SiO_2 and Al_2O_3 devices as a function of the number of sweeps (-5 V to +5 V) applied to the fluid gate at various backgate voltages in 10 mM, pH 7 Robinson buffer solution.

5.8 Dependence of pH Sensing on Backgate Optimization

The devices were first used to demonstrate the utility of the back gate during sensing. Recent reports singled out the careful tuning of the applied fluid gate bias to place devices in the subthreshold regime as a useful tool for maximizing the sensitivity of both pH and protein detection [105, 106]. Fundamentally, the Debye length can be varied in the silicon channel. The Debye length dictates how far electric fields will penetrate into the silicon channel and is given by:

$$\lambda_{Si} = \sqrt{\frac{\epsilon_{si}\epsilon_0 kT}{q^2\rho}} \tag{5.2}$$

where ϵ_{si} is the dielectric constant of silicon,k is the Boltzmann constant, ρ is the net charge density, and q is the elemental charge (λ_{Si} ≈1-2 nm for $\rho = 10^{18} - 10^{19}$ cm^{-3}). In response to charge modulation at the gate dielectric/fluid interface due to pH or protein binding events, changes in carrier concentration in the channel will occur principally within a Debye length away from the gate dielectric/silicon interface. By using the applied bias to reduce the net charge in the channel, the Debye length is increased, allowing for a higher percentage of the silicon channel to feel changes in charge at the surface, leading to increased sensitivity. In this work, we show that the applied back gate bias can be similarly utilized to modulate the effective electrical device thickness. Distinct from a recent report, which demonstrated pH responses above the Nernstian limit by measuring shifts in the threshold voltage sweeping the back gate [132], our work uses the back gate only to optimize the silicon channel while sweeping the front fluidic gate potential. This method measures surface potential shifts at the sensing interface, which is of direct interest. The concept is analogous to accumulation mode fully depleted double-gated SOI MOSFETs [133–135] and is illustrated schematically in Figure 5.11. Assuming that the front gate has been biased to place the top part of the channel into accumulation, changes in surface charge will only be felt a few nanometers into the top surface of the channel. If the back gate is biased to put the back of the channel into accumulation (V_{BA} less than -5 V for most of the devices in this work), then a significant part of the 30 nm thick channel will conduct current that is insensitive to changes

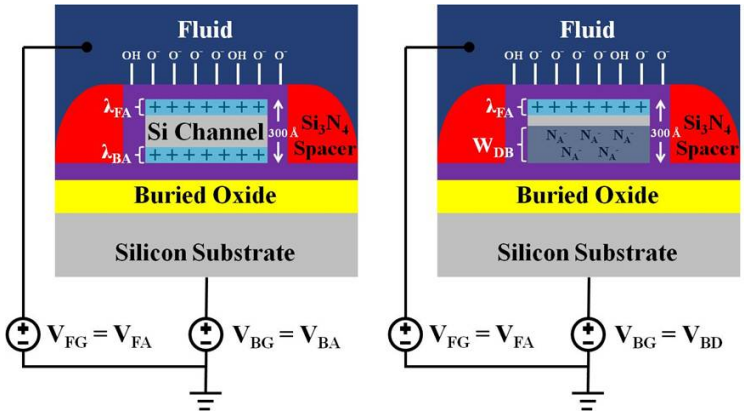

Figure 5.11: Schematic demonstrating the concept of using a backgate voltage to modulate the effective electrical thickness of the channel. On the left, when the back surface of the silicon is assumed to be in accumulation, a large percentage of the cross sectional area of the conductive channel (anything below the Debye length from the front) will not sense changes in charge at the dielectric-fluid interface. On the right, when the back surface is placed in depletion, the effective conductive thickness of the channel has been reduced so that the majority of the channel can detect charge. The fluid gate is assumed to be biased in both cases to place the front surface in accumulation.

in surface charge (Figure 5.11, left). Alternatively, if the back gate has been biased such that the channel is depleted except for the top accumulated surface (Figure 5.11, right), the effective electrical thickness of the device has now been reduced to the order of a few nanometers. In this case, changes in surface charge directly influence the entire electrically active area of the channel, which will lead to increased sensitivity. The physical thickness of the device, at 30 nm, is much less than the theoretical maximum achievable depletion width for a 10^{15} p-type doped channel ($\approx$ 800 nm). Medici, a 2D device simulation tool, was used to simulate the net carrier concentration as a function of the vertical position in the channel (Figure 5.12), with an applied front gate voltage of V_{FG} = - 1 V and two different back gate voltages, V_{BG} = -7 V and -4 V. A silicon surface carrier concentration on the order of 10^{18} at the top channel/gate dielectric interface was simulated for both back gate accumulated and depleted. However, when the back silicon accumulates, an additional channel forms at the back gate. This channel will be insensitive to charge changes at the front, thus reducing overall sensitivity. The expected trends were then confirmed experimentally.

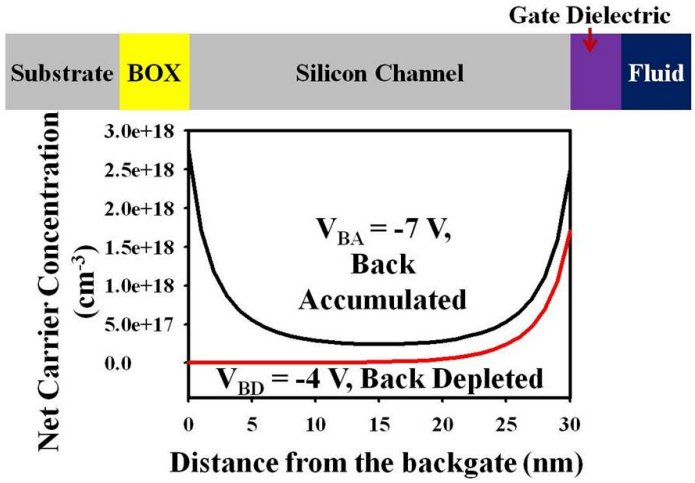

Figure 5.12: Simulated carrier densities in the channel of nanoFET devices for the case of back accumulated (V_{BA} = -7 V) and back depleted (V_{BD} = -4 V). The front gate was accumulated at V_{FG} = - 1 V, and the concentration of charged sites on the surface was taken to be $N_s = 10^{13}$ cm^{-2}.

pH experiments over the devices were performed using the setup described in Section 3.3.3. Any of ten devices connected to the electronic setup could be measured via control with the central computer, allowing for easily testing multiple devices at each pH point. This was especially useful in the real time measurements, where current or conductance was measured as a function of time. Multiple syringes and syringe pumps were used to slowly flow the solutions through the microfluidic system, over the chip, and finally into the waste receptacle at a rate of a few μL per minute. Typically, to ensure that a pH solution had been fully exchanged over the surface, each point was flown for at least 15-20 minutes over the device before the measurement was performed. Robinson buffer pH solutions were made using 1 mM acetic, 1 mM phosphate, and 1 mM boric with titrated HCl/NaOH to obtain the desired pH. All pH solutions were measured at the conclusion of the experiment to ensure that the pH had not changed significantly during the course of the experiment. Robinson buffer solutions have good pH stability over a wide range of pH values due to being composed of various salts with pKa values at different values over 2-9. As the solutions slowly flowed over the surface of the 50 nm wide Al_2O_3 devices, drain source current was measured as a function of applied fluidic gate bias at two fixed back gate biases to put the back silicon first in accumulation then depletion. An example of a typical result

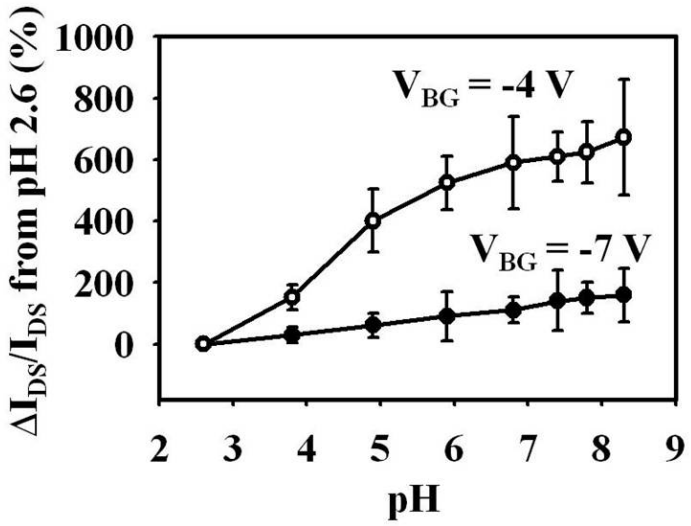

Figure 5.13: Experimental data showing the percentage change in current from the current at pH 2.6 for three 50 nm wide Al_2O_3 nanowire devices at two different backgate voltages in accumulation and depletion (V_{BG} = -7 V and V_{BG} = -4 V). A higher sensitivity is noted in the case of the back depletion. Error bars were calculated as the standard deviation of the percentage error for the three employed devices.

is shown in Figure 5.13, at an applied fluid gate of V_{FG} = 1.5 V. When the back silicon was placed into accumulation, at V_{BA} = -4 V, a distinct increase in current of around 100% of the original value was observed when varying the pH from 2.6 to 8.3. However, when the back was placed into depletion (V_{BD} = -7 V), a far higher change was observed: up to 700% increase in current, which matches the predictions of the Medici simulations.

5.9 Comparison of Al_2O_3 Devices to the Baseline SiO_2 Devices for pH Sensing

Next, we used the back gate optimization technique to compare the performance of devices with Al_2O_3 gate dielectric against SiO_2, which has been traditionally used in nanoscale field effect biosensors. Al_2O_3 films are expected to have greater sensitivity to pH changes than their SiO_2 counterparts. When biosensor device sensitivity is defined as $S = \Delta G/G_0$, Nair et al. showed that device sensitivity is linearly proportional to ϵ_r, and can be

written as [111]:

$$S = \frac{2\epsilon_r \epsilon_0 \psi_0 N(t)}{qa^2 N_D log(1 + \frac{t_D}{a})} \tag{5.3}$$

where $N(t)$ is the density of charge states at the surface, a is a geometry parameter, N_D is the doping of the silicon, and t_D is the thickness of the gate dielectric. The linear relationship here between the dielectric constant and the predicted sensitivity is a direct result of increase in the oxide capacitance as was discussed earlier. In addition, for pH sensing, the change in surface potential for an ISFET sensor (which is directly relevant here) is given by [48]:

$$\psi_0 = \frac{-2.3\frac{RT}{F}\Delta pH}{(2.3kT/q^2)(C_s/\beta_s) + 1} \tag{5.4}$$

where C_s is the differential double layer capacitance (dependent mostly on the ion concentration of the solution) and β_s is the buffer capacity of the surface, which is known to be markedly higher for Al_2O_3 when compared to SiO_2 [48]. The sensitivity enhancement offered by an Al_2O_3 dielectric is thus two-fold: (1) the increase in the dielectric constant correlates to an increase in oxide capacitance, thereby enhancing the response, and (2) the buffer capacity of the surface of aluminum films is higher, which leads to a higher surface potential shift for aluminum oxide devices.

We performed a side by side comparison of the silicon dioxide (100 Å gate dielectric) and the aluminum oxide devices (150 Å gate dielectric). The devices were optimized for back gate biasing conditions, and were placed into the Robinson buffer solutions of varying pH. At each pH, I_{DS} was measured as a function of V_{FG} for a constant V_{BG}. The threshold voltage for each curve was extracted using a constant current method. Results for three Al_2O_3 and three SiO_2 devices, all 50 nm in width and 30 nm thick, are shown in Figure 5.14. The observed average sensitivity of threshold voltage shift per pH is approximately 2 times higher for the Al_2O_3 devices when compared to the SiO_2 devices, which is slightly higher than reported comparisons for ISFET devices, around 1.3 [48]. This increase in sensitivity is observed despite the fact that the Al_2O_3 devices had a thicker gate dielectric which helps with robustness and reduction of leakage currents. In addition, the Al_2O_3 devices exhibit an average pH response (from pH 2.6 to 8.3) that is approximately 1.3 times higher than recent reports of the pH sensitivity of SiO_2 devices using a

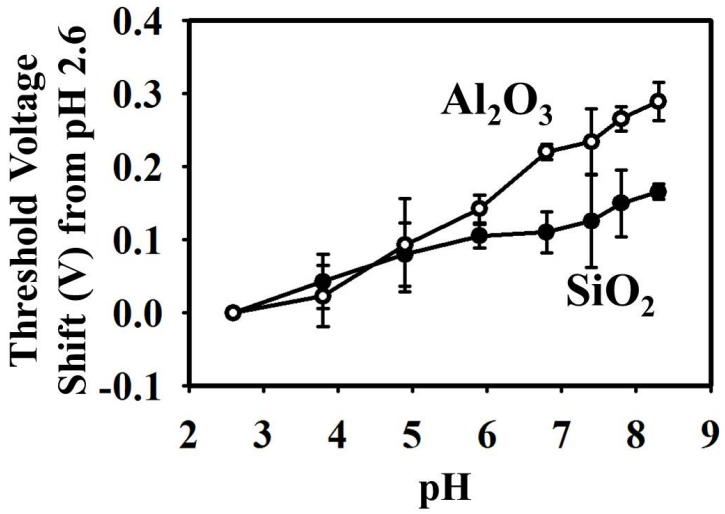

Figure 5.14: Experimental comparison of pH-induced threshold changes using three Al_2O_3 NWFET devices and three SiO_2 devices. The Al_2O_3 devices demonstrate a higher sensitivity to pH, which is expected based on the difference in buffer capacities of the surfaces. Error bars were calculated using the standard deviation of the threshold voltage shifts of the three devices used in the study.

similar back gate structure [132]. The error bars in Figure 5.14 were obtained as an average of the results of three different devices, and are due mostly to device to device variation. Individual devices showed high repeatability of less than 10 mV variation in threshold voltage for five sweeps.

5.10 Effect of Device Width on pH Sensing

The Al_2O_3 devices were next used to investigate the effect of device width on sensitivity of pH detection, with and without back gate optimization. We found that for devices with a physical thickness of 30 nm, the devices showed very similar responses to changes in pH for a range of widths varying from 50 nm (nanowires) up to 2 m (nanoplates). This is explained conceptually in Figure 5.15. When the thickness of the devices is much larger than the silicon Debye length (top) as previously reported [104], changes in charge at the surface affect a much larger percentage of the cross-section of the device channel for a wire configuration (left) as compared to a plate (right), thus re-

sulting in higher responses for the wire as compared to the plate. This is due primarily to the exposure of the sidewalls of a nanowire device, which allow for more of the channel charge to be modulated by the sidewall. However, for our devices, after back gate optimization, the effective electrical channel thickness is much smaller than or on the same order as the silicon Debye length (Figure 5.15, bottom). Changes in charge at the top surface affect the entire channel regardless of whether a nanowire or a nanoplate is used to measure response. In this case, very little dependence of sensitivity or response is expected on device width. This trend was observed experimentally for Al_2O_3 devices, by flowing Robinson buffers of different pH values over 50 nm, 200 nm, 400 nm, 1 m, and 2 μm wide devices patterned on the same chip in close proximity. With the optimization of back gate bias conditions, we saw very little relationship between device width and the measured average pH response (Figure 5.16, top), with a maximum deviation of less than 15% for all the device widths measured. However, when the back gate was left floating (making the device electrical thickness on the order of the physical thickness), a slight improvement in average pH response of around 300% could be seen when decreasing the device width from a 2 μm plate to a 50 nm wire (Figure 5.16, bottom). These results lend evidence to the claim that the primary concern for increasing pH sensitivity is maintaining a device electrical thickness that is much smaller than the silicon Debye length. Decreasing device width beneath the lithographical limit often results in increased cost and complexity of processing and may be unnecessary if proper biasing schemes are applied, in the case of pH sensing.

5.11 Conclusions

In summary, we have explored critical parameters that could be used to optimize the sensing of pH changes by field-effect sensors. We have demonstrated a top-down fabrication process that incorporates a new dielectric material, Al_2O_3, suggesting the possibility that a wide variety of other high k-dielectrics can also be utilized in nanowire field-effect sensors. The use of high-k dielectric materials improves both sensitivity and robustness by allowing for the use of a thicker gate dielectric, which reduces gate leakage issues in fluid. Both the Al_2O_3 and SiO_2 devices showed normal stable transistor

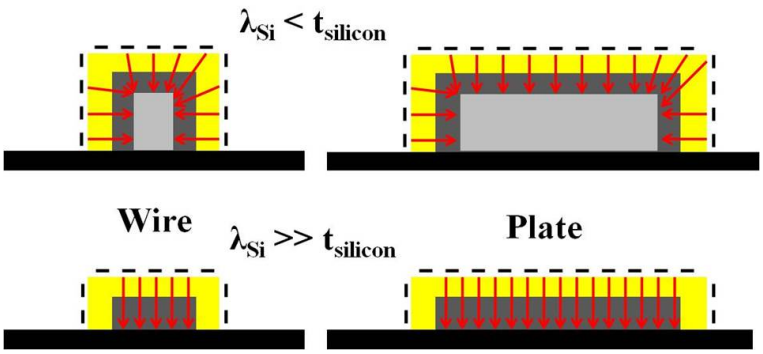

Figure 5.15: Schematic illustrating two separate cases: when the silicon Debye length is much less than the silicon thickness (top) and when the Debye length is much greater (bottom). A large difference in the % of the channel that can sense charge at the dielectric/fluid interface is noted for nanowire vs. nanoplate in the top case, whereas no difference is seen in the bottom case.

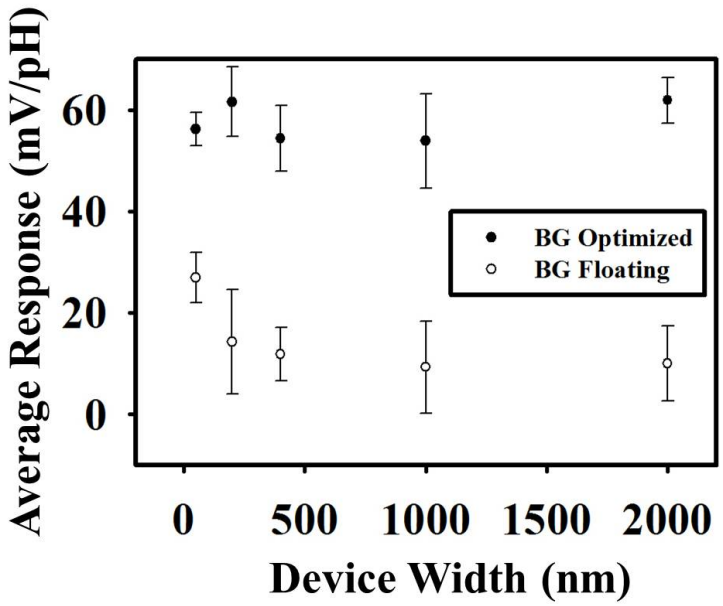

Figure 5.16: Average pH response (calculated by fitting a line to eight pH points) as a function of device width (50 nm, 200 nm, 400 nm, 1 m, and 2 μm wide devices) in an experiment with both optimized back gate biases (top) and with the back gate left floating (bottom). The response is seen to be virtually independent of device width when the back gate is optimized, but a slight increase in response is seen when reducing device width in the case of the floating back gate. Error bars were calculated with three separate devices in each case.

operation. By applying a potential to the back gate we were able to thin the effective electrical thickness of the devices to a few nanometers, which dramatically increases the response of the devices. The Al_2O_3 devices outperformed their counterpart SiO_2 devices by an average sensitivity improvement of 1.97. Lastly, an on-chip comparison of devices of varying width from the nanoscale to the microscale showed that when the effective device thickness is on the order of the silicon Debye length, response to changes in pH is relatively independent of device width.

Though these results demonstrate the advantages of using a high-k dielectric over a normal SiO_2 surface, there is still much room for improvement in the following areas:

- Device-to-device variation: The error bars shown in Figure 5.14 are due primarily to the variation in threshold voltage, device characteristics, and pH response of one device to another. These variations are induced mostly due to the lack of cleaniless and repeatability of machines in a university cleanroom. Methods to improve these non-idealities will be discussed in Chapter 6.

- Device noise: Average individual device noise for these devices was on the order of 10 mV or less. There is significant room for improvement. The devices discussed in Chapter 6 can have noise less than 1 mV.

- Minimum detectable pH resolution: As a result of the large noise, even if Nerntian response of 59 mV/pH was achieved, with a 3X noise ratio, the minimum detectable pH difference would be about 0.5, which is well above what even commercial sensors can easily detect (around 0.01 pH units). Future work with the HfO_2 dielectric devices will significantly improve on this important parameter.

Work in Chapter 6 will address most of these issues in addition to further increasing stability, pH response, and robustness in fluid with a HfO_2 gate dielectric.

CHAPTER 6

HAFNIUM OXIDE GATE DIELECTRIC FOR SENSITIVE PH AND SMALL NUCLEIC ACID OLIGOMER DETECTION

This chapter will discuss the fabrication of devices with a HfO_2 gate dielectric and their use for sensitive detection of pH changes and DNA analogues of important microRNA sequences.

6.1 Introduction

Point-of-care (POC) diagnostics has emerged as an exciting field where devices can provide rapid, cheap, and accurate results in a portable fashion. Such diagnostic devices have the potential to provide critical patient information more rapidly than instruments in centralized lab facilities at cheaper costs, reducing the turnaround time for results in critical care situations [136, 137]. Moreover, POC diagnostics can present patients with more control of their own therapy [138], leading to greater patient satisfaction and improved clinical outcome. In particular, treatment for various forms of cancer could highly benefit from such POC devices. As our knowledge of cancer pathways rapidly grows, important indicators of cancer have been revealed, including changes in the genome, exome, transcriptome, and expression levels of several cancer biomarkers such as proteins and microRNA (miRNA). Devices that could rapidly detect cancer biomarkers in a rapid, accurate, multiplexed, and cost-efficient fashion would revolutionize cancer treatment, allowing for better evaluation of the efficacy of treatment, earlier detection of cancer, and de-convolution of the complex pathways that result in cancer.

Adaption of the ubiquitous field-effect transistor (FET) technology has been proposed as a possible core technology for the sensing component of POC devices, due to the potential for low per unit cost, label-free detection, and amenability for scale-up and integration with signal processing electronics. Electrochemical methodologies based upon ion selective field-effect tran-

sistors (ISFETs) have been well studied over the last 40 years, including use as biosensors (bioFET) [139–142]. ISFET and bioFET performance is based upon the charge of a binding biological analyte over the gate insulator of the FET, which induces changes in the source-drain current of the device. This allows for label-free, ultrasensitive, and rapid detection of relevant biological analytes. Labeling can be very heterogeneous as well as detrimental to target-analyte interactions, reducing the sensitivity and accuracy of the measurement.

Silicon nanowire FET devices (SiNWFETs), where the silicon channel has thicknesses and diameters in the tens of nanometers or less, have further enhanced properties. Using SiNWFETs, researchers have demonstrated detection of biological analytes such as proteins [74, 77, 79, 80, 95, 97], DNA [39, 45, 76, 143], RNA [93], ions [144], and other small molecules [145] down to fM concentrations. The increased sensitivity of these devices is mainly attributed to the increased gate control of the silicon channel due to a higher surface area to volume ratio. Thus, silicon nanowires show promise in cancer diagnosis, since various cancer biomarkers may exist in small concentrations throughout the disease pathogenesis. Silicon nanowire FETs fabricated with top-down techniques [76, 146–149] are particularly attractive, due to CMOS compatibility and high amenability for scale-up. However, though nanowire technology has existed for over a decade, several issues have prevented the technology from maturation into fully fledged POC products. Various issues have arisen regarding device stability in fluid such as measurement drift [150], leakage paths through the sensing dielectric, high signal noise [151], and lack of repeatability. Silicon oxide, the traditional top gate dielectric, is one of the main culprits behind several of these issues, due to its relatively low dielectric constant, low pH buffering capacity, and susceptibility of gradual charge incorporation by ion diffusion when exposed to fluid [152, 153]. To circumvent some of these issues, researchers have turned to high-k materials, including aluminum oxide (Al_2O_3), hafnium oxide (HfO_2), and tantalum oxide (Ta_2O_5). High-k materials enable high gate oxide capacitance values even with physically thicker gate oxides, allowing a reduction in leakage current. HfO_2 has arisen as a particularly promising dielectric for ISFETs and MOSFETs due to its stability on silicon and its acceptable bandgap and conduction band offset values. It can be deposited by chemical vapor deposition and yields improved pH sensitivity. [130] To date, very little work

has demonstrated characterization and application of hafnium oxide layers for biosensing using FETs. Annealing of HfO_2 has been shown to improve pH sensitivity in a two-terminal EIS (electrolyte-insulator-semiconductor) capacitor using capacitance-voltage curves [154]. However, such a structure does not take advantage of the main desirable property for a FET, its intrinsic high current gain (high transconductance). In addition, HfO_2 deposited at high CVD temperatures for ISFETs leads to leakage paths in the silicon in high aspect ratio areas and results in higher roughness [155], which is undesirable for a charge based biosensor. The demonstrated sensitivity for this structure was very low (biotin and streptavidin detected down to 50 μg/mL). pH sensing has been demonstrated with a FET structure with encouraging near-Nernstian results, but no molecular sensing has been reported to date.

Here we describe a process for fabricating robust HfO_2 based silicon nanoFET sensors for biological applications. We use atomic layer deposition (ALD) to form the hafnium oxide dielectric and a wet etch based process for releasing the device structures. Unlike CVD methodologies, ALD is more conformal and can be performed at lower deposition temperatures with better process control. Additionally, the wet etch based process for device release eliminates the possibility of RIE induced damage to the delicate dielectric layer. We have characterized in detail the properties of this low temperature deposition process and optimized subsequent annealing conditions to create a high quality dielectric. Moreover, we discuss the electrical and chemical advantages of the process, which include HfO_2 becoming an excellent wet etch stop for acid, alkali, and oxidizing chemistries. By thoroughly characterizing the HfO_2-silicon interface, we were able to produce a high quality gate dielectric layer, resulting in a device with high repeatability and low hysteresis in fluid. The devices are highly stable and robust, and show minimal drift over hours in fluid. As a result, we were able to achieve $\approx$56mV/pH unit response for nanowire devices. We then demonstrate the sensitive detection of a DNA analogue sequence of microRNA, which can be highly important cancer biomarkers. MicroRNAs (miRNAs) are small RNA oligonucleotides which bind to messenger RNAs, causing translational repression of proteins and gene silencing. In this work, we focus on sensing DNA analogues of miRNAs, which we call microDNAs (miDNA). The miRNA templates we focus on, miR-10b and miR-21, are commonly upregulated in breast cancer [156–160]. Moreover, miR-21 is found in a 4-fold higher concentration

than miR-10b in normal tissue [161], making miR-10b a harder analyte to detect even when upregulated. The devices were functionalized with different molecular weight poly-lysine strands and DNA probes specific to the miR-10b miDNA sequence. Different sensitivities for the different molecular weight poly-lysines were achieved for miR-10b, with lower sensitivity being achieved on the higher molecular weight polymer. Analysis of the layers showed lower probe density and higher roughness for the higher molecular weight layer of poly-l-lysine. The devices were able to achieve 100fM detection limits for the mir-10b miDNA in comparison against a mir-21 non-complementary target, with a theoretical limit of detection of 1fM.

6.2 Materials and Methods

6.2.1 Materials

All metals for e-beam evaporation were of 99.999% purity and purchased from Lesker Co. DNA and miDNA strands were purchased from Integrated DNA Technologies and purified using HPLC. Poly-l-lysine (PLL) of MW 9,000-14,000 and MW 70,000-150,000 were purchased from Sigma in powder form and used without further purification. Robinson buffer solutions composed of 1mM acetic acid, 1mM phosphoric acid, and 1mM boric acid were titrated with NaOH/HCl from pHs 4-12. All buffer components were purchased from Fisher Scientific. A leak-free Ag/AgCl reference electrode was used to apply bias to the fluid on top of the devices and was purchased from Warner Instruments.

6.2.2 Device Fabrication

The detailed process flow was very similar to that covered in Chapter 3. The fabrication flow began with bonded Silicon-on-Insulator (SOI) wafers, doped p-type at $10^{15}/\text{cm}^2$ with a buried oxide thickness of 1,450 Å and top silicon thickness of 550 Å. The top silicon was thinned to approximately 300 Å by dry oxidation and stripping of the oxidized layer with 10:1 buffered oxide etch. The wires were then defined via electron beam lithography and wet etched with 25% TMAH to define the active silicon area. The source and

drain regions were doped with boron (simulated doping $10^{19}/cm^2$) by ion implantation, and annealed at 1000 °C for 5 minutes to active the dopants. The wafer was then dipped in 50:1 BOE for 20s to remove any native oxide, and an SC1/SC2 clean performed. The wafer then underwent a rapid thermal anneal at 1000 °C for 60s to help densify the native oxide layer. The HfO_2 gate dielectric was deposited by ALD at a temperature of 120 °C for 100 cycles. Following the gate dielectric formation, via holes were etched into the contact regions with 10:1 BOE, and a 100 Å Ni/50 Å TiN layer was deposited in the contact regions by RF sputtering. A rapid thermal anneal was performed at 500°C in Ar to form NiSi and reduce the contact resistance at the source and drain regions of the devices, while also densifying the HfO_2 and creating a wet etch stop. Next, 150nm of Al was sputtered and patterned over the contact areas. A 450 °C furnace anneal in Ar/H2 was performed for 30 min to anneal the contacts and remove interface traps in the oxide. Afterwards, a 5,000 Å thick passivation layer of PECVD SiO_xN_y was deposited over the entire wafer. Metal pad areas on the outside of the Al leads were defined by optical lithography and 10:1 BOE was used to etch the passivation layer. Metal pads composed of 50nm Ti/ 300nm Ni/ 500nm Au were then deposited by e-beam evaporation. The final passivation layer etchback to release the HfO_2 devices was done using 10:1 BOE. Subsequently, the wafer is diced (American Precision Dicing) into chips of 1.5x1.5cm for testing.

6.2.3 Materials Characterization

For thickness characterization, HfO_2 of varying thicknesses was deposited by ALD onto polished Si wafers and annealed according to the device fabrication above. The wafer was then covered with photoresist and diced into 1x1cm dies. Ellipsometry measurements were taken using a Rudolph FEIII ellipsometer at a wavelength of 632.8nm and an angle of 70 degrees. Each measurement was taken over ten different areas of a chip and averaged together to get a thickness and standard deviation. For fluorescence measurements, a 1 μm thick thermal oxide was grown on a polished Si and then 100 cycles ALD HfO_2 deposited on top. The thick grown oxide was to limit signal degradation due to fluorescence interference contrast (FLIC) [162]. The HfO_2

was subsequently annealed according to the device fabrication above. Fluorescent images were taken with a Nikon microscope at an exposure of 800ms and a gain of 1.3x. Atomic force microscopy images of the HfO_2 and PLL layers were taken with an Asylum Cypher AFM using a Force Modulation AFM probe tip (Budget Sensors) with a resonant frequency of 75kHz and a force constant of 1-3 N/m. Force applied to the substrates during contact mode was calibrated by taking the inverse optical lever sensitivity (invOLS) of the cantilever deflection on a bare HfO_2 surface and calculating the spring constant of the cantilever by fitting the thermal fluctuations. X-ray photoelectron spectroscopy of the HfO_2, DNA, and PLL layers were taken with a KRATOS Axis Ultra XPS at a take-off angle of 90 degrees. Survey spectra were acquired at a pass energy of 160eV with 2 sweeps collected. High resolution spectra of Hf 4f, P2p, O1s, C1s, and N1s peaks were collected at a pass energy of 40eV with a total of 25 passes per peak.

6.2.4 Electrical Measurements

High frequency C-V measurements of HfO_2 MOS capacitors were performed at 1MHz using a Keithley semiconductor parameter analyzer (Keithley 4200) and corrected for series resistance. The capacitors had a top contact of 30nm TiN/100nm Al, and a back contact of 100nm Al, which were DC sputtered. Electrical current measurements and applied biases were controlled by the Keithley 4200 as well. Fluid gate biases were applied with a leak free Ag/AgCl reference electrode (Warner Instruments) that made contact to the solution. Back gate biases were applied using the conductive platform of the probing station which made contact to the backside of the FET dies. At any other times, the conductive platform served as the ground for the FET dies while biases were applied to the fluid gate electrode. The Robinson buffer pH solutions were made using 1 mM acetic, 1 mM phosphoric, and 1 mM boric acid with titrated HCl/NaOH to obtain the desired pH. All pH solutions were measured at the conclusion of the experiment to ensure that the pH had not changed significantly during the course of the experiment.

6.2.5 Preparation of Devices for DNA Sensing

Before depositing poly-l-lysine, chips were degreased with acetone and methanol, then rinsed in DI water for 1min. The chips then underwent an O_2 plasma etch at 500mTorr and 200W for 5 mins. Poly-l-lysine solutions were made to 0.2mg/mL concentration in 5mM $Na_2B_4O_7$, pH 8.5. Chips are soaked in PLL solution for 2 hours, then taken out of the solution and rinsed in DI water for 1 min. Chips are then blown dry with N2 and dessicated for 10min. The chips are baked at 85 °C in a vacuum oven for 4 hours afterwards.

DNA probe and targets were obtained from Integrated DNA Technologies and diluted to a stock concentration of 100μM in DI water. All stock solutions were stored at -20 °C until used. DNA probe solution (10 μM in 3X SSC buffer) was spotted on the device in a 10μL volume and allowed to sit for 2 hours in a humidity chamber. The chip was then rinsed in 2X SSC, 0.2X SSC, and 5% EtOH for 1 min each, and blown dry with N2. To crosslink the DNA to the PLL, chips were baked at 85 °C for 2 hours in a convection oven. A PDMS well with an adhesive bottom tape was attached to the chip afterwards. Each well had a circular diameter of 5mm and a fluid volume of 50μL. The target solutions for varying concentrations of miR-10b and miR-21 were made in 2X SSC buffer and put in the PDMS well for 30 mins to hybridize. The target was then rinsed off 3 times in 2X SSC buffer and 3 times in 0.2X SSC buffer before measuring in 0.02X SSC buffer.

6.3 Results and Discussion

One of the most important components of any silicon based FET is the gate dielectric and its interface with silicon. We chose HfO_2 because it currently satisfies the requirements demanded for CMOS integration. Atomic layer deposition was chosen as the method for forming the gate dielectric because of its self-limiting growth process, meaning the thickness is controlled by the number of deposition cycles, allowing accurate thickness control and uniform step coverage. Moreover, due the reactive nature of the precursors, the temperature window for deposition is wide. However, the electrical and chemical properties of the film are temperature dependent as well. Before using HfO_2 as our gate dielectric we characterized the properties of the hafnium oxide layer as deposited and how the thermal treatments taken during our process

affect the gate dielectric.

During our nanowire process, the hafnium oxide must be susceptible to hydrofluoric acid wet etching in order to create the contact vias over the source-drain regions of the FET. The concentration of HF also must be gentle enough to not deteriorate the photoresist, leading us to use a 10:1 BOE as the reagent. During the course of characterization, we observed that ALD deposition temperatures higher than 200 °C resulted in a layer which would not etch in BOE solution. Layers deposited at less than 80 °C etched very quickly and had deposition rates much larger than the limiting rate of ≈1Å/cycle. In our process we use a temperature of 120 °C, which gave us a good compromise between etching rate and deposition rate.

The characterization of the deposition thickness vs. number of cycles was done using ellipsometry and is shown in Figure 6.1A. Here we assumed a simple bilayer stack of HfO_2 and Si, with refractive indices taken from the Sopra Material Library. By depositing ALD films between 10 and 90 cycles and measuring the thickness we were able to verify the deposition rate per cycle and estimate the interfacial oxide thickness. The overall thickness (T) of the film on silicon is related to the HfO_2 deposition cycle number ($NHfO_2$) by:

$$T(nm) = R_{dep} N_{HfO2} + t_{SiO2} \tag{6.1}$$

where R_{dep} is the deposition rate and t_{SiO2} the native oxide thickness. By fitting a line to the data in Figure 6.1A we get a deposition rate of 1.23 Å per cycle and, if we extrapolate back to zero cycles, a native oxide thickness of 9 Å. These results are within range of the reported growth rates of HfO_2 [163, 164] and thickness of a chemically grown native oxide [165].

After ALD of the hafnium oxide films, we investigated how annealing would affect the chemical and electrical properties of the gate dielectric. Annealing of the films is an important parameter in optimizing the electrical performance of the gate dielectric. HfO_2 begins to crystallize at temperatures over 500 °C, and the crystallization temperature is thickness dependent, increasing with decreasing thickness [166]. Crystallization, although increasing the dielectric constant, is known to increase the leakage current through grain boundaries in MOS structures as well. Thus, leakage would be amplified even more in an aqueous setting where ions are even more mobile than with

a top metal. During our process we decided to keep our anneal steps below 500 °C in order to avoid excess leakage affects. First, we perform a rapid thermal process in Ar at 500 °C for 60s to densify the gate dielectric. Then, after the deposition of the leads, we do a forming gas anneal (Ar/10%H2) at 475 °C for 30 minutes to passivate interface traps and anneal the leads. This constitutes our basic annealing procedure on the gate dielectric.

To examine how the anneal steps affected the gate dielectric chemically, we subjected the annealed and unannealed films to various strong acid etchants such as acid piranha and SC2, as well as in 10:1 BOE. The etch rates for hafnium oxide annealed vs. unannealed are presented in Figure 6.1B. The films deposited at 120 °C show etch susceptibility for all the etching solutions. Etch rates of 15-40 Å per minute are achieved with the various etching parameters. After the rapid thermal anneal and forming gas treatments, the hafnium oxide becomes chemically inert. The ellipsometric thickness of the films only changes by about 5 Å for each of the etchants. We attribute the thickness change to a thin carbonaceous layer on top of the film which is subsequently removed during exposure to the etching solutions.

In order to determine how the annealing affects the system electrically, MOS capacitors were formed by sputtering 30nm TiN, then 100nm Al, on the HfO_2, and 100nm Al on the back of p-type silicon contact to create a capacitor with a structure shown in Figure 6.1D. High frequency capacitance-voltage curves were taken for as-deposited, RTP only, and RTP+forming gas HfO_2 substrates. The results for a 100 cycle ALD HfO_2 film are shown in Figure 6.1C. Each device was swept ten times to give insight into its stability. Using the high frequency capacitance, we can extract parameters such as the oxide thickness, dielectric constant, effective charge, and flatband voltage. For a p-type MOS-C, the accumulation region of the C-V curve is observed when negative voltages are applied to the gate. The oxide capacitance (C_{ox}) is the high frequency capacitance when the device is biased for strong accumulation. If we assume the oxide is one entity, the MOS-C acts like a single parallel-plate capacitor and C_{ox} is related to the total oxide thickness (t_{ox}) by:

$$C_{ox} = \frac{\epsilon_0 K_{eff} A}{t_{ox}} \tag{6.2}$$

where ϵ_0 is the permittivity of free space, A the capacitor area, and K_{eff} the relative dielectric constant. From Figure 6.1C, we can see that C_{ox} increases

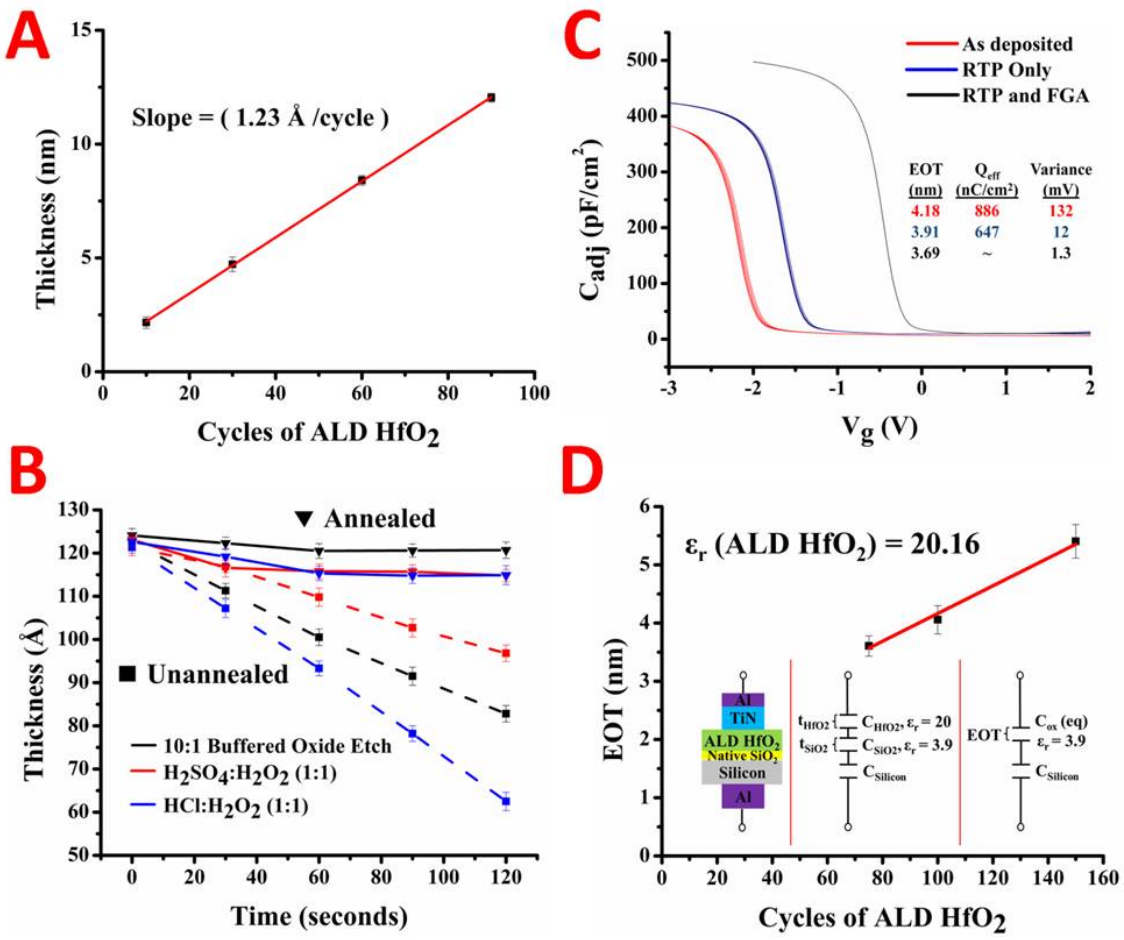

Figure 6.1: Characterization of the HfO_2 gate dielectric deposited by atomic layer deposition. The thickness of HfO_2 versus the amount of ALD cycles is shown in (A) with the slope inset. The effect of annealing the HfO_2 against chemical etchants is shown in (B) with the ellipsometric thickness versus etching time. High frequency capacitance-voltage curves for varying steps in the annealing procedure are in (C) with extracted values inset. The equivalent oxide thickness extracted from the C-V analysis versus the ALD cycle amount is plotted in (D) with the extracted dielectric constant inset.

as we perform the annealing procedures, indicating that K_{eff} is increasing and thus producing a higher quality HfO_2 layer. As we anneal the samples, we also notice the flatband voltage of the MOSCaps shifts to more positive potentials and the drift (or variance) becomes minimized for the RTP and forming gas system. The flatband voltage (V_{fb}) for MOSCaps can be expressed as:

$$V_{fb} = \phi_{MS} - \frac{Q_{eff}}{C_{ox}} \tag{6.3}$$

where ϕ_{MS} is the work function difference between the metal and the semiconductor and Q_{eff} is the effective oxide charge density. The Q_{eff} is also the sum of the oxide fixed charge(Q_F), oxide mobile charge (Q_M), and oxide trapped charge (Q_{OT}) with $Q_{eff} = Q_F + Q_M + Q_{OT}$. We extract the flatband voltage from the flatband capacitance by interpolating between the closest voltages around the flatband capacitance value. We then extract the variance and Q_{eff} for each MOSCap under study from the flatband voltages for each curve. The Q_{eff} and variances for each anneal are found in the inset in Figure 6.1C. By annealing the substrates we eliminate most of the effective charge and variance in the system. This is probably due to the removal of dangling bonds in the oxides and passivation of interface traps at the HfO_2-SiO2 and SiO_2-Si interfaces [167]. To determine the dielectric constant of the annealed HfO_2, different cycles amounts of HfO_2 were deposited and C_{ox} determined. If we assume the dielectric is composed entirely of SiO_2 (since the dielectric constant is known) we can replace the K_{eff} in Equation 6.2 with the dielectric constant of SiO_2 (3.9) and extract an equivalent oxide thickness (EOT) for the layer. An example of this is found in the inset of Figure 6.1D, along with the stack for the MOS capacitors. The EOT of the HfO_2 MOSCaps was plotted versus the ALD cycle number (N) and is shown in Figure 6.1D. The EOT is a combination of the HfO_2 thickness and dielectric constant with the interfacial oxide thickness and dielectric constant. It can be expressed in a linear form by:

$$EOT(N) = \frac{3.9}{K} R_{dep} N + t_{sio2} \tag{6.4}$$

The dielectric constant can be extracted from the slope of the line $(3.9/K)R_{dep}$ assuming the deposition rate is known, which we extracted from ellipsometry. The interfacial oxide thickness is equivalent to the y-intercept of the

line, or by extrapolating the fit back to zero cycles. By fitting the points in Figure 6.1D we determine a dielectric constant of 20.1 for the deposited ALD film, which meets expectations for a high-quality ALD HfO_2 film [168]. The extrapolated interfacial oxide thickness is ≈17 Å which agrees well with literature [169]. This value is substantially higher than the extracted value from ellipsometry of ≈9 Å. We attribute this to the high diffusivity of oxygen in HfO_2, which commonly increases the interfacial oxide thickness during anneals [170, 171].

Top-down and cross-section images of the nanowires and nanoplates are shown in Figure 6.2A. Part 1 of Figure 6.2A shows an overall top-down image of the nanowires. The release window is in the center, indicated by the yellow arrows, while the metal leads connecting to the nanowires are indicated by a green arrow. A high magnification image of the nanowires in (1) is shown in Figure 6.2A(2). The brighter areas represent the nanowires as silicon lies below the beam, increasing the secondary electron emission. The nanowires appear to be ≈150nm in width from the top-down image in (2), but the cross section in (3) shows them to be ≈100nm wide. The cross section in (3) shows the trapezoidal nature of the nanowires from the TMAH anisotropic etch, as well as the surrounding HfO_2 gate dielectric. The thickness of the HfO_2 is approximately 13nm from the image, although hard to measure precisely due to the grain size of the metal sputtering. This amount agrees well with the thickness information we obtained from Figure 6.1. A top down image for a nanoplate inside the release window is in (4), and shows a nanoplate of ≈2μm width.

A schematic showing the full cross section of a nanowire and the setup for device testing is in Figure 6.2B. For fluid testing, a leak free Ag/AgCl reference electrode is biased and swept, with a constant source-drain bias applied. The back of the handle wafer is grounded, and the $I_d - V_g$ transfer curve is measured.

The stability of the device under operation in 0.02X SSC buffer is shown in Figure 6.3. $I_d - V_g$ curves were swept from positive to negative bias with the Ag/AgCl electrode and cycled 5 times, shown in Figure 6.3A. The subthreshold slope extracted for the device is 112mV/decade, comparatively on the low end for nanowire devices in fluid testing. The standard deviation for threshold voltage on the devices is 2.7mV. The combination of a low standard deviation and a low subthreshold slope indicates the combination of a

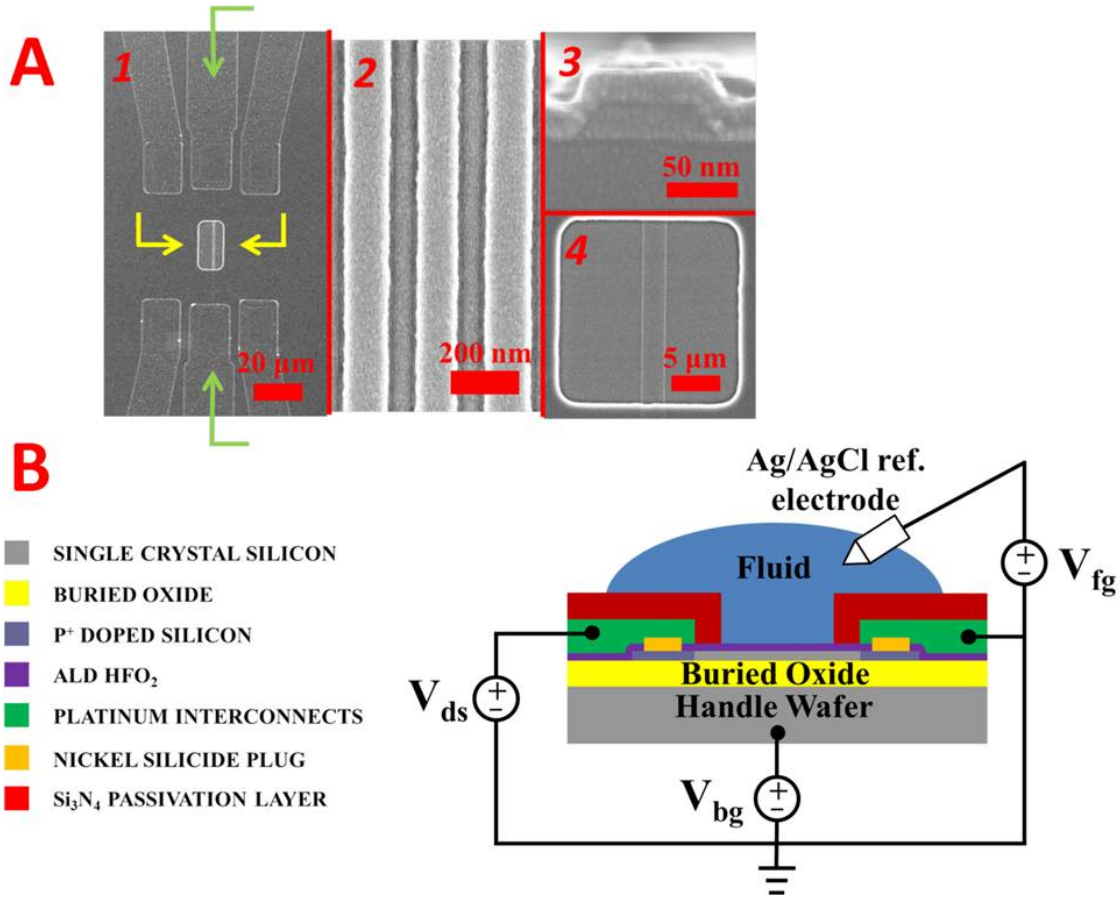

Figure 6.2: Scanning electron micrographs of the silicon nanowires are in (A). Image 1 shows an overview of the nanowire sensing area, with the source-drain metal leads (green arrows) and release window (yellow arrows) highlighted. A high magnification top-down image of the nanwires is shown in 2. A cross-sectional image of a nanowire is in 3 while a top down image of a nanoplate is in 4. A horizontal cross sectional schematic of sensing setup is represented in (B). The relevant structures are color coded to the left, with an example electrical measurement setup for the source drain (V_{ds}), fluid gate (V_{fg}), and back gate (V_{bg}).

high stability device and low drift reference electrode in electrolytic solutions. Moreover, the fluid is exposed to a ≈0.2 cm^2 area on the chip, which if not passivated properly would cause leakage current much higher than the measured device current. The leakage throughout this area ranged from 300pA to 1nA, or 1.5 nA/cm^2 to $5nA/cm^2$. An example of long term device stability in 0.02X SSC buffer is shown in Figure 6.3B. The threshold voltage after each sweep and the time was recorded and repeated over an hour. The change in threshold voltage over time decreases rapidly for the first 10 minutes, then stabilizes. The overall change is 65 mV/hour, with only 10mV change happening after the first 10 minutes. The standard deviation of the device over 5 sweeps surrounding each time point was also plotted. Briefly, the standard deviation for sweep 15 would include points from sweep 13-17. The standard deviation shows a ≈1mV standard deviation per 5 sweeps over the period of the hour. As the device equilibrates, the standard deviation between sweeps goes down. The leakage to the fluid gate is in Figure 6.3C, plotted over the course of an hour, and stays relatively stable near 800pA, indicating little degradation to the HfO_2 dielectric or passivation layer over that time period.

The response and stability of the devices to changes in pH was demonstrated using Robinson buffers for the nanowires and nanoplates. The changes in pH will cause a change in the surface potential on the device due to the proton reactive groups on top of the HfO_2 surface. Robinson buffer solutions ranging from pHs of 4.3-10.5 were used and the threshold voltages of nanowires and nanoplates extracted from the Id-Vg curves. The change in the surface potential with respect to the pH 7.4 solution, set at zero, was plotted vs. pH for 3 nanowires and 3 nanoplates, and is shown in Figure 6.4. We achieve a 55.8 mV/pH sensitivity for the nanowires and 51.0 mV sensitivity for the nanoplates, with the Nernstian limit being 59mV/pH. The sensitivity of nanowires being higher than bulk devices agrees well with literature without optimization of the backgate, as does the range of pH sensitivities found for the HfO_2 sensing dielectric.

The sensing of miDNA was done with different molecular weight PLL functionalizations using the same probe molecule. The procedure for modifying the surface is explained in detail in the Experimental section, but outlined in Figure 6.5A. Briefly, the poly-l-lysine is electrostatically adsorbed onto the HfO_2 surface and baked on a hotplate at 85 °C to ensure a good linkage. Then, the ssDNA probe is electrostatically bound to the HfO_2 surface and

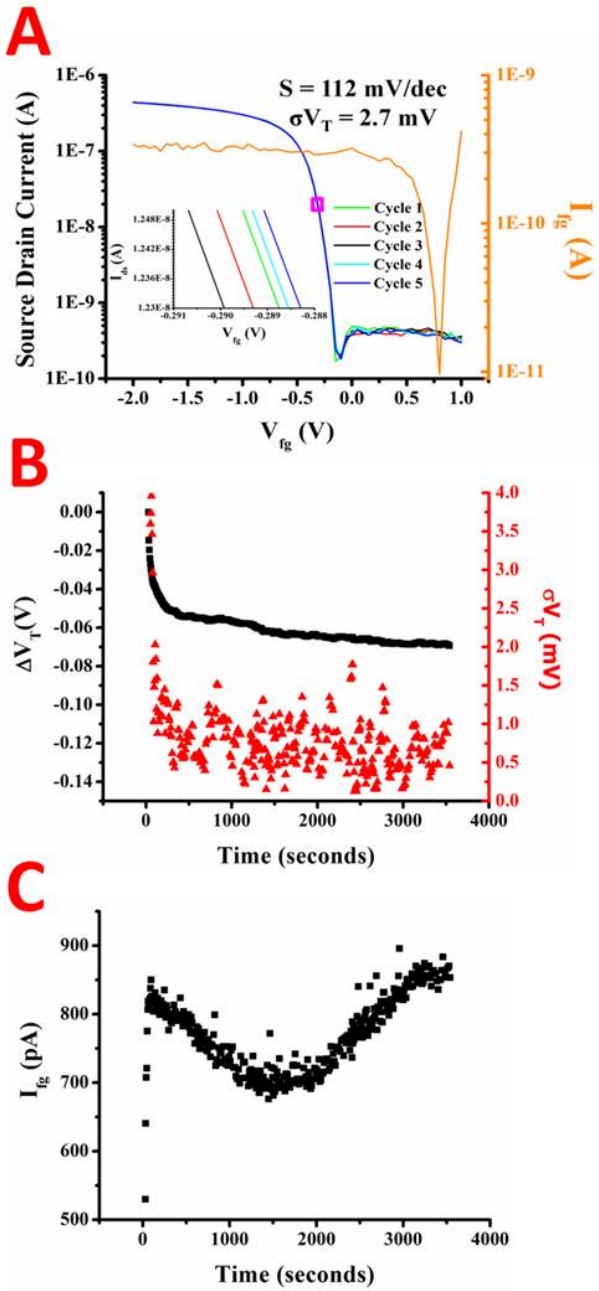

Figure 6.3: Representative source-drain current verse fluid gate voltage for a nanowire is shown in A. The nanowires were swept for 5 cycles with the fluid gate leakage also measure (right side of graph) and an enlarged view of the curve repeatability is inset in A. The change in the threshold voltage (left side) and standard deviation in threshold (right side) versus time for a nanowire is in B. The change in the current through the fluid gate versus time for a nanowire is in C.

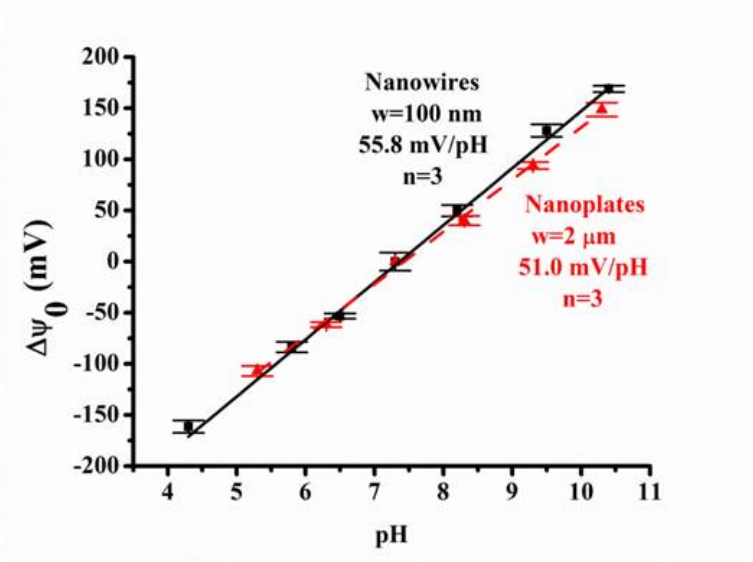

Figure 6.4: The change in surface potential of the HfO_2 sensing dielectric versus solution pH for nanowires (black) and nanoplates (red). The pH sensitivity for nanowires and nanoplates was extracted through linear regression and is displayed inset.

the excess is rinsed off. The ssDNA probe is then baked, which covalently links part of the sugar and phosphate backbone to the poly-l-lysine through free radical generation. The miDNA target is then hybridized with the probe and sensed on the device. Poly-l-lysine was chosen since it can be deposited from aqueous solution and electrostatically bound to both the HfO_2 and phosphate backbone of probe DNA. This allows for the probe DNA, and binding target, to be in a horizontal conformation [172]. As opposed to a vertical conformation, a horizontal conformation allows for charge density to be closer to the surface, thus creating a larger shift in the surface potential. A horizontal conformation allows for more charge to influence the channel at a certain Debye length of electrolyte solution.

The sensitivities for the devices with different molecular weight poly-l-lysines are quite different, which we discuss in Figure 6.7. A lower sensitivity would occur if the overall effective charge density during binding is less, or the charges were farther removed from the surface. A few possibilities which would lead to this are the morphology of the poly-lysine layers as well as the probe density. Thus, we characterized the poly-lysine layers and probe attachment to understand the underlying reasons for this discrepancy.

Table 6.1: Characterizion of the thickness, roughness, and probe density of the HfO_2 surface functionalization process.

	Ellipsometric Thickness (Å)	AFM Thickness (Å)	Roughness (Å)	XPS P 2p Peak Area
HfO_2 layer	120.1 ± 3.2	–	1.1	–
PLL 9-14K	11.3 ± 1.5	11.2	1.6	–
PLL 70-150K	12.1 ± 2.1	9.8	3.4	–
ssDNA (PLL 9-14K)	21.6 ± 2.3	–	1.9	145.7
ssDNA (PLL 70-150K)	19.8 ± 2.7	–	2.9	74.2

We used a combination of ellipsometry, AFM, and XPS to look into the morphology, thickness, and probe densities (Table 6.1). When the PLL layers were deposited, the ellipsometric thicknesses came out to be within error of each other at ≈11Å each. This indicates the formation of a polylysine monolayer on the surface. The ssDNA probe attachment came out to be within error as well, at ≈20.5Å each, which leads us to believe the DNA rests in a horizontal configuration. The similar thicknesses for both indicate we should get similar sensitivity levels for miDNA detection.

Thus, we utilized atomic force microscopy (AFM) to characterize the morphology of the 100 cycle ALD HfO_2 layer and the PLL layers. The tapping mode images in Figure 6.5B are numbered 1-3 in the image set for the untreated HfO_2, PLL (9-14k), and PLL (70-150k), respectively. The images for the untreated HfO_2 and PLL (9-14k) indicate very smooth and uniform layers. The roughness values extracted for the HfO_2 and PLL (9-14k) are 1.1 and 1.6Å RMS, respectively. The morphology of the PLL (70-150k) is much rougher and has a porous, spongelike appearance. These pores, represented by the darker spotted areas in the image, appear to be the thickness of the monolayer or close to it. Moreover, we were able to determine the thickness of the films by applying a 50nN force to the tip in contact mode and scratching away the PLL layers, then reimaging a larger area in tapping mode. A 50nN force is known to be more than enough to remove organic monolayers and silane layers, without damaging the underlying surface [173]. The images after a 50nN force are 4-6 in the image set. The untreated HfO_2 shows no changes in height, indicating a hard surface. The PLL layers show distinct changes in thickness, indicated by the square scratched area visualized in images 5 and 6. Taking a section analysis across the scratched areas gives

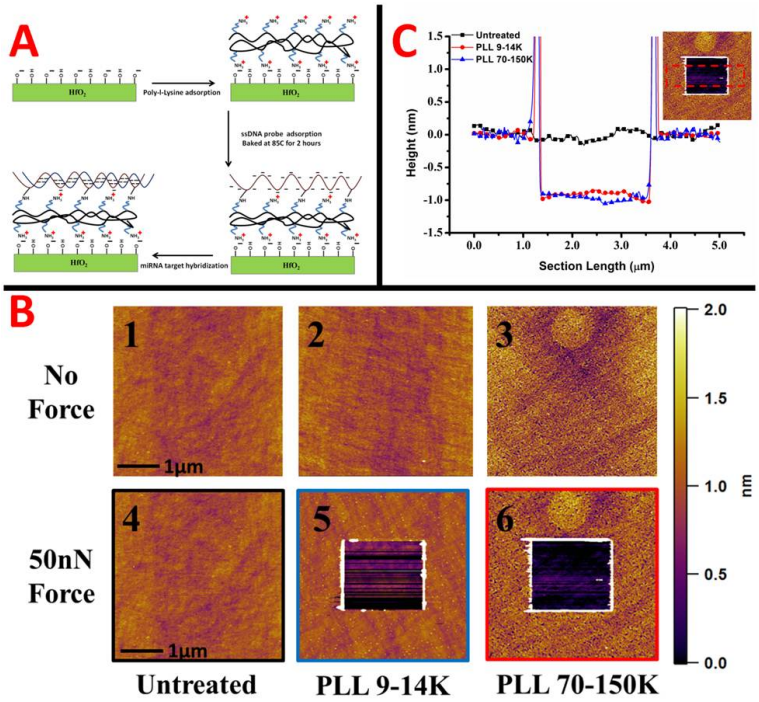

Figure 6.5: A schematic of the surface functionalization of the HfO_2 surface for microDNA sensing is shown in (A). AFM images of the HfO_2 and poly-l-lysine layers of different molecular weights are shown in (B). Tapping mode images with no force applied (upper) for the different layers, and after a 50nN scratching force (bottom) are displayed. The scale bar for all AFM images is on the right. A cross section for the images with 50nN force applied is in part C. The cross sections are color coded to images in B with an inset representing the cross sectional area.

us the thickness of the PLL films, and is shown in Figure 6.5C. The images 4-6 in 5B are color coded to match up with section analyses in Figure 6.5C. The section analyses showed a similar thickness for the PLL layers compared to ellipsometry and are in Table 6.1. However, the buildup of material on the side of the scratched away area was much greater for the lower molecular weight layer (data not shown). This indicates the amount of material for the higher molecular weight PLL on the substrate was less, leaning towards the evidence of a more porous and incomplete layer.

Attachment of the probe DNA to the PLL layers was measured using two techniques: (1) XPS for the P2p peak intensity from the DNA backbone and (2) fluorescence with a Texas Red labeled miR-10b probe. The XPS P2p signal intensity for the HfO_2 and probe DNA on the two PLL layers

is in Figure 6.6A. The peak for the ssDNA on PLL(9-14k) is much larger than the one on PLL (70-150k), indicating a higher probe density. The peak intensities are in Table 6.1, with a ratio of approximately 1.8:1 for the PLL(9-14k):PLL(70-150k). The fluorescently labeled micrographs of bare HfO_2 and PLL layers, both with and without probe are in Figure 6.6B. The quantification of the fluorescent intensity is in the bar graph in Figure 6.6C. Images 1 and 2 show the bare HfO_2 layer with and without the probe attachment procedure. The amount of background fluorescence for the HfO_2 with and without probe is about the same. Thus, DNA has very little non-specific adsorption to HfO_2, which should make for better selectivity and fewer issues with blocking. Images 3 and 4 show the background fluorescence for the PLL layers. The PLL (9-14k) layer shows slightly higher background, as to be expected since there are more optically active surface groups according to AFM. The images for the attachment of the miR-10b probe DNA show slightly greater than a two-fold intensity difference between the PLL layers, with PLL (9-14k) containing the higher probe density. This reaffirms the XPS results in Figure 6.6A, indicating the probe density is much higher on the lower molecular weight PLL layer.

The demonstration of sensing of miR-10b target on the HfO_2 silicon nanowires is in Figure 6.7, with the DNA probe and RNA target sequences in Table 6.2. To make sure the devices were being functionalized properly, $I_d - V_g$ curves at key steps during the probe attachment process were taken to examine the changes in threshold voltage (Figure 6.7A). First, a reference of the bare HfO_2 was taken in the .02X SSC sensing buffer. The deposition of PLL then shifts the threshold voltage to the left by $\approx$160mV. The direction of change is proper since the PLL is positively charged and the device operates in accumulation mode, thus creating a more negative threshold to compensate for the positive increase in surface potential. In contrast, when we adsorb the probe DNA we cause a shift in the opposite direction of $\approx$90mV relative to the PLL, which is also expected due to the negative charge density of the phosphate backbone.

After conjugating the ssDNA probe to the PLL surface, various concentrations of miR-10b target were allowed to interact with the sensor for 30 min, then were rinsed off and $I_d - V_g$ curves recorded in the .02X SSC sensing buffer. The threshold voltage change with varying RNA target concentrations was then measured relative to the ssDNA probe reference (shown

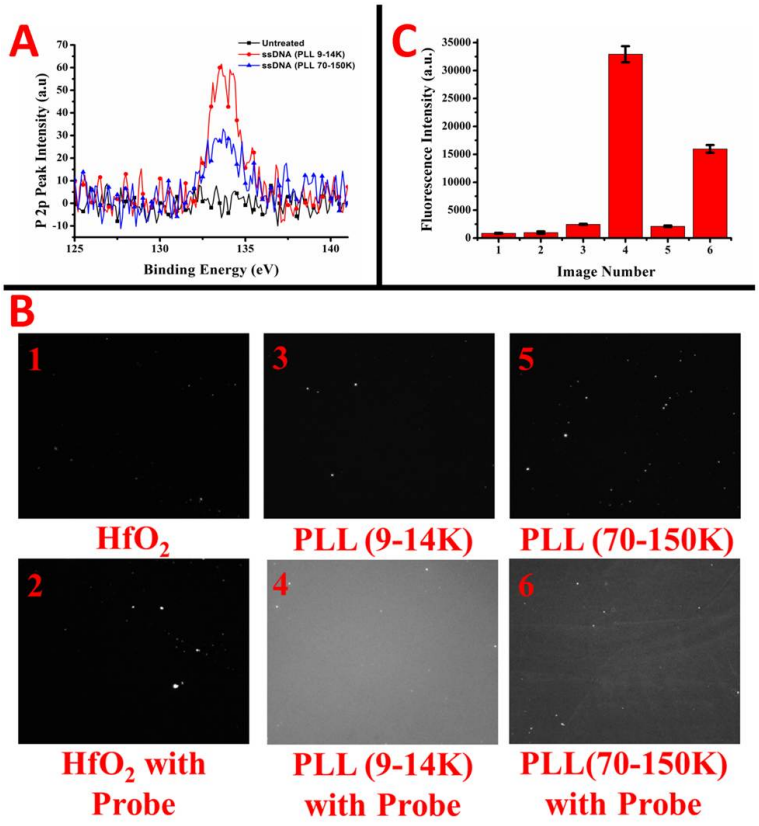

Figure 6.6: P2p peak intensities from XPS are shown in A for ssDNA adsorption onto the poly-l-lysine layers of different molecular weights, and onto the bare HfO_2 surface. Fluorescent micrographs of ssDNA probe immobilization are shown in B for HfO_2 and the different molecular weight poly-l-lysines, both with and without exposure to ssDNA probe. Fluorescent intensities for images 1-6 in B are plotted in column format in C.

Table 6.2: Nucleic acid sequences for the immobilized probe and miDNA targets

	Sequence
DNA probe	5'-CACAAATTCGGTTCTACAGGGTA -3'
miR-10b DNA complementary target	5'-TACCCTGTAGAACCGAATTTGTG-3'
miR-21 DNA non-complementary target	5'-TAGCTTATCAGACTGATGTTGA-3'

in Figure 6.7B). The signal-to-noise ratio (SNR) for the measurements was computed and a blue line drawn for 3xSNR, assumed to be the limit of detection for the device. For the lower molecular weight poly-lysine, at least 100fM of miR-10b target was able to be sensed, with an extrapolated limit of detection of 1fM. However, for the higher molecular weight poly-lysine, the limit of detection at 3xSNR is close to 1nM, close to 6 orders of magnitude higher. When the mismatch miR-21 target was allowed to hybridize with the miR-10b probe, the signal was very small and steady from 100fM all the way to 1μM concentrations. Most of the miR-21 signals were close to or between 0-5mV change in signal. Error bars for the standard deviation of sweeps over the measurement are also presented on the graph for each case.

6.4 Conclusions

Here we present a process for the fabrication of HfO_2 based top-down silicon nanowires and nanoplates with high stability and robustness in fluid. The ALD process for creating the HfO_2 gate dielectric was thoroughly characterized by ellipsometry, AFM, and CV measurements to assure us of a high quality layer. The devices respond to pH in accordance to sensitivities of other HfO_2 ISFETs, with nanowires slightly more sensitive than plates. Moreover, we characterized the difference between different molecular weight layers of PLL in terms of their surface morphology, thickness, and probe attachment densities. The average thicknesses of the layers were found to be about the same by AFM and ellipsometry: however, the probe density of the lower molecular weight PLL was about twice as much as the higher molecular weight one. This was confirmed by both fluorescence and XPS. Moreover, the AFM indicated the higher molecular weight PLL was much rougher and porous, perhaps contributing to the lower response to miDNA target using this polymer. Using these different layers for sensing of miDNA on a nanowire yielded limit of detection differences over 5 orders of magnitude, with the lower molecular weight PLL having higher sensitivity. By using the lower molecular weight poly-l-lysine, we were able to detect down to 100fM of miR-10b with a theoretical limit of detection of 1fM.

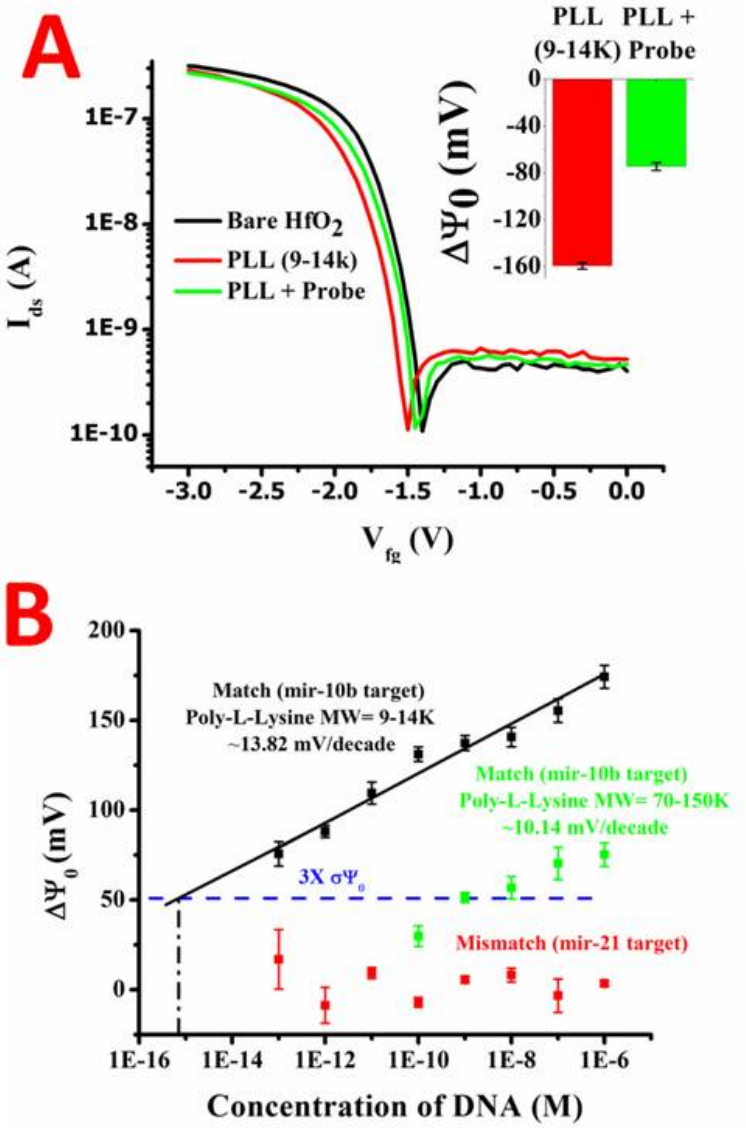

Figure 6.7: $I_d - V_g$ transfer curves of the surface functionalization process with PLL (9-14K) are shown in A. The changes in surface potential from the reference HfO_2 (A, inset) show a negative shift for the PLL deposition and the opposite shift for the probe immobilization. The change in surface potential versus the concentration of target in solution is plotted in B for the two different poly-l-lysines. The change in surface potential for the mismatched target is shown to be negligible (red symbols) and a theoretical limit of detection line is drawn in blue.

CHAPTER 7

COUPLED NANOWIRE-NANOPLATE SENSOR FOR ULTRASENSITIVE PH DETECTION

7.1 Introduction

This chapter will discuss a novel scheme for the combination of a nanowire and a nanoplate HfO_2 device for the ultrasensitive detection of pH. pH sensors in general are limited by the Nernstian limit of 59 mV/pH, with a detection limit dictated by the noise of the measurement. In this chapter, by using channels differing in width by a factor of 40, we demonstrate that the detectable signal-to-noise ratio can be vastly improved, enabling pH detection down to a theoretical 0.002 pH units, which is about one order of magnitude higher than the best value achievable with available commercial sensors. Such an ultrasensitive pH detection capability could be used for many applications, the most predominant of which is for monitoring of cancer progression from the intracellular and extracellular pH of tumor cells.

7.2 Motivation for Ultrasensitive pH Detection

Though there are a wide variety of types of cancer, tumor cells are well known to universally share many characteristics, including unbounded cell proliferation, resistance to growth-inhibitory signals, dysregulation of apoptosis, and self-induced increase in growth signals. The mechanisms underlying these characteristics are the subject of intensive study, and have yet to be fully understood. In the past fifteen years, cell pH has emerged as a possible tool to further investigate the mechanisms behind tumour progression and to measure the efficacy of cancer treatment [174]. A strong correlation has been documented by many studies between the dysregulation of pH (both intracellular and extracellular) and cancer. Normal adult cells usually ex-

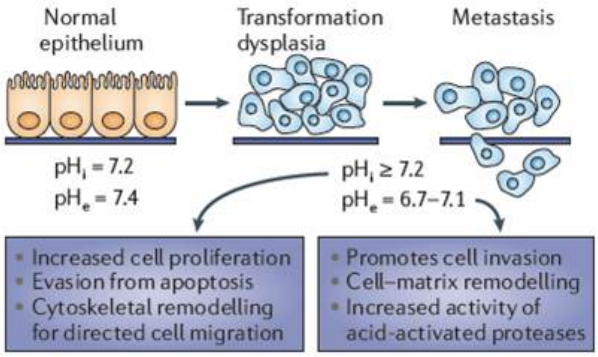

Figure 7.1: The reversed gradient of cancer cells compared to normal cells. pHi is increased by 0.2, while pHe is decreased by 0.3-0.7 pH units. This facilitates a variety of mechanisms that leads to cancer cell growth. Adapted from [174].

hibit a pH gradient of around -0.2 (intracellular pH, pHi≈7.2; extracellular pH, pHe≈7.4), which is maintained by several key cell membrane pumps. For cancer cells, however, as the tumor volume increases, the gradient is gradually reversed until pHi values of 7.4 and pHe values of 6.7-7.1 can be measured [175–179]. Although it is not yet clear what causes this pH dysregulation, a variety of cell processes are highly affected by changes in pH. Figure 7.1 illustrates a few hypotheses of the effects these observed pH shifts could have on cancer cells, including many of the main hallmarks of cancer cells (adapted from [174]). Regardless of the cause of these shifts, methods for the sensitive measurement of intracellular and extracellular pH have proven to be useful for both the monitoring of the progression of cancer [177] and for the evaluation of the efficacy of cancer treatment methods [180].

Intracellular pH in particular offers relatively uncharted territory and opportunities for both the differentiation of cancer cells from healthy cells [174], as well as for possible treatment options [181]. Conflicting reports exist, some showing increases in intracellular pH for cancer cells [175], and some with decreases over time [177]. In addition, measurements can be very noisy, increasing the minimum pH detection resolution to as much as 0.05-0.18 pH units [176], which approaches the total expected pH change from cancer to healthy cells. Intracellular measurements can become difficult due to the need to probe very small volumes of fluid within the cells of interest without perturbing intracellular activity. These measurements should be taken

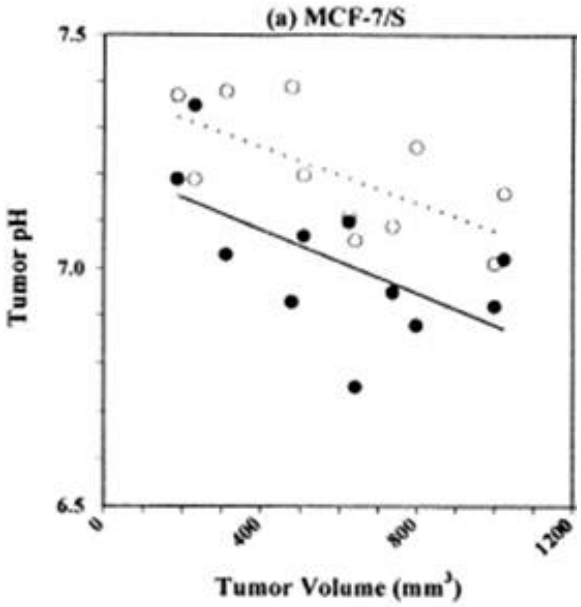

Figure 7.2: The reversed gradient of cancer cells compared to normal cells. pHi is increased by 0.2, while pHe is decreased by 0.3-0.7 pH units. This facilitates a variety of mechanisms that leads to cancer cell growth. Adapted from [174].

preferably without any modifications to the inside of the cell with as high resolution possible. Figure 7.2 shows the monitoring of both extracellular and intracellular pH in a MCF-7/S breast cancer tumor as a function of tumor size, measured with magnetic resonance spectroscopy (MRS). Definite trends of changing pHi and pHe can be seen, though the signal-to-noise ratio of the measurement has much room for improvement. There are clear opportunities for enhanced methods for detection of intracellular pH in real time with higher resolution.

A variety of methods have been developed to measure cell pH in vivo. Microelectrodes can be used for extracellular measurements but are generally too large to measure pHi [182]. magnetic resonance spectroscopy and magnetic resonance imaging (MRI) are the most commonly used techniques over the past two decades, and have the capability to measure both pHi and pHe in vivo in living tumours from animal and human models [177, 181, 183–185]. Most of the quoted values for pH have been measured with these techniques. However, MRS and MRI require elaborate machinery, trained technicians, and therefore significant resources. Fluorescent nanoparticles have recently

been investigated as possible pH sensors with high spatial resolution [186], but this technique requires bulky imaging components and labeled particles that could possibly alter cell activity. Cellular probes, such as nanorods or nanowires, have been proposed that can enter the cells in real time to monitor intracellular pH, but most studies are very preliminary, and it is not clear whether or not the invasive nature of interrogation could affect the measured results [187]. ISFETs have been used to accurately measure pH since the 1970s [48]. More recently, nanowire FET chemical and biological sensors (with widths on the order of 5-50 nm) have been shown to have improved pH measurement capability [74, 188, 189]. These FET sensors offer the attractive possibility of label-free, cheap, rapid, highly parallel, ultra-sensitive detection of pH at the nanoscale. There is a large opportunity for increasing the resolution of the pH detection (the smallest pH changes that can be detected) with these devices towards improved monitoring of minute changes in extracellular and intracellular pH of cells as a function of cancer progression.

7.3 The Nanowire-Nanoplate Combination Sensor

A schematic demonstrating the nanowire-nanoplate combination sensor is shown in Figure 7.3. Two devices of varying width are biased in parallel. T1 is a nanoplate device with width of 2 μm, and T2 is a nanowire device with width of 50 nm. The output current is measured at the shorted drain nodes of the devices as is shown in the schematic. This current is the sum of the source-drain current for both devices:

$$I = I_{DS1} + I_{DS2} \tag{7.1}$$

The two transistors have separate fluid wells and separate reference electrodes, which can be used to control the separate fluid potentials separately. T1 is considered to be the sensing element, and is exposed to solutions of varying pH with a fixed gate bias, V_{FG2}. T2 is the "transducer" element, and is exposed to only a reference solution throughout the experiments. Transfer characteristics of T2 are used as the output characteristic (by sweeping V_{FG1}), while the pH of the solutions over T2 is the input characteristic. As the pH is changed over T1, large changes in the total current I will be induced due

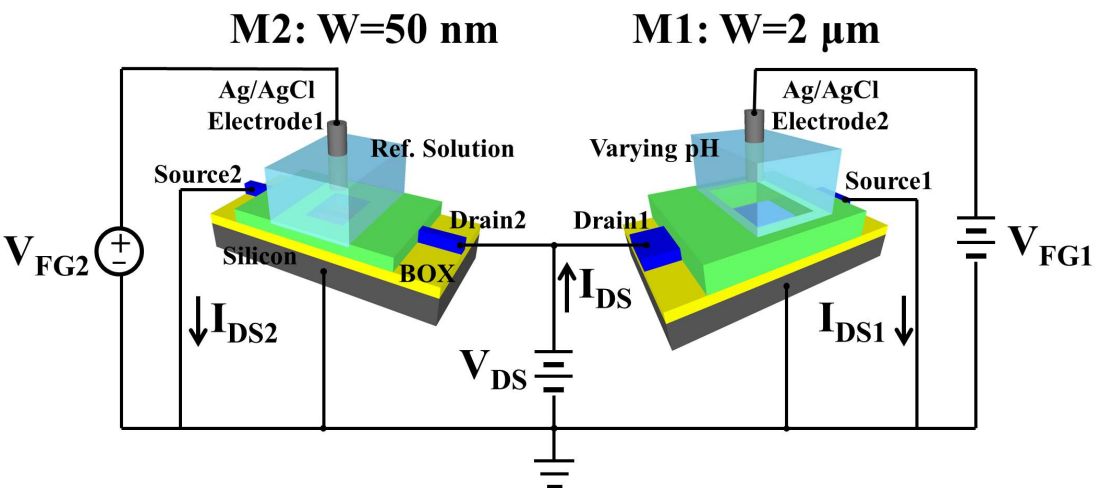

Figure 7.3: Schematic demonstrating the nanowire-nanoplate pH sensor configuration. A constant DC bias is applied to the gate of T2, the plate device. The gate of T1, the wire, is swept while the total current I is measured as a function of the pH over T2.

to the surface potential changes over T1. In order to counterbalance these large changes in current to preserve the same total current I, very large shifts in the I-V_{FG2} are needed as illustrated in Figure 7.6. These large shifts are amplified by a factor of approximately W2/W1 (about 40 in this case). This leads to a dramatic decrease in the smallest pH shift that is detectable by the system.

7.4 Theoretical Framework for the Nanowire-Nanoplate Sensor

Since T1 and T2 are both accumulation p-type devices operating in the linear regime (V_{DS}=0.25 V for both devices), the drain current modulation in T2 due to a shift in the gate voltage at T2 is given by:

$$\Delta I_{DS2} = \mu_1 C_{OX2} (W/L)_2 V_{DS} \Delta V_{FG2} \tag{7.2}$$

If T1 is kept in accumulation with a small negative V_{FG1}, then the band bending at the surface of the silicon will be very small, and when the current of T1 is modulated due to changes in pH over T1 it will be given by:

$$\Delta I_{DS1} = \mu_1 C_{OX1} (W/L)_2 V_{DS} \Delta V_{FG1} \tag{7.3}$$

where the ΔV_{FG1} term is due to changes in $\psi_0 1$, the surface potential over T1 due to changes in pH. For T2 to fully counterbalance this shift in current, we need to set $\Delta I_{DS1} = \Delta I_{DS2}$, or:

$$\frac{\Delta V_{GS2}}{\Delta V_{GS1}} = \left(\frac{\mu_1}{\mu_2} \frac{(W/L)_1}{(W/L)_2} \frac{V_{DS1}}{V_{DS2}} \right) \frac{C_{OX1}}{C_{OX2}} = \alpha \frac{C_{OX1}}{C_{OX2}} \tag{7.4}$$

With appropriate design of any of the parameters above, including device (W/L), mobility, or source-drain current, α can be much greater than 1. With current double-gated field-effect transistors, which operate on a similar principle by using differences in the oxide capacitance, this term is equal to 1 [132] and only allows one degree of freedom for control of the amplification factor.

The above analysis is only for the accumulation region and is not complete since the surface potential change over T1 due to change in pH is not a fully independent parameter. To numerically solve for the full electrostatics, we need to consider the electrostatics of the buffer, the semiconductor, and the top oxide/buffer interface in parallel [190]. Results from such a simulation are shown in Figure 7.4. Here we can see that the sensitivity factor can approach ≈10 V/pH when T1 is biased in slight accumulation, which is many orders of magnitude higher than relevant DGFET sensors (0.1-1 V/pH). In depletion (with slightly positive gate biases), the sensitivity factor can be seen to drop off, though not by much. For the rest of this work, T1 was always biased in slight accumulation.

7.5 Results and Discussion

All experimental results presented in this chapter were obtained with similar conditions to those described in Chapter 6. Individual transfer characteristics of the nanowire device and the nanoplate device at five different pH values are shown in Figure 7.5. The nanowire current is seen to be significantly lower (≈ 20X) than the current through the plate. A blown up view of the nanoplate as a function of changing pH is shown in Figure 7.5B. Values around physiological pH were chosen for higher relevance, and pH points were

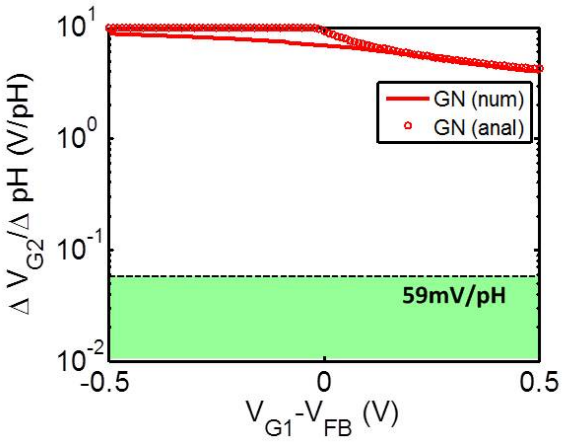

Figure 7.4: Theoretical calculation of pH sensitivity. The sensitivity is shown as a function of the bias applied to the fluid gate of the nanoplate subtracted by its flatband voltage. From [190].

designed very close to one another, since this scheme lends itself well for very high sensitivity but low dynamic range measurements. The current through T1, the nanoplate in the pH solutions, I_{DS1}, can be seen to monotonically increase with increasing pH, at about 12-13 nA per 0.1 pH increase. We have highlighted the vertical line at $V_{FG1} = -0.9V$, since this was the low constant bias applied to T1 to keep it in accumulation during the experiments.

The two devices were then connected as shown in Figure 7.3, and exposed to the different pH solutions. Transfer characteristics were extracted by sweeping V_{FG1} and measuring the total current I_{total}. Results are shown in Figure 7.6. The method for determining the shift in "threshold voltage" is also demonstrated in this figure, where essentially we take a constant current, and determine where each curve intersects a horizonal line through this current. Five sweeps were taken per pH point to quantify the average noise of the nanoplate (3.45 mV), the nanowire (2.63 mV), and of the combined system. Results for each shift, including the noise of the combined system, are shown in Table 7.1. Volts per pH is the sensitivity factor previously discussed, given by:

$$S = \frac{\Delta V_t}{\Delta pH} \tag{7.5}$$

This sensitivity factor is approximately equal to:

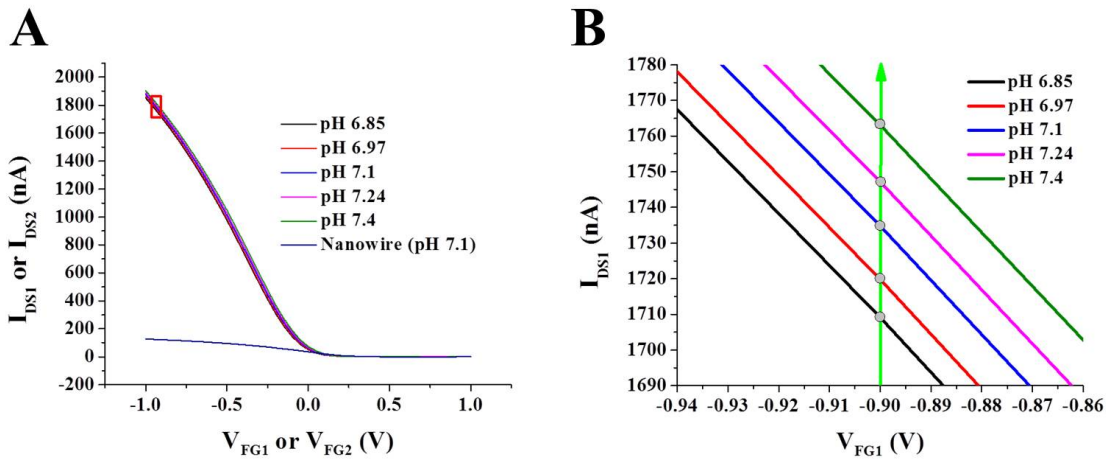

Figure 7.5: A- Transfer characteristics for the nanoplate (for 5 different pH values) and for the nanowire. B-Zoomed in region around the red rectangle in part A.

$$S = \alpha(0.059\ V/pH) \tag{7.6}$$

Using this sensitivity factor and the extracted noise for each point, we can calculate the minimum detectable pH resolution, given by:

$$\Delta pH_{min} = \frac{3}{\alpha/\delta V_t} \tag{7.7}$$

These values are plotted in Table 7.1. For the four shifts noted, the highest ΔpH_{min} observed was less than 0.002 pH units, around an order of magnitude better than any pH sensor currently available. A comparison of this minimum pH resolution to individual nanoplate, nanowire, and commercial devices is shown in Figure 7.7. It must be noted that this technique has very small dynamic range, which is limited by the window in which the transfer characteristics are swept (for example, from +1 to -2 V in Figure 7.6). It is intended as a very sensitive measurements of pH values that will not change significantly over time — for example, for use as intracellular or extracellular pH detectors of tumor cell environments.

A very puzzling part of these results is the question of why the average noise for the combined device was not amplified as a result of this configuration. To reiterate, the relevant extracted noises were (for 5 sweeps):

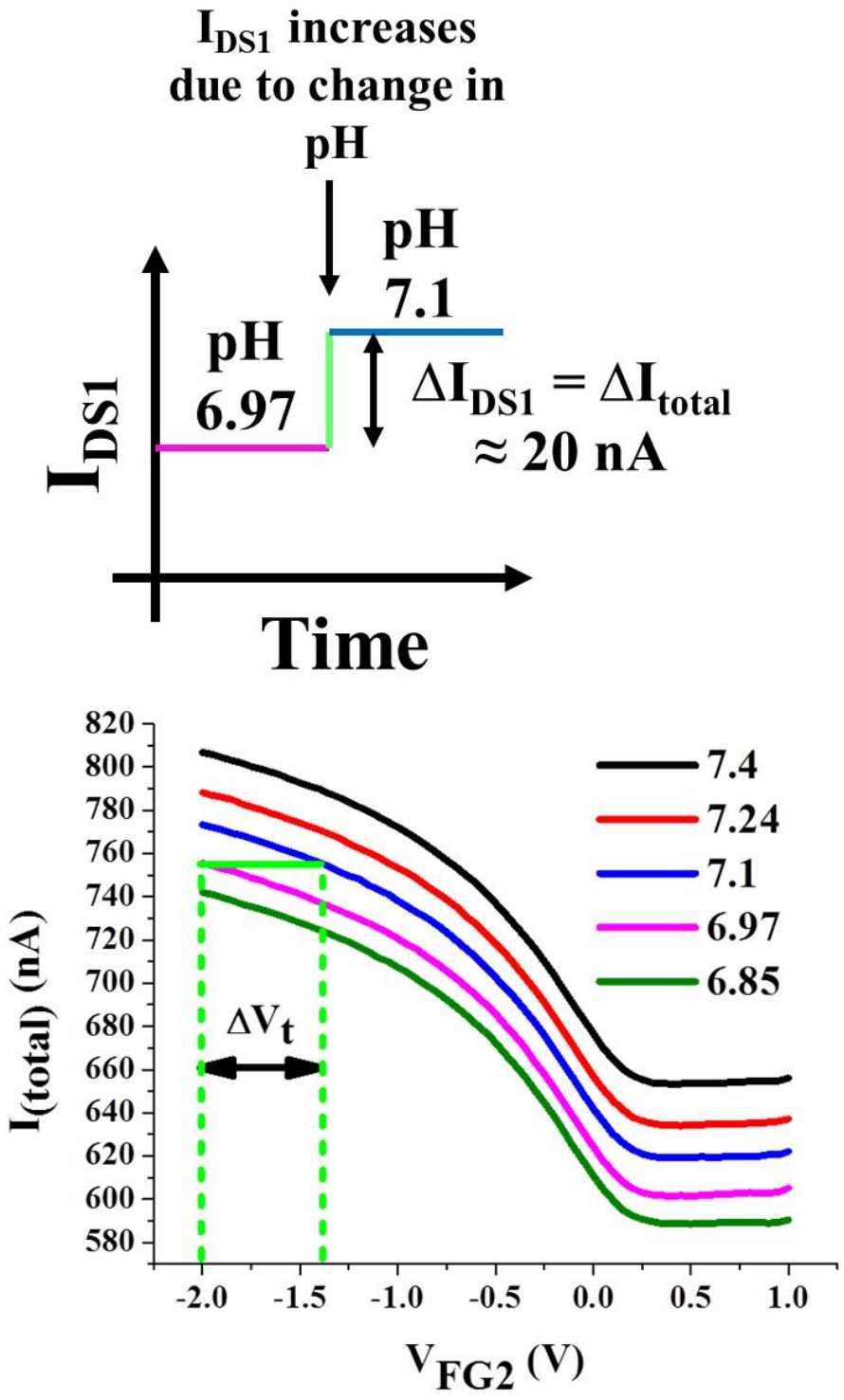

Figure 7.6: The transfer characteristics of the combined nanowire-nanoplate device as a function of pH. The green line shows an example of how the shift in threshold voltage for the device is calculated.

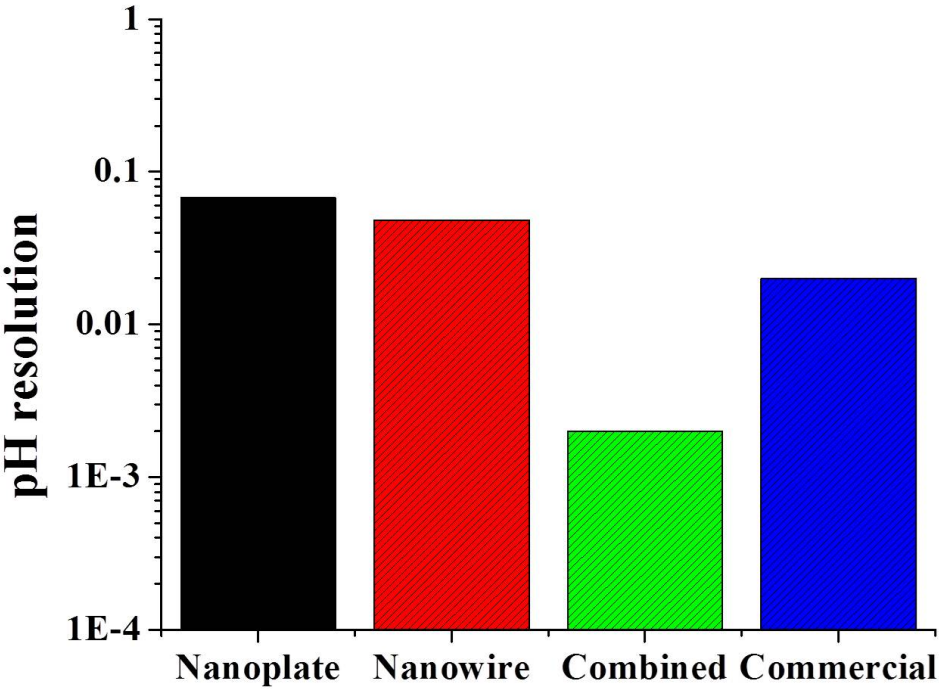

Figure 7.7: Comparison of the minimum pH detection resolution to commercial sensors, to an individual nanoplate, and to an individual nanowire sensor.

Table 7.1: Summary of sensitivity and achievable minimum pH resolutions.

pH Shift	Sensitivity: S (V/pH)	Noise: δV_t (mV)	Signal to Noise Ratio	pH Resolution pH_{min}
6.85 to 6.97	4.24	2.36	1798	0.00167
6.97 to 7.1	4.51	1.28	3525	0.00085
7.1 to 7.24	3.72	2.01	1848	0.00162
7.24 to 7.4	3.94	1.10	3582	0.00084

- Individual nanowire: 2.63 mV
- Individual nanoplate: 3.45 mV
- Combined device, sweeping the nanowire: < 3 mV

It would be initially expected that this noise should also be multiplied by the amplification factor ($\alpha > 40$ for this work) for the combination configuration. Further analysis, however, yields deeper insight.

For a sensor operating in its linear regime, the spectral density of fluctuations in gate voltage for a given source-drain current is primarily dominated by FET noise, not by the electrolyte noise ($I_0 \approx 10$mM), and can be given by [191]:

$$S_{Vg} = S_{V_fb}\left[1 + \left(\alpha\mu_{eff}C_{eff}\frac{I_D}{g_m}\right)\right]^2 \tag{7.8}$$

where

$$S_{Vfb} = \frac{q^2kTN_t\lambda}{fWLC_{eff}^2} \tag{7.9}$$

and

$$I_D = \mu_{eff} C_{eff} \frac{W}{L}(V_G - V_T)V_{DS},\ g_m = \frac{dI_D}{dV_G} = \mu_{eff} C_{eff} \frac{W}{L} V_{DS} \qquad (7.10)$$

From these expressions, it can be seen that the average voltage fluctuation δV is proportional $1/W$. We would therefore expect the average noise for the nanoplate device to be far below that of the nanowire, which is not seen (3.45 mV $>$ 2.63 mV). This is actually quite intuitive, since for stochastic processes, higher device areas should allow for better integration of noise events and thus less overall noise. This apparent discrepancy can be explained by assuming an overall noise of the environment S_{env}, where $S_{env} \geq S_{nw} >> S_{np}$, where S_{nw} and S_{np} are the intrinsic device noises for the nanowire and the nanoplate, respectively. These noises are distinct from the actual measured noise of an experiment, which will always be dominated by the largest noise source — in this case, S_{env}. The noise of the environment can include many factors, including the electrical measurement system, fluctuations in surface potential and ions at the nanoplate interface, changes in the fluid electrode, etc. The combination noise of the system then is:

$$S_{overall} = max(S_{env},\ \alpha S_{np},\ S_{nw}) \qquad (7.11)$$

From Equation 7.11, we can see that as long as αS_{np} stays below S_{env}, Equation 7.6 for the sensitivity per pH value will hold, and the overall minimum detectable pH value will be decreased by α. Fortunately, S_{np} can be arbitrarily controlled by the device width of T1 so that this is always the case. This concept is further illustrated in Figure 7.8.

7.6 Conclusions

In conclusion, we have demonstrated the use of a nanowire-nanoplate combination sensor for the detection of pH units down to 0.002, which is an order of magnitude better than commercial sensors and is, to our knowledge, the most sensitive bioFET pH sensor reported to date. An increase in the observed signal was achieved by a huge difference in the source-drain currents of the two devices, which was used to induce a large threshold shift for the nanowire device due to pH changes on the nanoplate device. The measured

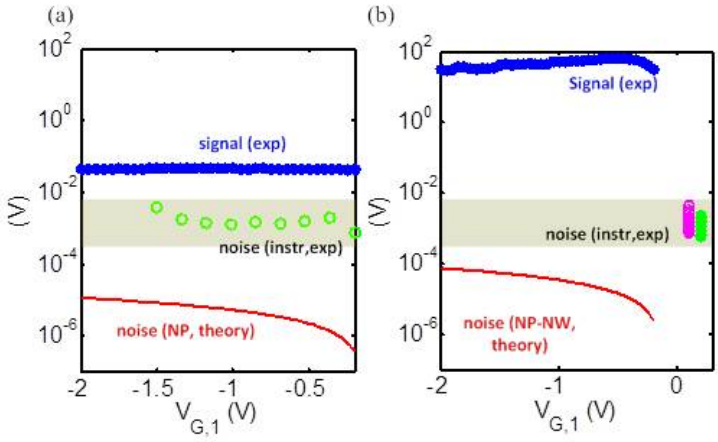

Figure 7.8: (a) The measured signal (blue dots) and instrument noise (green circles) plotted as a function of the nanoplate gate bias for the nanoplate sensor. (b) Corresponding plot for the combined sensor scheme. The theoretical limit of the noise is also shown in red (solid curve). The ratios of signal to nosie in each figure indicate the SNR of each sensor configuration

noise was not enhanced in this process due to an environmental noise factor that was larger than the intrinsic nanoplate and nanowire noise. As long as the intrinsic nanoplate noise is kept to lower than the environmental noise divided by α, the amplification factor, the resulting pH sensitivity will be $\alpha(0.059$ mV/pH). This method for ultrasensitive detection can be used for many applications, including the monitoring of intracellular and extracellular pH in tumor cells.

CHAPTER 8

CONCLUSIONS AND FUTURE WORK

8.1 Conclusions

This dissertation has demonstrated progress towards developing a repeatable, reliable, and robust nanoFET sensor platform for the ultrasensitive detection of pH, nucleic acid oligomers, and proteins. In Chapter 2, we discussed the relevant literature and background for field-effect sensors, which allow for the sensitive, label-free detection of pH changes and biomolecules in solution. The technology offers several important advantages over related technologies, including amenability to scale-up, ease of integration, low per unit cost, low sample volumes, quick detection times, and very high sensitivity to low concentrations of target analytes. Chapter 3 described the silicon dioxide gate dielectric fabrication process used as a baseline for the rest of the work, including efforts to optimize many important features such as the definition of nanoscale structures, silicon doping concerns, contact resistance, fluid passivation, and exposure of the devices to fluid. In Chapter 4, these devices were used for the detection of pyrophosphate generated from DNA polymerase activity, for the detection of short DNA strands down to 1 nM, and for the detection of mouse-IgG1 proteins down to 8 fM. These applications demonstrate that the fabricated devices can be used as sensitive detectors of charge. Chapter 5 illustrated possible improvements to the baseline process introduced in Chapter 3, specifically by the addition of an ALD deposited Al_2O_3 gate dielectric layer in place of SiO_2. With a dielectric constant of approximately 9, aluminum oxide offers several advantages over silicon dioxide for biosensors, including increased sensitivity to pH due to increased buffer capacity, higher oxide capacitances which lead to better device subthreshold slope and transconductance, and better protection of the silicon channel in fluid environments. The Al_2O_3 devices were demonstrated

to have higher sensitivity to pH when compared to their counterpart SiO_2 devices. In addition, the importance of optimization of the backgate for such sensors was illustrated, and the effect of device width on pH sensitivity was explored. The further extrapolation of this fabrication process was discussed in Chapter 6, which detailed additional fabrication steps from the baseline process needed to fabricate HfO_2 gate dielectric devices. In this iteration, several key characterization steps of the gate dielectric-silicon interface were carefully optimized to reduce the final biosensor noise and decrease minimum detectable pH changes and biomolecular concentrations. Using this architecture, we demonstrated pH sensitivity of 55.8 mV/pH for nanowire devices and 51.0 mV/pH for nanoplate devices. The devices were extremely stable in fluid, had low leakage currents, and were operational for thousands of sweeps for hours in fluidic environments. The devices were also used for the detection of DNA analogues of important cancer-related microRNA sequences, down to 100 fM, with a theoretical detection sensitivity of around 1 fM. Finally, Chapter 7 discussed a novel dual nanowire-nanoplate combination scheme for ultrasensitive detection of pH. By amplifying the threshold voltage shift seen per pH value while keeping the noise limit below the environmental noise, we were able to demonstrate 4-5 V/pH sensitivity, with the theoretical capability to detect changes in pH as low as 0.002, which is at least an order of magnitude better than available commercial sensors. The results presented in this dissertation can be used for a variety of applications, from detection of intracellular and extracellular pH in tumor cells to PCR detection to the sensitive, robust sensing of a wide variety of important biomolecules for cancer diagnosis and understanding of complex pathways in the human body that lead to disease.

8.2 Future Work

With the development of the robust HfO_2 platform, several exciting sensing applications can be explored in the near future. In addition, the combination nanowire-nanoplate scheme offers opportunities for use in several important applications.

8.2.1 Detection of MicroRNA

The most immediate application where the sensors can be used is the detection of microRNA. The concentration of several miRNA sequences are well known to be correlated to the stage of cancer, as was discussed in Chapter 6. We demonstrated detection of mir-10b synthetic DNA down to 100 fM in this dissertation. The opportunities here include:

- Detection of synthetic RNA, which is less stable than the DNA detected in this work.
- Decreasing the detection limits. We showed that 1 fM detection should be theoretically possible.
- Testing the crosstalk between mir-10b, mir-21, and other cancer related microRNA.
- Detection of specific miRNA sequences from total microRNA (all of the microRNA) that can be isolated from cell lines using commercially available kits. Table 8.1 demonstrates some initial quantification of of the numbers of five sequences of miRNA isolated from two different cell lines, MCF7 (breast cancer cell line) and MCF10 (non-cancerous negative control) from collaborators at Ohio State University from 1 million cells. Ideally, we would like to match electrical results to results similar to these, which are typically quantified with real time PCR (RTPCR) after extraction.
- Detection of specific miRNA sequences from totalRNA, which is similar to the step above, except with all of the RNA from cell lines, including much longer sequences.
- Detection of specific miRNA sequences from a bodily fluid, such as breast aspirate fluid.

The devices illustrated in this dissertation have repeatable characteristics that will hopefully enable these applications.

Table 8.1: MicroRNA expression profiles for MCF7 (cancerous) and MCF10a(non-cancerous) cell lines. Results from M. Paulaitis at Ohio State University.

micro RNA	MCF7 average expression level	MCF10a average expression level
miR-21	1,890,829	96,814
let-7a	843,351	578,865
miR-16	746,992	263,728
miR-26a	298,485	72,385
miR-221	97,891	243,511

8.2.2 Detection of PCR and Cell Lysate via Minute Changes in pH

Our group recently demonstrated that each of our FET biosensors can also be used as a nanoscale heating element with ultrahigh spatial resolution in both the lateral and vertical directions [189, 192]. We are also currently pursuing scale-down of this technique in individual droplets to reduce the heat sink of a large well. Initial results show that the application of the AC bias between the shorted source-drain node of a transistor and the backgate can induce repeatable temperature profiles in the fluid directly above the devices. We have shown some preliminary results of the use of this heating technique for rapid, highly miniaturized PCR on chip and for the localized lysing of cells. Here, the cell is moved to the wire via a novel magnetic tweezer technique from Ohio State University [193]. The cells are allowed to settle to the surface of the devices, and the heating voltages are turned on. Live/dead stains are used to verify the state of the cell. As can be seen from the images and the plots, as the heating voltage is turned on, the cells gradually electroporate and destruct, which allows the dead dye, propidium iodide, to enter the cell and fluoresce.

We hope to use the ultrasensitive pH technique described in Chapter 7 to sense the local changes in pH that should be induced from lysing the cell. As described previously, the intracellular pH is slightly different from the external pH, and should reflect transitory local pH changes at the surfaces that can be monitored by the devices. If these differences can be observed

and recorded, it may be possible to eventually differentiate cancerous cells from healthy cells using this technique. Additionally, the devices could be functionalized with probes molecules for interesting nucleic acids, proteins, or other relevant molecules that would be freed upon cell lysis. This eventually may be able to replace all the traditional "front-end" sample preparation steps typically required for lab-on-a-chip sensors.

It is also well known that for every base pair added by DNA polymerase in PCR reactions, a H^+ ion is a by-product of the base pair addition. The entire sensing mechanism behind Ion Torrent's DNA sequencing takes advantage of this fact. However, there are issues with the current sensitivity of electrical measurement of PCR [13]. Another opportunity for the sensors would be to combine on chip PCR with the heating elements with electrical, label free detection of PCR. Such results could enable the possibility of scalable, microscale PCR reactions in a highly integrated fashion, with both the heating and detection element employing a very small footprint on a chip that could easily be combined with signal processing electronics for a true large density PCR array.

8.2.3 Other Relevant Biomarkers

A wide variety of other biomarkers are important for a variety of diseases, including cancer. Using the platform established in this disseration, we can investigate the possibility of using our sensors as true indicators of the expression levels of important DNA, RNA, miRNA, and various proteins for different pathways in the human body. After a base chemical attachment scheme is fully established, such as that used to attach the miRNA probes in Chapter 6, the only difference between devices targeted at different analytes is the probe molecules that must first be immobilized. As discussed in the motivation of this thesis, information on the concentrations of such biomarkers has the potential to yield invaluable knowledge about a plethora of cell pathways and mechanisms, an understanding that eventually can translate into dramatically increasing the efficacies of many treatments for a vast collection of diseases.

REFERENCES

[1] M. Blaghman, *Cancer Facts and Figures*. American Cancer Society, 2011.

[2] B. Alberts, A. Johnson, J. Lewis, M. Raff, K. Roberts, and P. Walter, *Molecular Biology of the Cell*, 4th ed. New York: Garland Science, 2002.

[3] S. A. Soper, K. Brown, A. Ellington, B. Frazier, G. Garcia-Manero, V. Gau, S. I. Gutman, D. F. Hayes, B. Korte, J. L. Landers, D. Larson, F. Ligler, A. Majumdar, M. Mascini, D. Nolte, Z. Rosenzweig, J. Wang, and D. Wilson, "Point-of-care biosensor systems for cancer diagnostics/prognostics," *Biosensors & Bioelectronics*, vol. 21, no. 10, pp. 1932–1942, 2006, 032EG Times Cited:64 Cited References Count:96.

[4] H. Nakamura and I. Karube, "Current research activity in biosensors," *Analytical and Bioanalytical Chemistry*, vol. 377, no. 3, pp. 446–468, 2003, 724JZ Times Cited:132 Cited References Count:385.

[5] J. Lu, G. Getz, E. A. Miska, E. Alvarez-Saavedra, J. Lamb, D. Peck, A. Sweet-Cordero, B. L. Ebet, R. H. Mak, A. A. Ferrando, J. R. Downing, T. Jacks, H. R. Horvitz, and T. R. Golub, "MicroRNA expression profiles classify human cancers," *Nature*, vol. 435, no. 7043, pp. 834–838, 2005, 933NK Times Cited:2133 Cited References Count:30.

[6] J. C. Brase, D. Wuttig, R. Kuner, and H. Sultmann, "Serum microRNAs as non-invasive biomarkers for cancer," *Molecular Cancer*, vol. 9, 2010, 695HV Times Cited:3 Cited References Count:86.

[7] N. Miller, H. M. Heneghan, A. J. Lowery, K. J. Sweeney, J. Newell, and M. J. Kerin, "Circulating microRNAs as novel minimally invasive biomarkers for breast cancer," *Annals of Surgery*, vol. 251, no. 3, pp. 499–505, 2010, 562OD Times Cited:43 Cited References Count:27.

[8] M. C. Rodicio and M. de Planell-Saguer, "Analytical aspects of microRNA in diagnostics: A review," *Analytica Chimica Acta*, vol. 699, no. 2, pp. 134–152, 2011, 797EE Times Cited:0 Cited References Count:180.

[9] Y. S. Sun, J. P. Landry, Y. Y. Fei, and X. D. Zhu, "Effect of fluorescently labeling protein probes on kinetics of protein-ligand reactions," *Langmuir*, vol. 24, no. 23, pp. 13 399–13 405, 2008, 376XO Times Cited:20 Cited References Count:25.

[10] T. Kodadek, "Protein microarrays: prospects and problems," *Chemistry & Biology*, vol. 8, no. 2, pp. 105–115, 2001, 418BF Times Cited:304 Cited References Count:38.

[11] C. L. Corless, "Personalized cancer diagnostics," *Science*, vol. 334, no. 6060, pp. 1217–1218, 2011, 855HD Times Cited:0 Cited References Count:5.

[12] S. Roychowdhury, M. K. Iyer, D. R. Robinson, R. J. Lonigro, Y. M. Wu, X. H. Cao, S. Kalyana-Sundaram, L. Sam, O. A. Balbin, M. J. Quist, T. Barrette, J. Everett, J. Siddiqui, L. P. Kunju, N. Navone, J. C. Araujo, P. Troncoso, C. J. Logothetis, J. W. Innis, D. C. Smith, C. D. Lao, S. Y. Kim, J. S. Roberts, S. B. Gruber, K. J. Pienta, M. Talpaz, and A. M. Chinnaiyan, "Personalized oncology through integrative high-throughput sequencing: A pilot study," *Science Translational Medicine*, vol. 3, no. 111, 2011, 862GX Times Cited:2 Cited References Count:50.

[13] J. M. Rothberg, W. Hinz, T. M. Rearick, J. Schultz, W. Mileski, M. Davey, J. H. Leamon, K. Johnson, M. J. Milgrew, M. Edwards, J. Hoon, J. F. Simons, D. Marran, J. W. Myers, J. F. Davidson, A. Branting, J. R. Nobile, B. P. Puc, D. Light, T. A. Clark, M. Huber, J. T. Branciforte, I. B. Stoner, S. E. Cawley, M. Lyons, Y. T. Fu, N. Homer, M. Sedova, X. Miao, B. Reed, J. Sabina, E. Feierstein, M. Schorn, M. Alanjary, E. Dimalanta, D. Dressman, R. Kasinskas, T. Sokolsky, J. A. Fidanza, E. Namsaraev, K. J. McKernan, A. Williams, G. T. Roth, and J. Bustillo, "An integrated semiconductor device enabling non-optical genome sequencing," *Nature*, vol. 475, no. 7356, pp. 348–352, 2011, 794PA Times Cited:2 Cited References Count:46.

[14] J. Wang, "Electrochemical biosensors: Towards point-of-care cancer diagnostics," *Biosensors & Bioelectronics*, vol. 21, no. 10, pp. 1887–1892, 2006, 032EG Times Cited:219 Cited References Count:43.

[15] G. J. Kost, "Point-of-care testing - clinical immediacy, significance, and outcomes," *American Journal of Clinical Pathology*, vol. 104, no. 4, pp. S1–S1, 1995, suppl. 1 Tb088 Times Cited:2 Cited References Count:0.

[16] G. J. Kost, S. S. Ehrmeyer, B. Chernow, J. W. Winkelman, G. P. Zaloga, R. R. Dellinger, and T. Shirey, "The laboratory-clinical interface

- point-of-care testing," *Chest*, vol. 115, no. 4, pp. 1140–1154, 1999, 185EV Times Cited:41 Cited References Count:79.

[17] M. L. Kilgore, S. J. Steindel, and J. A. Smith, "Cost analysis for decision support: The case of comparing centralized versus distributed methods for blood gas testing," *Journal of Healthcare Management*, vol. 44, no. 3, pp. 207–215, 1999, 194QY Times Cited:7 Cited References Count:12.

[18] J. Douketis and M. A. Crowther, "Twice daily enoxaparin, but not once daily dalteparin, is associated with elevated anti-factor xa heparin levels at the time of epidural catheter removal." *Blood*, vol. 98, no. 11, pp. 707a–707a, 2001, part 1 491WY 2954 Times Cited:0 Cited References Count:0.

[19] C. P. Price, "Regular review - point of care testing," *British Medical Journal*, vol. 322, no. 7297, pp. 1285–1288, 2001, 437YW Times Cited:60 Cited References Count:26.

[20] R. Bashir, "BioMEMs: state-of-the-art in detection, opportunities and prospects," *Advanced Drug Delivery Reviews*, vol. 56, no. 11, pp. 1565–1586, 2004, 857QK Times Cited:154 Cited References Count:163.

[21] D. Bowtell and J. Sambrook, *DNA Microarrays: A Molecular Cloning Manual*, 1st ed. Cold Spring Harbor, New York: Cold Spring Harbor Laboratory Press, 2003.

[22] D. Gresham, M. J. Dunham, and D. Botstein, "Comparing whole genomes using DNA microarrays," *Nature Reviews Genetics*, vol. 9, no. 4, pp. 291–302, 2008, 275PM Times Cited:59 Cited References Count:112.

[23] M. T. Barrett, A. Scheffer, A. Ben-Dor, N. Sampas, D. Lipson, R. Kincaid, P. Tsang, B. Curry, K. Baird, P. S. Meltzer, Z. Yakhini, L. Bruhn, and S. Laderman, "Comparative genomic hybridization using oligonucleotide microarrays and total genomic DNA," *Proceedings of the National Academy of Sciences of the United States of America*, vol. 101, no. 51, pp. 17 765–17 770, 2004, 882PT Times Cited:195 Cited References Count:26.

[24] R. Redon, S. Ishikawa, K. R. Fitch, L. Feuk, G. H. Perry, T. D. Andrews, H. Fiegler, M. H. Shapero, A. R. Carson, W. W. Chen, E. K. Cho, S. Dallaire, J. L. Freeman, J. R. Gonzalez, M. Gratacos, J. Huang, D. Kalaitzopoulos, D. Komura, J. R. MacDonald, C. R. Marshall, R. Mei, L. Montgomery, K. Nishimura, K. Okamura, F. Shen, M. J. Somerville, J. Tchinda, A. Valsesia, C. Woodwark, F. T. Yang, J. J. Zhang, T. Zerjal, J. Zhang, L. Armengol, D. F. Conrad, X. Estivill,

C. Tyler-Smith, N. P. Carter, H. Aburatani, C. Lee, K. W. Jones, S. W. Scherer, and M. E. Hurles, "Global variation in copy number in the human genome," *Nature*, vol. 444, no. 7118, pp. 444–454, 2006, 108BQ Times Cited:1553 Cited References Count:77.

[25] B. A. Weir, M. S. Woo, G. Getz, S. Perner, L. Ding, R. Beroukhim, W. M. Lin, M. A. Province, A. Kraja, L. A. Johnson, K. Shah, M. Sato, R. K. Thomas, J. A. Barletta, I. B. Borecki, S. Broderick, A. C. Chang, D. Y. Chiang, L. R. Chirieac, J. Cho, Y. Fujii, A. F. Gazdar, T. Giordano, H. Greulich, M. Hanna, B. E. Johnson, M. G. Kris, A. Lash, L. Lin, N. Lindeman, E. R. Mardis, J. D. McPherson, J. D. Minna, M. B. Morgan, M. Nadel, M. B. Orringer, J. R. Osborne, B. Ozenberger, A. H. Ramos, J. Robinson, J. A. Roth, V. Rusch, H. Sasaki, F. Shepherd, C. Sougnez, M. R. Spitz, M. S. Tsao, D. Twomey, R. G. W. Verhaak, G. M. Weinstock, D. A. Wheeler, W. Winckler, A. Yoshizawa, S. Y. Yu, M. F. Zakowski, Q. Y. Zhang, D. G. Beer, I. I. Wistuba, M. A. Watson, L. A. Garraway, M. Ladanyi, W. D. Travis, W. Pao, M. A. Rubin, S. B. Gabriel, R. A. Gibbs, H. E. Varmus, R. K. Wilson, E. S. Lander, and M. Meyerson, "Characterizing the cancer genome in lung adenocarcinoma," *Nature*, vol. 450, no. 7171, pp. 893–U22, 2007, 237RU Times Cited:343 Cited References Count:40.

[26] J. R. Pollack, C. M. Perou, A. A. Alizadeh, M. B. Eisen, A. Pergamenschikov, C. F. Williams, S. S. Jeffrey, D. Botstein, and P. O. Brown, "Genome-wide analysis of DNA copy-number changes using cDNA microarrays," *Nature Genetics*, vol. 23, no. 1, pp. 41–46, 1999, 231XU Times Cited:863 Cited References Count:30.

[27] M. J. Dunham, H. Badrane, T. Ferea, J. Adams, P. O. Brown, F. Rosenzweig, and D. Botstein, "Characteristic genome rearrangements in experimental evolution of saccharomyces cerevisiae," *Proceedings of the National Academy of Sciences of the United States of America*, vol. 99, no. 25, pp. 16 144–16 149, 2002, 624VY Times Cited:210 Cited References Count:49.

[28] R. Lucito, M. Nakimura, J. A. West, H. Ying, K. Chin, K. Jensen, R. McCombie, J. W. Gray, and M. Wigler, "Genetic analysis using genomic representations," *Proceedings of the National Academy of Sciences of the United States of America*, vol. 95, no. 8, pp. 4487–4492, 1998, zh535 Times Cited:47 Cited References Count:40.

[29] J. B. Fan, M. S. Chee, and K. L. Gunderson, "Highly parallel genomic assays," *Nature Reviews Genetics*, vol. 7, no. 8, pp. 632–644, 2006, 064VR Times Cited:171 Cited References Count:156.

[30] O. P. Kallioniemi, "Biochip technologies in cancer research," *Annals of Medicine*, vol. 33, no. 2, pp. 142–147, 2001, 421HU Times Cited:51 Cited References Count:14.

[31] R. M. Lequin, "Enzyme immunoassay (EIA)/enzyme-linked immunosorbent assay (ELISA)," *Clinical Chemistry*, vol. 51, no. 12, pp. 2415–2418, 2005, 987QV Times Cited:93 Cited References Count:27.

[32] R. S. Gaster, D. A. Hall, C. H. Nielsen, S. J. Osterfeld, H. Yu, K. E. Mach, R. J. Wilson, B. Murmann, J. C. Liao, S. S. Gambhir, and S. X. Wang, "Matrix-insensitive protein assays push the limits of biosensors in medicine," *Nature Medicine*, vol. 15, no. 11, pp. 1327–U130, 2009, 516LM Times Cited:8 Cited References Count:33.

[33] R. Fan, O. Vermesh, A. Srivastava, B. K. H. Yen, L. D. Qin, H. Ahmad, G. A. Kwong, C. C. Liu, J. Gould, L. Hood, and J. R. Heath, "Integrated barcode chips for rapid, multiplexed analysis of proteins in microliter quantities of blood," *Nature Biotechnology*, vol. 26, no. 12, pp. 1373–1378, 2008, 382FR Times Cited:97 Cited References Count:33.

[34] S. Yang, A. Undar, and J. D. Zahn, "A microfluidic device for continuous, real time blood plasma separation," *Lab on a Chip*, vol. 6, no. 7, pp. 871–880, 2006, 057FE Times Cited:99 Cited References Count:35.

[35] J. Barnas, A. Fuss, R. E. Camley, P. Grunberg, and W. Zinn, "Novel magnetoresistance effect in layered magnetic-structures - theory and experiment," *Physical Review B*, vol. 42, no. 13, pp. 8110–8120, 1990, eg488 Times Cited:299 Cited References Count:34.

[36] G. A. Prinz, "Magnetoelectronics (vol 282, pg 1660, 1998)," *Science*, vol. 283, no. 5400, pp. 330–330, 1999, 157MV Times Cited:12 Cited References Count:1.

[37] R. F. Pierret, *Semiconductor Device Fundamentals*. Addison-Wesley Publishing Group, 1996.

[38] J. M. Gao, F. A. Gomez, R. Harter, and G. M. Whitesides, "Determination of the effective charge of a protein in solution by capillary electrophoresis," *Proceedings of the National Academy of Sciences of the United States of America*, vol. 91, no. 25, pp. 12 027–12 030, 1994, pw708 Times Cited:53 Cited References Count:18.

[39] J. Fritz, E. B. Cooper, S. Gaudet, P. K. Sorger, and S. R. Manalis, "Electronic detection of DNA by its intrinsic molecular charge," *Proceedings of the National Academy of Sciences of the United States of America*, vol. 99, no. 22, pp. 14 142–14 146, 2002, 610NT Times Cited:204 Cited References Count:32.

[40] C. S. J. Hou, N. Milovic, M. Godin, P. R. Russo, R. Chakrabarti, and S. R. Manalis, "Label-free microelectronic PCR quantification," *Analytical Chemistry*, vol. 78, no. 8, pp. 2526–2531, 2006, 034RM Times Cited:13 Cited References Count:34.

[41] C. S. J. Hou, M. Godin, K. Payer, R. Chakrabarti, and S. R. Manalis, "Integrated microelectronic device for label-free nucleic acid amplification and detection," *Lab on a Chip*, vol. 7, no. 3, pp. 347–354, 2007, 141ZD Times Cited:7 Cited References Count:48.

[42] N. M. Milovic, J. R. Behr, M. Godin, C. S. J. Hou, K. R. Payer, A. Chandrasekaran, P. R. Russo, R. Sasisekharan, and S. R. Manalis, "Monitoring of heparin and its low-molecular-weight analogs by silicon field effect," *Proceedings of the National Academy of Sciences of the United States of America*, vol. 103, no. 36, pp. 13 374–13 379, 2006, 084DR Times Cited:9 Cited References Count:50.

[43] R. Freeman, J. Elbaz, R. Gill, M. Zayats, and I. Willner, "Analysis of dopamine and tyrosinase activity on ion-sensitive field-effect transistor (ISFET) devices," *Chemistry-a European Journal*, vol. 13, no. 26, pp. 7288–7293, 2007, 212CI Times Cited:20 Cited References Count:22.

[44] R. Freeman, R. Gill, and I. Willner, "Following a protein kinase activity using a field-effect transistor device," *Chemical Communications*, no. 33, pp. 3450–3452, 2007, 200YD Times Cited:18 Cited References Count:17.

[45] J. Hahm and C. M. Lieber, "Direct ultrasensitive electrical detection of DNA and DNA sequence variations using nanowire nanosensors," *Nano Letters*, vol. 4, no. 1, pp. 51–54, 2004, 764YA Times Cited:372 Cited References Count:22.

[46] Y. W. Chen, M. Z. Liu, T. Kaneko, and P. C. McIntyre, "Atomic layer deposited hafnium oxide gate dielectrics for charge-based biosensors," *Electrochemical and Solid State Letters*, vol. 13, no. 3, pp. G29–G32, 2010, 544WL Times Cited:0 Cited References Count:24.

[47] P. Bergveld, "Development of an ion-sensitive solid-state device for neurophysiological measurements," *Ieee Transactions on Biomedical Engineering*, vol. 17, no. 1, pp. 70–71, 1970, f3208 Times Cited:623 Cited References Count:5.

[48] P. Bergveld, "Thirty years of ISFETology - what happened in the past 30 years and what may happen in the next 30 years," *Sensors and Actuators B-Chemical*, vol. 88, no. 1, pp. 1–20, 2003, 630YT Times Cited:233 Cited References Count:50.

[49] R. E. G. vanHal, J. C. T. Eijkel, and P. Bergveld, "A general model to describe the electrostatic potential at electrolyte oxide interfaces," *Advances in Colloid and Interface Science*, vol. 69, pp. 31–62, 1996, wd121 Times Cited:67 Cited References Count:21.

[50] P. Bergveld, "The operation of an ISFET as an electronic device," *Sensors and Actuators*, vol. 1, no. 1, pp. 17–29, 1981, ly432 Times Cited:82 Cited References Count:0.

[51] P. Bergveld, "Future applications of ISFETs," *Sensors and Actuators B-Chemical*, vol. 4, no. 1-2, pp. 125–133, 1991, fj819 Times Cited:24 Cited References Count:22.

[52] P. Bergveld, "A critical-evaluation of direct electrical protein-detection methods," *Biosensors & Bioelectronics*, vol. 6, no. 1, pp. 55–72, 1991, ff429 Times Cited:69 Cited References Count:35.

[53] P. Bergveld, "The future of biosensors," *Sensors and Actuators a-Physical*, vol. 56, no. 1-2, pp. 65–73, 1996, wa070 Times Cited:55 Cited References Count:16.

[54] G. A. J. Besselink, R. B. M. Schasfoort, and P. Bergveld, "Modification of ISFETs with a monolayer of latex beads for specific detection of proteins," *Biosensors & Bioelectronics*, vol. 18, no. 9, pp. 1109–1114, 2003, 697KV Times Cited:21 Cited References Count:13.

[55] J. C. T. Eijkel, W. Olthuis, and P. Bergveld, "An ISFET-based dipstick device for protein detection using the ion-step method," *Biosensors & Bioelectronics*, vol. 12, no. 9-10, pp. 991–1001, 1997, yq268 Times Cited:8 Cited References Count:13.

[56] W. Olthuis, P. Bergveld, and J. Kruise, "The exploitation of ISFETs to determine the acid-base behaviour of proteins," *Electrochimica Acta*, vol. 43, no. 23, pp. 3483–3488, 1998, 115HR Times Cited:2 Cited References Count:13.

[57] R. B. M. Schasfoort, P. Bergveld, J. Bomer, R. P. H. Kooyman, and J. Greve, "Modulation of the ISFET response by an immunological reaction," *Sensors and Actuators*, vol. 17, no. 3-4, pp. 531–535, 1989, u4964 Times Cited:12 Cited References Count:3.

[58] J. Kruise, J. C. T. Eijkel, and P. Bergveld, "Detection of protein concentrations using a pH-step titration method," *Sensors and Actuators B-Chemical*, vol. 44, no. 1-3, pp. 297–303, 1997, yu444 Times Cited:4 Cited References Count:10.

[59] J. Kruise, J. G. Rispens, P. Bergveld, F. J. B. Kremer, D. Starmans, J. R. Haak, J. Feijen, and D. N. Reinhoudt, "Detection of charged proteins by means of impedance measurements," *Sensors and Actuators B-Chemical*, vol. 6, no. 1-3, pp. 101–105, 1992, hn692 Times Cited:9 Cited References Count:7.

[60] W. Olthuis, J. Luo, and P. Bergveld, "Characterization of proteins by means of their buffer capacity, measured with an ISFET-based coulometric sensor-actuator system," *Biosensors & Bioelectronics*, vol. 9, no. 9-10, pp. 743–751, 1994, qd262 Times Cited:4 Cited References Count:21.

[61] B. H. Vanderschoot and P. Bergveld, "The pH-static enzyme sensor - an ISFET-based enzyme sensor, insensitive to the buffer capacity of the sample," *Analytica Chimica Acta*, vol. 199, pp. 157–160, 1987, l5913 Times Cited:25 Cited References Count:6.

[62] C. S. Lee, S. K. Kim, and M. Kim, "Ion-sensitive field-effect transistor for biological sensing," *Sensors*, vol. 9, no. 9, pp. 7111–7131, 2009, 499IS Times Cited:0 Cited References Count:108.

[63] D. C. Li, P. H. Yang, and M. S. C. Lu, "CMOS open-gate ion-sensitive field-effect transistors for ultrasensitive dopamine detection," *Ieee Transactions on Electron Devices*, vol. 57, no. 10, pp. 2761–2767, 2010, 669KH Times Cited:0 Cited References Count:21.

[64] R. E. G. Vanhal, J. C. T. Eijkel, and P. Bergveld, "A novel description of ISFET sensitivity with the buffer capacity and double-layer capacitance as key parameters," *Sensors and Actuators B-Chemical*, vol. 24, no. 1-3, pp. 201–205, 1995, rm959 Times Cited:44 Cited References Count:10.

[65] D. S. Kim, Y. T. Jeong, H. J. Park, J. K. Shin, P. Choi, J. H. Lee, and G. Lim, "An FET-type charge sensor for highly sensitive detection of DNA sequence," *Biosensors & Bioelectronics*, vol. 20, no. 1, pp. 69–74, 2004, 855BJ Times Cited:93 Cited References Count:14.

[66] D. S. Kim, H. J. Park, H. M. Jung, J. K. Shin, P. Choi, J. H. Lee, and G. Lim, "Field effect transistor-based bimolecular sensor employing a Pt reference electrode for the detection of deoxyribonucleic acid sequence," *Japanese Journal of Applied Physics Part 1-Regular Papers Short Notes & Review Papers*, vol. 43, no. 6B, pp. 3855–3859, 2004, 837FX Times Cited:26 Cited References Count:14.

[67] H. Ecken, S. Ingebrandt, M. Krause, D. Richter, M. Hara, and A. Offenhausser, "64-channel extended gate electrode arrays for extracellular

signal recording," *Electrochimica Acta*, vol. 48, no. 20-22, pp. 3355–3362, 2003, 718AR Times Cited:14 Cited References Count:20.

[68] T. Goda and Y. Miyahara, "Detection of microenvironmental changes induced by protein adsorption onto self-assembled monolayers using an extended gate-field effect transistor," *Analytical Chemistry*, vol. 82, no. 5, pp. 1803–1810, 2010, 559QN Times Cited:0 Cited References Count:31.

[69] E. M. Guerra, G. R. Silva, and M. Mulato, "Extended gate field effect transistor using V2O5 xerogel sensing membrane by sol-gel method," *Solid State Sciences*, vol. 11, no. 2, pp. 456–460, 2009, 416FN Times Cited:5 Cited References Count:28.

[70] H. Y. Hsu, C. Y. Wu, H. C. Lee, J. L. Lin, Y. L. Chin, and T. P. Sun, "Sodium and potassium sensors based on separated extended gate field effect transistor," *Biomedical Engineering-Applications Basis Communications*, vol. 21, no. 6, pp. 441–444, 2009, 534SV Times Cited:0 Cited References Count:9.

[71] Y. Ishige, M. Shimoda, and M. Kamahori, "Extended-gate FET-based enzyme sensor with ferrocenyl-alkanethiol modified gold sensing electrode," *Biosensors & Bioelectronics*, vol. 24, no. 5, pp. 1096–1102, 2009, sp. Iss. SI 405CL Times Cited:3 Cited References Count:20.

[72] W. H. Baumann, M. Lehmann, A. Schwinde, R. Ehret, M. Brischwein, and B. Wolf, "Microelectronic sensor system for microphysiological application on living cells," *Sensors and Actuators B-Chemical*, vol. 55, no. 1, pp. 77–89, 1999, 202YK Times Cited:56 Cited References Count:31.

[73] D. S. Kim, J. E. Park, J. K. Shin, P. K. Kim, G. Lim, and S. Shoji, "An extended gate FET-based biosensor integrated with a Si microfluidic channel for detection of protein complexes," *Sensors and Actuators B-Chemical*, vol. 117, no. 2, pp. 488–494, 2006, sp. Iss. SI 075IA Times Cited:10 Cited References Count:20.

[74] Y. Cui, Q. Q. Wei, H. K. Park, and C. M. Lieber, "Nanowire nanosensors for highly sensitive and selective detection of biological and chemical species," *Science*, vol. 293, no. 5533, pp. 1289–1292, 2001, 463TD Times Cited:1866 Cited References Count:22.

[75] F. Patolsky, G. F. Zheng, O. Hayden, M. Lakadamyali, X. W. Zhuang, and C. M. Lieber, "Electrical detection of single viruses," *Proceedings of the National Academy of Sciences of the United States of America*, vol. 101, no. 39, pp. 14 017–14 022, 2004, 858SG Times Cited:277 Cited References Count:23.

[76] Z. Li, Y. Chen, X. Li, T. I. Kamins, K. Nauka, and R. S. Williams, "Sequence-specific label-free DNA sensors based on silicon nanowires," *Nano Letters*, vol. 4, no. 2, pp. 245–247, 2004, 774EA Times Cited:198 Cited References Count:14.

[77] G. F. Zheng, F. Patolsky, Y. Cui, W. U. Wang, and C. M. Lieber, "Multiplexed electrical detection of cancer markers with nanowire sensor arrays," *Nature Biotechnology*, vol. 23, no. 10, pp. 1294–1301, 2005, 972QZ Times Cited:455 Cited References Count:49.

[78] G. F. Zheng, W. Lu, and C. M. Lieber, "Ultrahigh sensitive protein detection by frequency analysis using nanowire field effect sensors," *Abstracts of Papers of the American Chemical Society*, vol. 231, pp. –, 2006, 050YE 502-PHYS Times Cited:0 Cited References Count:0.

[79] E. Stern, J. F. Klemic, D. A. Routenberg, P. N. Wyrembak, D. B. Turner-Evans, A. D. Hamilton, D. A. LaVan, T. M. Fahmy, and M. A. Reed, "Label-free immunodetection with CMOS-compatible semiconducting nanowires," *Nature*, vol. 445, no. 7127, pp. 519–522, 2007, 131KI Times Cited:163 Cited References Count:30.

[80] E. Stern, A. Vacic, N. K. Rajan, J. M. Criscione, J. Park, B. R. Ilic, D. J. Mooney, M. A. Reed, and T. M. Fahmy, "Label-free biomarker detection from whole blood," *Nature Nanotechnology*, vol. 5, no. 2, pp. 138–142, 2010, 562NL Times Cited:1 Cited References Count:30.

[81] W. C. Chen, H. C. Lin, Y. C. Chang, C. D. Lin, and T. Y. Huang, "In situ doped source/drain for performance enhancement of double-gated poly-Si nanowire transistors," *Ieee Transactions on Electron Devices*, vol. 57, no. 7, pp. 1608–1615, 2010, 613QX Times Cited:0 Cited References Count:23.

[82] Z. Q. Gao, A. Agarwal, A. D. Trigg, N. Singh, C. Fang, C. H. Tung, Y. Fan, K. D. Buddharaju, and J. M. Kong, "Silicon nanowire arrays for label-free detection of DNA," *Analytical Chemistry*, vol. 79, no. 9, pp. 3291–3297, 2007, 161PG Times Cited:102 Cited References Count:32.

[83] A. Cattani-Scholz, D. Pedone, M. Dubey, S. Neppl, B. Nickel, P. Feulner, J. Schwartz, G. Abstreiter, and M. Tornow, "Organophosphonate-based PNA-functionalization of silicon nanowires for label-free DNA detection," *Acs Nano*, vol. 2, no. 8, pp. 1653–1660, 2008, 342HK Times Cited:31 Cited References Count:34.

[84] M. G. Nikolaides, S. Rauschenbach, and A. R. Bausch, "Characterization of a silicon-on-insulator based thin film resistor in electrolyte solutions for sensor applications," *Journal of Applied Physics*, vol. 95,

no. 7, pp. 3811–3815, 2004, 805BV Times Cited:33 Cited References Count:20.

[85] S. Q. Lud, M. G. Nikolaides, I. Haase, M. Fischer, and A. R. Bausch, "Field effect of screened charges: Electrical detection of peptides and proteins by a thin-film resistor," *Chemphyschem*, vol. 7, no. 2, pp. 379–384, 2006, 013IZ Times Cited:27 Cited References Count:28.

[86] J. M. Yang, L. de la Garza, T. J. Thornton, M. Kozicki, and D. Gust, "Controlling the threshold voltage of a metal-oxide-semiconductor field effect transistor by molecular protonation of the Si : SiO2 interface," *Journal of Vacuum Science & Technology B*, vol. 20, no. 4, pp. 1706–1709, 2002, 585ED Times Cited:12 Cited References Count:8.

[87] P. A. Neff, A. Naji, C. Ecker, B. Nickel, R. Von Klitzing, and A. R. Bausch, "Electrical detection of self-assembled polyelectrolyte multilayers by a thin film resistor," *Macromolecules*, vol. 39, no. 2, pp. 463–466, 2006, 007XN Times Cited:32 Cited References Count:27.

[88] S. Sharma, K. Buchholz, S. M. Luber, U. Rant, M. Tornow, and G. Abstreiter, "Silicon-on-insulator microfluidic device with monolithic sensor integration for microTAS applications," *Journal of Microelectromechanical Systems*, vol. 15, no. 2, pp. 308–313, 2006, 032JH Times Cited:9 Cited References Count:20.

[89] N. Elfstrom, A. E. Karlstrom, and J. Linnrost, "Silicon nanoribbons for electrical detection of biomolecules," *Nano Letters*, vol. 8, no. 3, pp. 945–949, 2008, 273QS Times Cited:14 Cited References Count:28.

[90] Y. Fang, F. Patolsky, and C. M. Lieber, "Electrical detection of single DNA molecules with silicon nanowire devices," *Biophysical Journal*, p. 551a, 2007, suppl. S 132WA Times Cited:1 Cited References Count:0.

[91] Y. L. Bunimovich, Y. S. Shin, W. S. Yeo, M. Amori, G. Kwong, and J. R. Heath, "Quantitative real-time measurements of DNA hybridization with alkylated nonoxidized silicon nanowires in electrolyte solution," *Journal of the American Chemical Society*, vol. 128, no. 50, pp. 16 323–16 331, 2006, 116TP Times Cited:83 Cited References Count:57.

[92] G. J. Zhang, G. Zhang, J. H. Chua, R. E. Chee, E. H. Wong, A. Agarwal, K. D. Buddharaju, N. Singh, Z. Q. Gao, and N. Balasubramanian, "DNA sensing by silicon nanowire: Charge layer distance dependence," *Nano Letters*, vol. 8, no. 4, pp. 1066–1070, 2008, 287IQ Times Cited:24 Cited References Count:23.

[93] G. J. Zhang, J. H. Chua, R. E. Chee, A. Agarwal, and S. M. Wong, "Label-free direct detection of miRNAs with silicon nanowire biosensors," *Biosensors & Bioelectronics*, vol. 24, no. 8, pp. 2504–2508, 2009, 442AC Times Cited:1 Cited References Count:28.

[94] G. J. Zhang, J. H. Chua, R. E. Chee, A. Agarwal, S. M. Wong, K. D. Buddharaju, and N. Balasubramanian, "Highly sensitive measurements of PNA-DNA hybridization using oxide-etched silicon nanowire biosensors," *Biosensors & Bioelectronics*, vol. 23, no. 11, pp. 1701–1707, 2008, 309WV Times Cited:11 Cited References Count:20.

[95] F. Patolsky, G. F. Zheng, and C. M. Lieber, "Fabrication of silicon nanowire devices for ultrasensitive, label-free, real-time detection of biological and chemical species," *Nature Protocols*, vol. 1, no. 4, pp. 1711–1724, 2006, 234IU Times Cited:76 Cited References Count:33.

[96] J. H. Chua, R. E. Chee, A. Agarwal, S. M. Wong, and G. J. Zhang, "Label-free electrical detection of cardiac biomarker with complementary metal-oxide semiconductor-compatible silicon nanowire sensor arrays," *Analytical Chemistry*, vol. 81, no. 15, pp. 6266–6271, 2009, 476PV Times Cited:2 Cited References Count:29.

[97] E. Stern, A. Vacic, C. Li, F. N. Ishikawa, C. W. Zhou, M. A. Reed, and T. M. Fahmy, "A nanoelectronic enzyme-linked immunosorbent assay for detection of proteins in physiological solutions," *Small*, vol. 6, no. 2, pp. 232–238, 2010, 553JX Times Cited:0 Cited References Count:53.

[98] F. Patolsky, B. P. Timko, G. H. Yu, Y. Fang, A. B. Greytak, G. F. Zheng, and C. M. Lieber, "Detection, stimulation, and inhibition of neuronal signals with high-density nanowire transistor arrays," *Science*, vol. 313, no. 5790, pp. 1100–1104, 2006, 076ZT Times Cited:157 Cited References Count:38.

[99] T. Cohen-Karni, B. P. Timko, L. E. Weiss, and C. M. Lieber, "Flexible electrical recording from cells using nanowire transistor arrays," *Proceedings of the National Academy of Sciences of the United States of America*, vol. 106, no. 18, pp. 7309–7313, 2009, 441QI Times Cited:5 Cited References Count:33.

[100] E. Stern, E. R. Steenblock, M. A. Reed, and T. M. Fahmy, "Label-free electronic detection of the antigen-specific t-cell immune response," *Nano Letters*, vol. 8, no. 10, pp. 3310–3314, 2008, 358HD Times Cited:4 Cited References Count:29.

[101] S. Y. Chen, J. G. Bomer, W. G. van der Wiel, E. T. Carlen, and A. van den Berg, "Top-down fabrication of sub-30 nm monocrystalline silicon nanowires using conventional microfabrication," *Acs*

Nano, vol. 3, no. 11, pp. 3485–3492, 2009, 521UY Times Cited:0 Cited References Count:37.

[102] H. D. Tong, S. Chen, W. G. van der Wiel, E. T. Carlen, and A. van den Berg, "Novel top-down wafer-scale fabrication of single crystal silicon nanowires," *Nano Letters*, vol. 9, no. 3, pp. 1015–1022, 2009, 418IO Times Cited:2 Cited References Count:61.

[103] R. Juhasz, N. Elfstrom, and J. Linnros, "Controlled fabrication of silicon nanowires by electron beam lithography and electrochemical size reduction," *Nano Letters*, vol. 5, no. 2, pp. 275–280, 2005, 898UA Times Cited:21 Cited References Count:16.

[104] N. Elfstrom, R. Juhasz, I. Sychugov, T. Engfeldt, A. E. Karlstrom, and J. Linnros, "Surface charge sensitivity of silicon nanowires: Size dependence," *Nano Letters*, vol. 7, no. 9, pp. 2608–2612, 2007, 211CM Times Cited:19 Cited References Count:16.

[105] O. H. Elibol, B. Reddy, and R. Bashir, "Nanoscale thickness double-gated field effect silicon sensors for sensitive pH detection in fluid," *Applied Physics Letters*, vol. 92, no. 19, pp. –, 2008, 310XN Times Cited:5 Cited References Count:16.

[106] X. P. A. Gao, G. F. Zheng, and C. M. Lieber, "Subthreshold regime has the optimal sensitivity for nanowire FET biosensors," *Nano Letters*, vol. 10, no. 2, pp. 547–552, 2010, 553BE Times Cited:0 Cited References Count:29.

[107] E. Stern, R. Wagner, F. J. Sigworth, R. Breaker, T. M. Fahmy, and M. A. Reed, "Importance of the debye screening length on nanowire field effect transistor sensors," *Nano Letters*, vol. 7, no. 11, pp. 3405–3409, 2007, 232ZI Times Cited:30 Cited References Count:24.

[108] N. Elfstrom and J. Linnros, "Biomolecule detection using a silicon nanoribbon: accumulation mode versus inversion mode," *Nanotechnology*, vol. 19, no. 23, pp. –, 2008, 298BZ Times Cited:1 Cited References Count:19.

[109] P. R. Nair and M. A. Alam, "Dimensionally frustrated diffusion towards fractal adsorbers," *Physical Review Letters*, vol. 99, no. 25, pp. –, 2007, 244TB Times Cited:4 Cited References Count:15.

[110] P. R. Nair and M. A. Alam, "Performance limits of nanobiosensors," *Applied Physics Letters*, vol. 88, no. 23, pp. –, 2006, 061ZV Times Cited:34 Cited References Count:11.

[111] P. R. Nair and M. A. Alam, "Screening-limited response of nanobiosensors," *Nano Letters*, vol. 8, no. 5, pp. 1281–1285, 2008, 301OV Times Cited:21 Cited References Count:19.

[112] P. A. Neff, B. K. Wunderlich, S. Q. Lud, and A. R. Bausch, "Silicon-on-insulator based thin film resistors for quantitative biosensing applications," *Physica Status Solidi a-Applications and Materials Science*, vol. 203, no. 14, pp. 3417–3423, 2006, 112OP Times Cited:5 Cited References Count:19.

[113] A. Poghossian, A. Cherstvy, S. Ingebrandt, A. Offenhausser, and M. J. Schoning, "Possibilities and limitations of label-free detection of DNA hybridization with field-effect-based devices," *Sensors and Actuators B-Chemical*, vol. 111, pp. 470–480, 2005, sp. Iss. SI 977RM Times Cited:104 Cited References Count:32.

[114] M. J. S. Poghossian and Arshak, *Electrochemical Sensors, Biosensors and Their Biomedical Applications*. Elsevier Inc., 2008.

[115] T. M. Squires, R. J. Messinger, and S. R. Manalis, "Making it stick: convection, reaction and diffusion in surface-based biosensors," *Nature Biotechnology*, vol. 26, no. 4, pp. 417–426, 2008, 285NC Times Cited:32 Cited References Count:45.

[116] D. Misra and E. L. Heasell, "Electrical damage to silicon devices due to reactive ion etching," *Semiconductor Science and Technology*, vol. 5, no. 3, pp. 229–236, 1990, cu112 Times Cited:10 Cited References Count:0.

[117] N. K. Rajan, D. A. Routenberg, and M. A. Reed, "Optimal signal-to-noise ratio for silicon nanowire biochemical sensors," *Applied Physics Letters*, vol. 98, no. 26, 2011, 786VJ Times Cited:0 Cited References Count:19.

[118] J. P. Gambino and E. G. Colgan, "Silicides and ohmic contacts," *Materials Chemistry and Physics*, vol. 52, no. 2, pp. 99–146, 1998, yw558 Times Cited:204 Cited References Count:422.

[119] G. M. Credo, X. Su, K. Wu, O. H. Elibol, D. J. Liu, B. Reddy, T. W. Tsai, B. R. Dorvel, J. S. Daniels, R. Bashir, and M. Varma, "Label-free electrical detection of pyrophosphate generated from DNA polymerase reactions on field-effect devices," *Analyst*, vol. 137, no. 6, pp. 1351–1362, 2012, 895QI Times Cited:0 Cited References Count:40.

[120] J. Heinonen, *Biological role of inorganic pyrophosphate*. London, U.K.: Kluwer Academic Publishers, 2001.

[121] S. K. Kim, D. H. Lee, J. I. Hong, and J. Yoon, "Chemosensors for pyrophosphate," *Accounts of Chemical Research*, vol. 42, no. 1, pp. 23–31, 2009, 396UM Times Cited:131 Cited References Count:37.

[122] M. Ronaghi, M. Uhlen, and P. Nyren, "A sequencing method based on real-time pyrophosphate," *Science*, vol. 281, no. 5375, pp. 363–+, 1998, 102HR Times Cited:641 Cited References Count:19.

[123] D. J. Liu, G. M. Credo, X. Su, K. Wu, H. C. Lim, O. H. Elibol, R. Bashir, and M. Varma, "Surface immobilizable chelator for label-free electrical detection of pyrophosphate," *Chemical Communications*, vol. 47, no. 29, pp. 8310–8312, 2011, 795NM Times Cited:1 Cited References Count:15.

[124] I. Luzinov, D. Julthongpiput, A. Liebmann-Vinson, T. Cregger, M. D. Foster, and V. V. Tsukruk, "Epoxy-terminated self-assembled monolayers: Molecular glues for polymer layers," *Langmuir*, vol. 16, no. 2, pp. 504–516, 2000, 276RA Times Cited:124 Cited References Count:57.

[125] I. Heller, A. M. Janssens, J. Mannik, E. D. Minot, S. G. Lemay, and C. Dekker, "Identifying the mechanism of biosensing with carbon nanotube transistors," *Nano Letters*, vol. 8, no. 2, pp. 591–595, 2008, 262RR Times Cited:123 Cited References Count:32.

[126] B. Dorvel, B. Reddy, I. Block, P. Mathias, S. E. Clare, B. Cunningham, D. E. Bergstrom, and R. Bashir, "Vapor-phase deposition of monofunctional alkoxysilanes for sub-nanometer-level biointerfacing on silicon oxide surfaces," *Advanced Functional Materials*, vol. 20, no. 1, pp. 87–95, 2010, 549JR Times Cited:0 Cited References Count:67.

[127] B. M. Venkatesan, B. Dorvel, S. Yemenicioglu, N. Watkins, I. Petrov, and R. Bashir, "Highly sensitive, mechanically stable nanopore sensors for DNA analysis," *Advanced Materials*, vol. 21, no. 27, pp. 2771–2776, 2009, 478SF Times Cited:2 Cited References Count:32.

[128] A. J. Bard and L. R. Faulkner, *Electrochemical Methods: Fundamentals and Applications*, 2nd ed. New Jersey: John Wiley & Sons, 2001.

[129] M. Dankerl, A. Reitinger, M. Stutzmann, and J. A. Garrido, "Resolving the controversy on the pH sensitivity of diamond surfaces," *Physica Status Solidi-Rapid Research Letters*, vol. 2, no. 1, pp. 31–33, 2008, 262BT Times Cited:9 Cited References Count:12.

[130] J. Robertson, "High dielectric constant oxides," *European Physical Journal-Applied Physics*, vol. 28, no. 3, pp. 265–291, 2004, 876NA Times Cited:164 Cited References Count:158.

[131] D. A. Muller, T. Sorsch, S. Moccio, F. H. Baumann, K. Evans-Lutterodt, and G. Timp, "The electronic structure at the atomic scale of ultrathin gate oxides," *Nature*, vol. 399, no. 6738, pp. 758–761, 1999, 210JP Times Cited:543 Cited References Count:20.

[132] O. Knopfmacher, A. Tarasov, W. Y. Fu, M. Wipf, B. Niesen, M. Calame, and C. Schonenberger, "Nernst limit in dual-gated si-nanowire FET sensors," *Nano Letters*, vol. 10, no. 6, pp. 2268–2274, 2010, 606TB Times Cited:0 Cited References Count:33.

[133] B. Iniguez, B. Gentinne, V. Dessard, and D. Flandre, "A physically-based c-infinity-continuous model for accumulation-mode SOI pMOSFET's," *Ieee Transactions on Electron Devices*, vol. 46, no. 12, pp. 2295–2303, 1999, 262GZ Times Cited:4 Cited References Count:15.

[134] S. L. Jang and S. S. Liu, "A novel approach for modeling accumulation-mode SOI MOSFETs," *Solid-State Electronics*, vol. 43, no. 1, pp. 87–96, 1999, 147NP Times Cited:2 Cited References Count:16.

[135] H. O. Joachim, Y. Yamaguchi, Y. Inoue, T. Nishimura, and N. Tsubouchi, "Analytical modeling of short-channel behavior of accumulation-mode transistors on silicon-on-insulator substrate," *Japanese Journal of Applied Physics*, vol. 33, no. 1B, pp. 558–562, 1994, mv678 Times Cited:3 Cited References Count:7.

[136] M. A. Harvey, "Point-of-care laboratory testing in critical care," *American Journal of Critical Care*, vol. 8, no. 2, pp. 72–83, 1999.

[137] M. L. Kilgore, S. J. Steindel, and J. A. Smith, "Evaluating stat testing options in an academic health center: Therapeutic turnaround time and staff satisfaction," *Clinical Chemistry*, vol. 44, no. 8 I, pp. 1597–1603, 1998.

[138] J. D. Douketis, "Patient self-monitoring of oral anticoagulant therapy: potential benefits and implications for clinical practice," *American journal of cardiovascular drugs : drugs, devices, and other interventions*, vol. 1, no. 4, pp. 245–251, 2001.

[139] J. Kimura and T. Kuriyama, "FET biosensors," *Journal of Biotechnology*, vol. 15, no. 3, pp. 239–254, 1990, dv624 Times Cited:14 Cited References Count:27.

[140] J. R. Sandifer and J. J. Voycheck, "A review of biosensor and industrial applications of pH-ISFETs and an evaluation of Honeywell's duraFET," *Mikrochimica Acta*, vol. 131, no. 1-2, pp. 91–98, 1999.

[141] M. J. Schning and A. Poghossian, "Bio FEDs (field-effect devices): State-of-the-art and new directions," *Electroanalysis*, vol. 18, no. 19-20, pp. 1893–1900, 2006.

[142] M. Yuqing, G. Jianguo, and C. Jianrong, "Ion sensitive field effect transducer-based biosensors," *Biotechnology Advances*, vol. 21, no. 6, pp. 527–534, 2003.

[143] A. Gao, N. Lu, P. Dai, T. Li, H. Pei, X. Gao, Y. Gong, Y. Wang, and C. Fan, "Silicon-nanowire-based CMOS-compatible field-effect transistor nanosensors for ultrasensitive electrical detection of nucleic acids," *Nano Letters*, vol. 11, no. 9, pp. 3974–3978, 2011.

[144] L. Luo, J. Jie, W. Zhang, Z. He, J. Wang, G. Yuan, L. C. M. Wu, and S. T. Lee, "Silicon nanowire sensors for Hg2+ and Cd2+ ions," *Applied Physics Letters*, vol. 94, no. 19, 2009.

[145] W. U. Wang, C. Chen, K. H. Lin, Y. Fang, and C. M. Lieber, "Label-free detection of small-molecule-protein interactions by using nanowire nanosensors," *Proceedings of the National Academy of Sciences of the United States of America*, vol. 102, no. 9, pp. 3208–3212, 2005, 903KC Times Cited:142 Cited References Count:30.

[146] S. Choi, I. Park, Z. Hao, H. Y. N. Holman, and A. P. Pisano, "Quantitative studies of long-term stable, top-down fabricated silicon nanowire pH sensors," *Applied Physics A: Materials Science and Processing*, pp. 1–8, 2012.

[147] O. H. Elibol, D. Morisette, D. Akin, J. P. Denton, and R. Bashir, "Integrated nanoscale silicon sensors using top-down fabrication," *Applied Physics Letters*, vol. 83, no. 22, pp. 4613–4615, 2003, 747CF Times Cited:41 Cited References Count:6.

[148] P. Ginet, S. Akiyama, N. Takama, H. Fujita, and B. Kim, "CMOS-compatible fabrication of top-gated field-effect transistor silicon nanowire-based biosensors," *Journal of Micromechanics and Microengineering*, vol. 21, no. 6, 2011.

[149] A. Kim, C. S. Ah, H. Y. Yu, J. H. Yang, I. B. Baek, C. G. Ahn, C. W. Park, M. S. Jun, and S. Lee, "Ultrasensitive, label-free, and real-time immunodetection using silicon field-effect transistors," *Applied Physics Letters*, vol. 91, no. 10, 2007.

[150] S. Chen, L. Nyholm, N. Jokilaakso, A. E. Karlstrm, J. Linnros, U. Smith, and S. L. Zhang, "Current instability for silicon nanowire field-effect sensors operating in electrolyte with platinum gate electrodes," *Electrochemical and Solid-State Letters*, vol. 14, no. 7, pp. J34–J37, 2011.

[151] S. Kim, K. Kim, T. Rim, C. Park, D. Cho, C. K. Baek, Y. H. Jeong, M. Meyyappan, and J. S. Lee, "pH sensing and noise characteristics of Si nanowire ion-sensitive field effect transistors," pp. 1233–1236.

[152] L. Bousse and P. Bergveld, "The role of buried OH sites in the response mechanism of inorganic-gate pH-sensitive ISFETs," *Sensors and Actuators*, vol. 6, no. 1, pp. 65–78, 1984.

[153] J. N. Zemel, "Microfabricated nonoptical chemical sensors," *Review of Scientific Instruments*, vol. 61, no. 6, pp. 1579–1606, 1990.

[154] C. S. Lai, C. M. Yang, and T. F. Lu, "PH sensitivity improvement on 8 nm thick hafnium oxide by post deposition annealing," *Electrochemical and Solid-State Letters*, vol. 9, no. 3, pp. G90–G92, 2006.

[155] P. D. Van Der Wal, D. Briand, G. Mondin, S. Jenny, S. Jeanneret, C. Millon, H. Roussel, C. Dubourdieu, and N. F. De Rooij, "High-k dielectrics for use as ISFET gate oxides," *Proceedings of American Chemical Society*, vol. 2, pp. 677–680.

[156] K. A. Cissell, Y. Rahimi, S. Shrestha, E. A. Hunt, and S. K. Deo, "Bioluminescence-based detection of microRNA, mir21 in breast cancer cells," *Analytical Chemistry*, vol. 80, no. 7, pp. 2319–2325, 2008.

[157] G. Gabriely, N. M. Teplyuk, and A. M. Krichevsky, "Context effect: microRNA-10b in cancer cell proliferation, spread and death," *Autophagy*, vol. 7, no. 11, pp. 1384–1386, 2011.

[158] A. G. Iyevleva, E. S. Kuligina, N. V. Mitiushkina, A. V. Togo, Y. Miki, and E. N. Imyanitov, "High level of mir-21, mir-10b, and mir-31 expression in bilateral vs. unilateral breast carcinomas," *Breast Cancer Research and Treatment*, vol. 131, no. 3, pp. 1049–1059, 2012.

[159] L. Ma, F. Reinhardt, E. Pan, J. Soutschek, B. Bhat, E. G. Marcusson, J. Teruya-Feldstein, G. W. Bell, and R. A. Weinberg, "Therapeutic silencing of mir-10b inhibits metastasis in a mouse mammary tumor model," *Nature Biotechnology*, vol. 28, no. 4, pp. 341–347, 2010.

[160] L. Ma, J. Teruya-Feldstein, and R. A. Weinberg, "Tumour invasion and metastasis initiated by microRNA-10b in breast cancer," *Nature*, vol. 449, no. 7163, pp. 682–688, 2007.

[161] Y. Liang, D. Ridzon, L. Wong, and C. Chen, "Characterization of microRNA expression profiles in normal human tissues," *BMC Genomics*, vol. 8, pp. 1324–1327, 2007.

[162] A. Lambacher and P. Fromherz, "Fluorescence interference-contrast microscopy on oxidized silicon using a monomolecular dye layer," *Applied Physics a-Materials Science & Processing*, vol. 63, no. 3, pp. 207–216, 1996, vg157 Times Cited:124 Cited References Count:27.

[163] D. M. Hausmann, E. Kim, J. Becker, and R. G. Gordon, "Atomic layer deposition of hafnium and zirconium oxides using metal amide precursors," *Chemistry of Materials*, vol. 14, no. 10, pp. 4350–4358, 2002.

[164] K. Kukli, M. Ritala, T. Sajavaara, J. Keinonen, and M. Leskel, "Atomic layer deposition of hafnium dioxide films from hafnium tetrakis(ethylmethylamide) and water," *Chemical Vapor Deposition*, vol. 8, no. 5, pp. 199–204, 2002.

[165] F. Bohra, B. Jiang, and J. M. Zuo, "Textured crystallization of ultrathin hafnium oxide films on silicon substrate," *Applied Physics Letters*, vol. 90, no. 16, pp. 103–109, 2007.

[166] G. D. Wilk, R. M. Wallace, and J. M. Anthony, "Hafnium and zirconium silicates for advanced gate dielectrics," *Journal of Applied Physics*, vol. 87, no. 1, pp. 484–492, 2000.

[167] J. B. E.H Nicollian, *MOS Physics and Technology.* New York, NY: Wiley, 1982.

[168] A. Callegari, E. Cartier, M. Gribelyuk, H. F. Okorn-Schmidt, and T. Zabel, "Physical and electrical characterization of hafnium oxide and hafnium silicate sputtered films," *Journal of Applied Physics*, vol. 90, no. 12, pp. 6466–6475, 2001.

[169] L. Zhong, W. L. Daniel, Z. Zhang, S. A. Campbell, and W. L. Gladfelter, "Atomic layer deposition, characterization, and dielectric properties of HfO2/SiO2 nanolaminates and comparisons with their homogeneous mixtures," *Chemical Vapor Deposition*, vol. 12, no. 2-3, pp. 143–150, 2006.

[170] L. V. Goncharova, M. Dalponte, T. Feng, T. Gustafsson, E. Garfunkel, P. S. Lysaght, and G. Bersuker, "Diffusion and interface growth in hafnium oxide and silicate ultrathin films on Si(001)," *Physical Review B - Condensed Matter and Materials Physics*, vol. 83, no. 11, 2011.

[171] S. Rudenja, A. Minko, and D. A. Buchanan, "Low-temperature deposition of stoichiometric HfO2 on silicon: Analysis and quantification of the HfO2/Si interface from electrical and xps measurements," *Applied Surface Science*, vol. 257, no. 1, pp. 17–21, 2010.

[172] A. V. Saprigin, C. W. Thomas, C. S. Dulcey, C. H. Patterson Jr, and M. S. Spector, "Spectroscopic quantification of covalently immobilized oligonucleotides," *Surface and Interface Analysis*, vol. 37, no. 1, pp. 24–32, 2005.

[173] N. Crampton, W. A. Bonass, J. Kirkham, and N. H. Thomson, "Formation of aminosilane-functionalized mica for atomic force microscopy imaging of DNA," *Langmuir*, vol. 21, no. 17, pp. 7884–7891, 2005.

[174] B. A. Webb, M. Chimenti, M. Jacobson, and D. Barber, "Dysregulated pH: a perfect storm for cancer progression," *Nature Reviews Cancer*, vol. 11, pp. 671–677, 2011.

[175] F. A. Gallagher, M. I. Kettunen, S. E. Day, D. E. Hu, J. H. Ardenkjaer-Larsen, R. in't Zandt, P. R. Jensen, M. Karlsson, K. Golman, M. H. Lerche, and K. M. Brindle, "Magnetic resonance imaging of pH in vivo using hyperpolarized (13)c-labelled bicarbonate," *Nature*, vol. 453, no. 7197, pp. 940–U73, 2008, 311WV Times Cited:120 Cited References Count:30.

[176] R. J. Gillies, N. Raghunand, G. S. Karczmar, and Z. M. Bhujwalla, "MRI of the tumor microenvironment," *Journal of Magnetic Resonance Imaging*, vol. 16, no. 4, pp. 430–450, 2002, 601KV Times Cited:152 Cited References Count:221.

[177] N. Raghunand, M. I. Altbach, R. van Sluis, B. Baggett, C. W. Taylor, Z. M. Bhujwalla, and R. J. Gillies, "Plasmalemmal pH-gradients in drug-sensitive and drug-resistant MCF-7 human breast carcinoma xenografts measured by P-31 magnetic resonance spectroscopy," *Biochemical Pharmacology*, vol. 57, no. 3, pp. 309–312, 1999, 152CN Times Cited:46 Cited References Count:16.

[178] L. Stuwe, M. Muller, A. Fabian, J. Waning, S. Mally, J. Noel, A. Schwab, and C. Stock, "pH dependence of melanoma cell migration: protons extruded by NHE1 dominate protons of the bulk solution," *Journal of Physiology-London*, vol. 585, no. 2, pp. 351–360, 2007, 236UW Times Cited:27 Cited References Count:40.

[179] S. D. Webb, J. A. Sherratt, and R. G. Fish, "Mathematical modelling of tumour acidity: Regulation of intracellular pH," *Journal of Theoretical Biology*, vol. 196, no. 2, pp. 237–250, 1999, 159PR Times Cited:33 Cited References Count:43.

[180] M. F. McCarty and J. Whitaker, "Manipulating tumor acidification as a cancer treatment strategy," *Alternative Medicine Review*, vol. 15, no. 3, pp. 264–272, 2010, 665BF Times Cited:0 Cited References Count:101.

[181] N. Raghunand, X. He, R. van Sluis, B. Mahoney, B. Baggett, C. W. Taylor, G. Paine-Murrieta, D. Roe, Z. M. Bhujwalla, and R. J. Gillies, "Enhancement of chemotherapy by manipulation of tumour pH," *British Journal of Cancer*, vol. 80, no. 7, pp. 1005–1011, 1999, 197VK Times Cited:83 Cited References Count:26.

[182] J. R. Griffiths, "Are cancer-cells acidic," *British Journal of Cancer*, vol. 64, no. 3, pp. 425–427, 1991, gf223 Times Cited:248 Cited References Count:32.

[183] R. J. Gillies, Z. Liu, and Z. Bhujwalla, "P-31-MRS measurements of extracellular pH of tumors using 3-aminopropylphosphonate," *American Journal of Physiology*, vol. 267, no. 1, pp. C195–C203, 1994, part 1 Ny984 Times Cited:120 Cited References Count:30.

[184] A. S. E. Ojugo, P. M. J. McSheehy, D. J. O. McIntyre, C. McCoy, M. Stubbs, M. O. Leach, I. R. Judson, and J. R. Griffiths, "Measurement of the extracellular pH of solid tumours in mice by magnetic resonance spectroscopy: a comparison of exogenous F-19 and P-31 probes," *Nmr in Biomedicine*, vol. 12, no. 8, pp. 495–504, 1999, 282RM Times Cited:85 Cited References Count:34.

[185] M. Stubbs, R. L. Veech, and J. R. Griffiths, "Tumor metabolism - the lessons of magnetic-resonance spectroscopy," *Advances in Enzyme Regulation, Vol 35*, vol. 35, pp. 101–115, 1995, bd26c Times Cited:41 Cited References Count:52 Advances in Enzyme Regulation.

[186] R. V. Benjaminsen, H. H. Sun, J. R. Henriksen, N. M. Christensen, K. Almdal, and T. L. Andresen, "Evaluating nanoparticle sensor design for intracellular pH measurements," *Acs Nano*, vol. 5, no. 7, pp. 5864–5873, 2011, 796ES Times Cited:0 Cited References Count:51.

[187] S. M. Al-Hilli, R. T. Al-Mofarji, and M. Willander, "Zinc oxide nanorod for intracellular pH sensing," *Applied Physics Letters*, vol. 89, no. 17, 2006, 099IB Times Cited:17 Cited References Count:14.

[188] S. Y. Chen, J. G. Bomer, E. T. Carlen, and A. van den Berg, "Al(2)O(3)/Silicon nanoISFET with near ideal nernstian response," *Nano Letters*, vol. 11, no. 6, pp. 2334–2341, 2011, 773QJ Times Cited:1 Cited References Count:42.

[189] B. Reddy, B. R. Dorvel, J. Go, P. R. Nair, O. H. Elibol, G. M. Credo, J. S. Daniels, E. K. C. Chow, X. Su, M. Varma, M. A. Alam, and R. Bashir, "High-k dielectric Al(2)O(3) nanowire and nanoplate field effect sensors for improved pH sensing," *Biomedical Microdevices*, vol. 13, no. 2, pp. 335–344, 2011, 732EY Times Cited:0 Cited References Count:41.

[190] J. Go, P. Nair, J. B. Reddy, B. R. Dorvel, R. Bashir, and M. Alam, "Coupled heterogenous 'nanowire-nanoplate' planar transistor sensors for giant nernst response," *ACS Nano*, 2012, under Review.

[191] M. J. Deen, M. W. Shinwari, J. C. Ranuarez, and D. Landheer, "Noise considerations in field-effect biosensors," *Journal of Applied Physics*, vol. 100, no. 7, 2006, 094OE Times Cited:15 Cited References Count:12.

[192] O. H. Elibol, B. Reddy, P. R. Nair, B. Dorvel, F. Butler, Z. S. Ahsan, D. E. Bergstrom, M. A. Alam, and R. Bashir, "Localized heating on silicon field effect transistors: Device fabrication and temperature measurements in fluid," *Lab on a Chip*, vol. 9, no. 19, pp. 2789–2795, 2009, 494GM Times Cited:0 Cited References Count:34.

[193] T. Henighan, A. Chen, G. Vieira, A. J. Hauser, F. Y. Yang, J. J. Chalmers, and R. Sooryakumar, "Manipulation of magnetically labeled and unlabeled cells with mobile magnetic traps," *Biophysical Journal*, vol. 98, no. 3, pp. 412–417, 2010, 552SH Times Cited:6 Cited References Count:26.